Alma Mater Studiorum
Università degli Studi di Bologna

Dottorato di Ricerca in Fisica
XVIII Ciclo

Measurement of leading-proton production cross section in DIS with the ZEUS detector at HERA

Candidato:
Dott. Lorenzo Rinaldi

Tutore:
Prof. Maurizio Basile

Coordinatore:
Prof. Roberto Soldati

Settore scientifico-disciplinare
FIS/04
Fisica Nucleare e Subnucleare

Contents

Introduction **1**

1 Theoretical overview **3**
1.1 DIS kinematics 4
1.2 Measurement of kinematic variables at HERA 5
1.3 The structure functions and the quark-parton model 8
1.4 The evolution equations 11
1.5 Diffraction 12
1.6 Leading-baryon physics 14
1.6.1 The Regge phenomenology 15
1.6.2 The Fracture Functions 18
1.6.3 Proton remnant fragmentation in the Lund Model . . 18
1.7 The Leading Effect and the Effective Energy 19
1.7.1 The Effective Energy phenomenology 19

2 The experimental apparatus **29**
2.1 The HERA collider 29
2.2 The ZEUS detector 32
2.2.1 The Central Tracking Detector 36
2.2.2 The Uranium Calorimeter 37
2.2.3 The Luminosity Monitor 39
2.2.4 The Forward Neutron Calorimeter 40
2.2.5 The ZEUS Trigger and Data Acquisition System . . . 41

3 The Leading Proton Spectrometer **43**
3.1 Beam optics 43
3.2 Spectrometer layout and construction 45
3.2.1 Detectors and Front-end 46
3.2.2 LPS Trigger 48
3.2.3 Mechanical Construction 49
3.3 Detector operations and performance 50
3.4 Reconstruction and alignment of the detector 51
3.4.1 How the Proton Momentum can be Measured 51

3.4.2 Track Reconstruction 54
3.4.3 Alignment and Calibration 56

4 The event simulation 59
4.1 Monte Carlo generators 59
4.1.1 Simulation of the standard Deep Inelastic Scattering . 59
4.1.2 Rapidity gaps and Soft Colour Interaction 60
4.2 The detector simulation 61
4.2.1 MOLPS: the LPS standalone simulation 62
4.3 Summary of Monte Carlo samples used in the analysis 63

5 The event selection 67
5.1 The DIS selection 67
5.2 The LPS selection 71
5.3 The Monte Carlo reweighting 73
5.4 Comparisons data-MC 82
5.5 Migrations from photoproduction and low Q^2 processes . . . 85
5.6 Background from overlay events 85
5.7 Background from π^+ and K^+ 90
5.8 Trigger effects 90

6 Measurement of the leading-proton production cross section 93
6.1 Resolution and binning 93
6.2 Acceptance 96
6.3 Systematic uncertainties 97
6.4 Measurement of the cross section 101
6.5 Leading-proton production rate to the inclusive DIS 113

7 Preliminary results with LPS s123 121
7.1 New Geometry implementation 122
7.1.1 Data-MC comparisons 122
7.2 Cross section measurement with a reduced event sample . . . 123
7.3 Conclusions 130

Conclusions 131

Acknowledgements 133

A Tables 135

Bibliography 159

Introduction

This thesis presents the measurement of leading-proton production in *ep* Deep Inelastic Scattering reactions. The leading-protons carry a large fraction of the initial proton momentum and are detected at very small angles in the proton beam direction.

The analysis is carried out using the data collected by the ZEUS experiment at the HERA electron-proton collider, during the 1997 data taking period. The leading protons were detected with high precision using the Leading Proton Spectrometer (LPS) [1] of the ZEUS detector. The LPS consists of 36 silicon planes grouped in six stations (s1→s6) placed along the beam-line in the proton beam direction, between about 20 m and 90 m from the interaction point. The main part of the work described in this thesis is done using data collected by the LPS stations s4-s5-s6, that form a spectrometer almost completely independent by the one that includes the stations s1-s2-s3. Work in progress with this latter spectrometer will also be presented.

The leading-proton production has been studied in proton-proton collisions, both at the ISR [2, 3] and in fixed target experiments [4, 5] . More recently, the HERA collider experiments measured the production of leading-proton in *ep* collisions [6–8] . With this few exceptions, the experimental data are scarce. This lack of information is a problem for a deep understanding of strong interactions beyond the perturbative expansion of QCD. Indeed, in high-energy collisions, the QCD-hardness scale decreases from the central, large transverse momentum region, to the soft, non-perturbative hadronic scale of the target-fragmentation region. Therefore the detection of leading-protons in the final state of high energy collisions yields information on the non-perturbative side of strong interactions.

Another reason for the interest in leading-proton production comes from the fact that the ISR data revealed universality features of the hadronic final state produced in electro-weak and strong interactions if the hadronic system is analysed in terms of the effective energy available for hadronization [9, 10].

The leading-proton production mechanism is still not completely understood and a deep study of the leading-proton properties is an important test for those theories and models that predict its production, as well as for the simulation of the beam-proton remnant hadronic fragmentation after the

collision.

Nowadays, a deep knowledge of the leading-proton properties is fundamental for the next Physics at the Large Hadron Collider. Indeed a large fraction of background at LHC is expected to come from the "pile-up" events, that are soft proton-proton interactions overlapping to the hard process. In the pile-up events, the proton has a "leading" behaviour and the leading-proton studies will allow a better understanding and modeling of this background.

The goal of this analysis is to measure the leading-proton production in the semi-inclusive DIS reaction $ep \to ep'X$.

The single-differential cross sections as a function of the longitudinal fractional momentum x_L of the incoming proton taken by the leading-proton, $d\sigma_{ep\to ep'X}/dx_L$ and of the leading-proton transverse squared momentum p_T^2, $d\sigma_{ep\to ep'X}/dp_T^2$ are measured as well as the double-differential cross section $d^2\sigma_{ep\to ep'X}/dx_L dp_T^2$. The exponential dependence of the cross section in p_T^2 at fixed x_L is also studied in detail.

Another important study is the comparison of the leading-proton production to the inclusive DIS reaction $ep \to eX$ and the measurement of the leading-proton-tagged structure function $\bar{F}_2^{LP}$.

The first chapter is an overview of the physics of DIS at HERA and of the leading-baryon physics.

Chapter 2 contains a description of the experimental facilities: the HERA collider and the ZEUS detector, while the Leading Proton Spectrometer is described in more detail in Chapter 3.

Chapter 4 introduces and describes the Monte Carlo techniques used for the analysis. In Chapter 5 the event selection procedures and the background treatment are discussed.

In Chapter 6 are presented the results of the measurement of the leading-proton production together with a description of the details of the analysis.

Chapter 7 is dedicated to the description of the work in progress with the LPS stations s1-s2-s3, that have not been commissioned for a long time and, up to now, have never been used for physics analysis.

The thesis work has been carried out in association with the ZEUS-Bologna group of the Italian Institute of Nuclear Physics (INFN) and with the Deutshes Elektronen-Synchrotron laboratory (DESY) in Hamburg.

Chapter 1

Theoretical overview

An important role in collision physics has been played by Deep Inelastic Scattering (DIS) experiments, in which leptons collide on hadronic targets. The point-like nature of the lepton beam allows to investigate the internal structure of the hadrons and to understand the laws to which the smallest constituents of the matter obey.

A seminal DIS experiment was performed at the Stanford Linear Accelerator Center (SLAC) in 1967 [11] , with an electron beam of 17 GeV impinging on a nucleon target. It was observed that the structure function, that describes the internal structure of the hadron, depends only on an adimensional variable x, introduced by Bjorken [12]. This behavior, known as scaling, agrees with the expectation for electrons scattering off free point-like objects within the nucleon. Influenced by the SLAC measurement and motivated by the assumption of Gell-Mann [13] and Zweig [14] that hadrons can be described as combinations of more foundamental objects, the quarks, Feynman proposed the quark-parton model [15]. In this model the hadrons are built by elementary point-like electrically charged objects (partons). By varying the resolution with which the hadron is inspected in a DIS experiment, beyond a certain limit, one always observes the same point-like sub-structure, a phenomenon that explains the scaling.

Further fixed-target DIS experiments in the 70's and 80's were carried out at CERN, FNAL and SLAC, increasing the lepton beam energy up to 300 GeV. In these experiments a breaking of scale invariance was observed. This experimental evidence confirmed the predictions of the parton density evolution equations as obtained by the Quantum Chromodynamics (QCD), the gauge theory of strong interaction.

With the advent of the *ep* collider HERA, at the DESY laboratory in Hamburg, the kinematic range of the DIS regime has been widely extended, allowing to achieve a much deeper knowledge of the structure of the matter.

1.1 DIS kinematics

At fixed energy of the incoming lepton and proton, the kinematics of the inclusive DIS reaction is completely described by a set of two independent variables. The general formulation of a ep deep inelastic scattering can be written in the form:

$$e(k) + P(p) \rightarrow \ell(k') + X(p') \tag{1.1}$$

were e is the incoming electron with its momentum $k = (E_e, \vec{k})$, P is the incoming proton with momentum $p = (E_p, \vec{p})$. The final state lepton ℓ, with momentum $k' = (E_\ell, \vec{k'})$ can be an electron or a neutrino. In the first case the event is a neutral current (NC) process in which a photon or a Z^0 boson is exchanged (fig. 1.1-left), while in the second case it is a charged current (CC) process, in which a W boson is exchanged, (fig. 1.1-right). In equation 1.1 X represents the hadronic final state. In the following only the NC process will be considered.

From the momenta of the incoming and outgoing particles it is possible to build the following quantities:

- the square of the energy available in the ep center of mass system:

$$s = (k + p)^2 = m_p^2 + 2k \cdot p \simeq 4E_e E_p, \tag{1.2}$$

  where m_p is the proton mass and the electron mass has been neglected;

- the square of the four-momentum transfer at the electron vertex:

$$Q^2 = -q^2 = -(k - k')^2, \tag{1.3}$$

- the energy of the photon in the proton rest frame:

$$\nu = \frac{q \cdot p}{m_p}, \tag{1.4}$$

- the fraction of the proton carried out by the struck quark (Bjorken variable):

$$x = \frac{Q^2}{2q \cdot p} = \frac{Q^2}{2m_p \nu}, \tag{1.5}$$

- the fraction of the energy lost by the electron in the proton rest system (inelasticity):

$$y = \frac{p \cdot q}{p \cdot k} = \frac{Q^2}{sx}, \tag{1.6}$$

- the square of the hadronic final state invariant mass in the γp system:

$$W^2 = (p + q)^2 \simeq sy(1 - x). \tag{1.7}$$

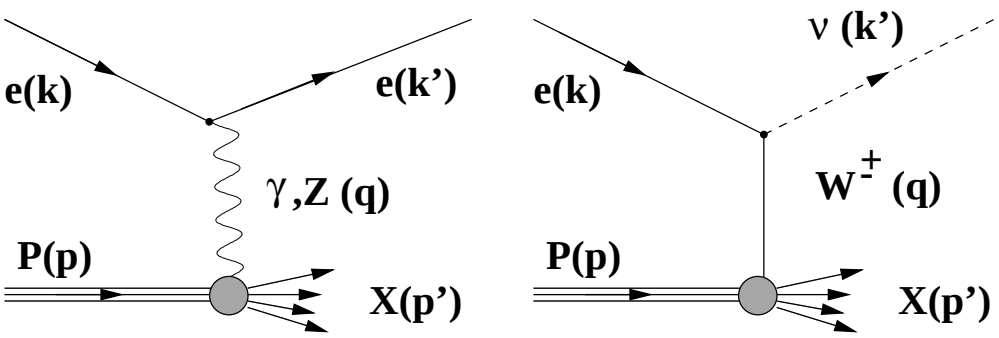

Figure 1.1: *Feynman graphs for Neutral Current (left) and Charge Current (right) scattering in ep interactions.*

The kinematic regime accessible at HERA is shown in figure 1.2, where a comparison with other DIS experiments is shown.

The momentum transfer, $q = \sqrt{-Q^2}$, is related to the wavelength λ of the virtual boson through the Heisenberg's uncertainty principle:

$$\lambda = \frac{1}{|\vec{q}|} \approx \frac{2m_p x}{Q^2}. \tag{1.8}$$

In order to resolve objects of size Δ, the wavelength λ has to be smaller than Δ. Indeed at low Q^2 the resolution is small and no proton substructure can be observed. At higher Q^2 the resolution increases and the inner structure of the proton can be probed.

1.2 Measurement of kinematic variables at HERA

The kinematic variables are reconstructed from the quantities measured in the detector. There are four variables directly measurable in the detector: the energy and the polar angle of the scattered electron and of the current jet (generated by the struck quark). Several methods are used at HERA, depending on the detector and on the kinematic range of the measurement.

The electron method. It uses the polar angle ($\theta_{e'}$) and the energy ($E_{e'}$) of the scattered electron. From the previous definitions the electron method yields:

$$y = 1 - \frac{E_{e'}}{2E_e} \cdot (1 - \cos\theta_{e'}),$$

$$Q^2 = 2E_e E_{e'} \cdot (1 + \cos\theta_{e'}),$$

$$x = \frac{E_{e'}}{2yE_p} \cdot (1 + \cos\theta_{e'}).$$

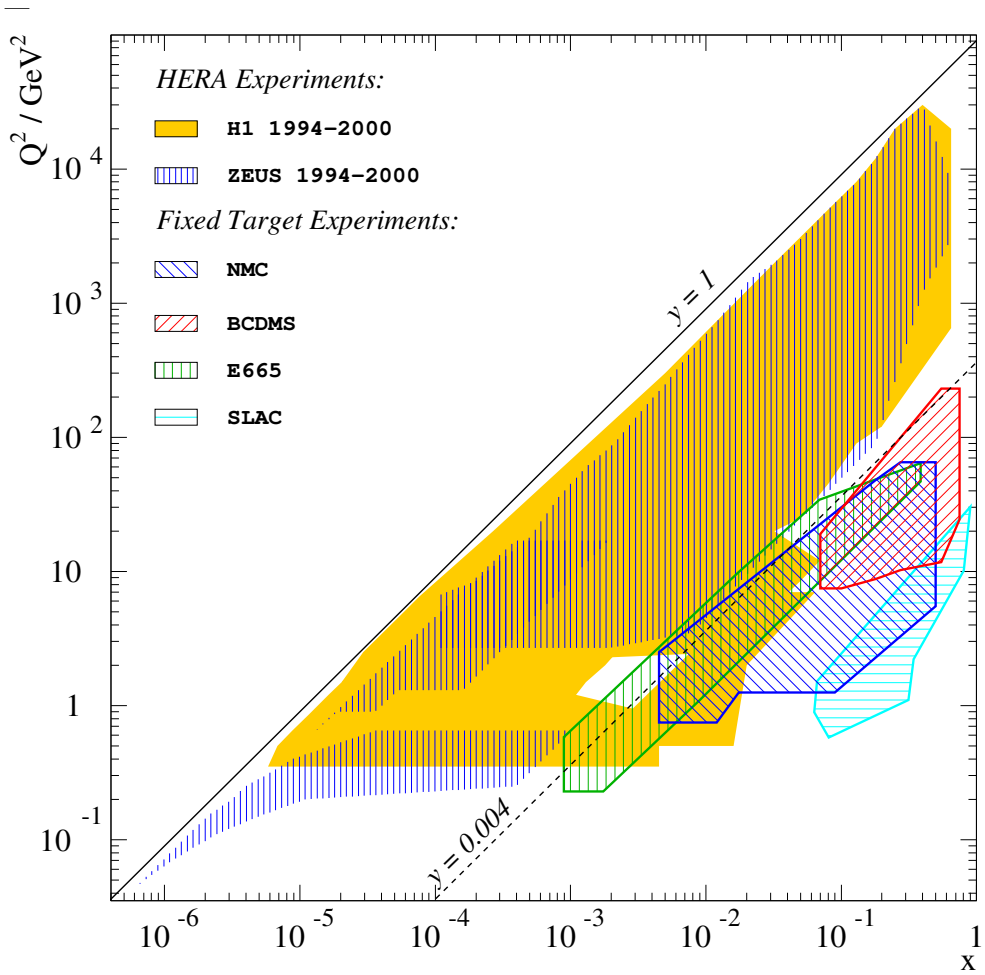

Figure 1.2: *Kinematic coverage in the $x - Q^2$ plane for various fixed-target experiments and the HERA collider experiment H1 and ZEUS.*

This method is very sensitive to the initial state radiation, in which a photon is emitted by the incident electron along the beam direction; this photon escapes detection and shifts the overall energy of the event.

The hadronic method. From the hadron system X_h (excluding the proton remnant) one finds:

$$y = \frac{E_h}{2E_e} \cdot (1 - \cos\theta_h),$$

$$Q^2 = E_h^2 \cdot \frac{\sin^2\theta_h}{1-y},$$

$$x = \frac{E_h}{2E_p} \cdot \frac{1+\cos\theta_h}{1-y},$$

where E_h is the the energy of the hadronic system and θ_h is the production angle between the central axis of the hadron system, X_h, and the z axis. This method is used when the information on the scattered electron is not available (i.e. in charged current reactions).

The Jacquet-Blondel method. The hadron variables can be approximately determined by summing the energies (E_h) and transverse (p_{Th}) and longitudinal momenta (p_{zh}) of all hadronic final states. The method rests on the assumption that the transverse momentum carried by those hadrons which escape detection through the beam-hole can be neglected. The result is:

$$y_{JB} = \frac{\sum_h (E_h - p_{zh})}{2E_e},$$

$$Q^2_{JB} = \frac{(\sum_h p_{xh})^2 + (\sum_h p_{yh})^2}{1 - y_{JB}},$$

$$x_{JB} = \frac{Q^2_{JB}}{s y_{JB}}.$$

The double-angle method. It uses the electron scattering angle and the angle γ_h connected with the longitudinal and transverse flow of the hadronic system (in the naive parton model γ_h is the scattering angle of the struck quark):

$$\cos\gamma_h = \frac{(\sum_h p_{xh})^2 + (\sum_h p_{yh})^2 - (\sum_h (E_h - p_{zh}))^2}{(\sum_h p_{xh})^2 + (\sum_h p_{yh})^2 + (\sum_h (E_h - p_{zh}))^2},$$

$$Q^2_{DA} = \frac{4E_e^2 \sin\gamma_h (1+\cos\theta_{e'})}{\sin\gamma_h + \sin\theta_{e'} - \sin(\gamma_h + \theta_{e'})},$$

$$x_{DA} = \frac{E_e}{E_p} \frac{\sin\gamma_h + \sin\theta_{e'} + \sin(\gamma_h + \theta_{e'})}{\sin\gamma_h + \sin\theta_{e'} - \sin(\gamma_h + \theta_{e'})},$$

$$y_{DA} = \frac{Q^2_{DA}}{s x_{DA}}.$$

As the double-angle method relies on ratios of energies, it is less sensitive to the scale uncertainty in the measurement of the energy of the final state particles.

1.3 The structure functions and the quark-parton model

In the approximation of single boson exchange, the cross section of lepton-hadron scattering can be factorized considering the interaction at the lepton vertex and at the hadron vertex separately. The emission of the virtual photon can be calculated exactly from QED, while the hadronic interaction is parametrized in terms of structure functions which depend on the parton densities of the target. Neglecting the proton mass, the cross section can then be written as:

$$\frac{d\sigma(e^{\pm}p \to e^{\pm}X)}{dxdQ^2} = \frac{4\pi\alpha^2}{xQ^4}\left[\left(1 - y + \frac{y^2}{2}\right)F_2(x,Q^2) - \Delta_L \pm \Delta_3\right], \qquad (1.9)$$

with

$$\Delta_L = \frac{y^2}{2}F_L(x,Q^2), \qquad \Delta_3 = \frac{y^2}{2}xF_3(x,Q^2) \qquad (1.10)$$

where α is the electromagnetic coupling constant.

The structure function F_L is related to the coupling of longitudinally polarized photons to the quarks, while F_2 receives contributions both from transverse and longitudinally polarized photons. For both these structure functions parity is conserved. F_3 results from the weak interaction (Z^0 exchange) and therefore violates parity.

Using leptons as probes of the proton structure functions, only the electrically charged constituents of the proton are scattered. The Quark Parton Model (QPM) gives a simple description of the hadrons in terms of partons. According to the parton model of Feynman, the hadrons consist of free $\frac{1}{2}$-spin point-like constituents, called partons. The cross section of inelastic ep scattering is then given by the sum of elastic electron-quark scattering cross sections

$$\frac{d\sigma_{eq}}{dQ^2} = \frac{4\pi\alpha^2 e_q^2}{xQ^4}\left(1 - y + \frac{y^2}{2}\right), \qquad (1.11)$$

The cross section in ep scattering can then be computed by summing over all quarks of type q weighted by the probability of finding the quark q carrying

a fraction x of the proton momentum:

$$\frac{d\sigma_{ep}}{dxdQ^2} = \sum_q e_q^2 f_q(x) \frac{d\sigma_{eq}}{dQ^2} \tag{1.12}$$

where e_q is the electric charge of the q-th struck-parton. In this model, the parton densities $f_q(x)$ are related to the structure functions of the proton by:

$$F_2(x) = \sum_q e_q^2 f_q(x) \qquad \text{and} \qquad F_L = 0 \tag{1.13}$$

In the DIS limit, where $Q^2 \to \infty$ and x is fixed, the structure functions obey a scaling law and depend only on the dimensionless Bjorken variable x. Bjorken scaling implies that the virtual photon scatters off point-like constituents, otherwise the dimensionless structure functions would depend on the ratio Q/Q_0 with $1/Q_0$ being some length scale characterizing the size of the constituents.

The modern theory of the strong interactions is the Quantum Chromodynamics (QCD), a non-abelian gauge theory based on the SU(3) symmetry group, which describes the interaction between quarks and gluons. Each quark has three possible charges related to the colour quantum number and the interaction is mediated via the exchangee of eight different coloured gauge bosons, the gluons. The gluons always carry a combination of colour and anti-colour and the emission of a gluon changes the colour member of the quark. Since the symmetry group of the colour quantum number $(\mathrm{SU}(3)_c)$ is non-abelian, the gluons can couple each other. The gluon self-coupling is the reason for the strong (QCD) coupling constant α_s to become large at low energies and to decrease at high energies. The "running" of α_s determines that at low energies the strength of the colour field is increasing and in this way the quarks and gluons can never be observed as free particles ("confinement"). At high energies, the strength of the colour field decreases and the quarks and gluons behave as essentially free, allowing the application of non-perturbative theory ("asymptotic freedom").

In QCD, the naive QPM needs to be modified due to the coupling of quarks to gluons. Quarks may radiate gluons which in turn can split into $q\bar{q}$ pairs (*sea quarks*). In this case the number of partons increases while the average momentum per parton decreases. With increasing Q^2 more and more of these fluctuation can be resolved. In the low Q^2 region, the valence quarks which have relatively large x values dominate. At large-Q^2 values gluon radiation leads to an increase of the number of quarks with low-x values and correspondingly to a depletion of the high-x region. In fact, at low-x a rapid increase of F_2 with increasing Q^2 has been observed while F_2 decreases at large values of x (see fig. 1.3). This Q^2 dependence of F_2 for fixed x is known as scaling violation.

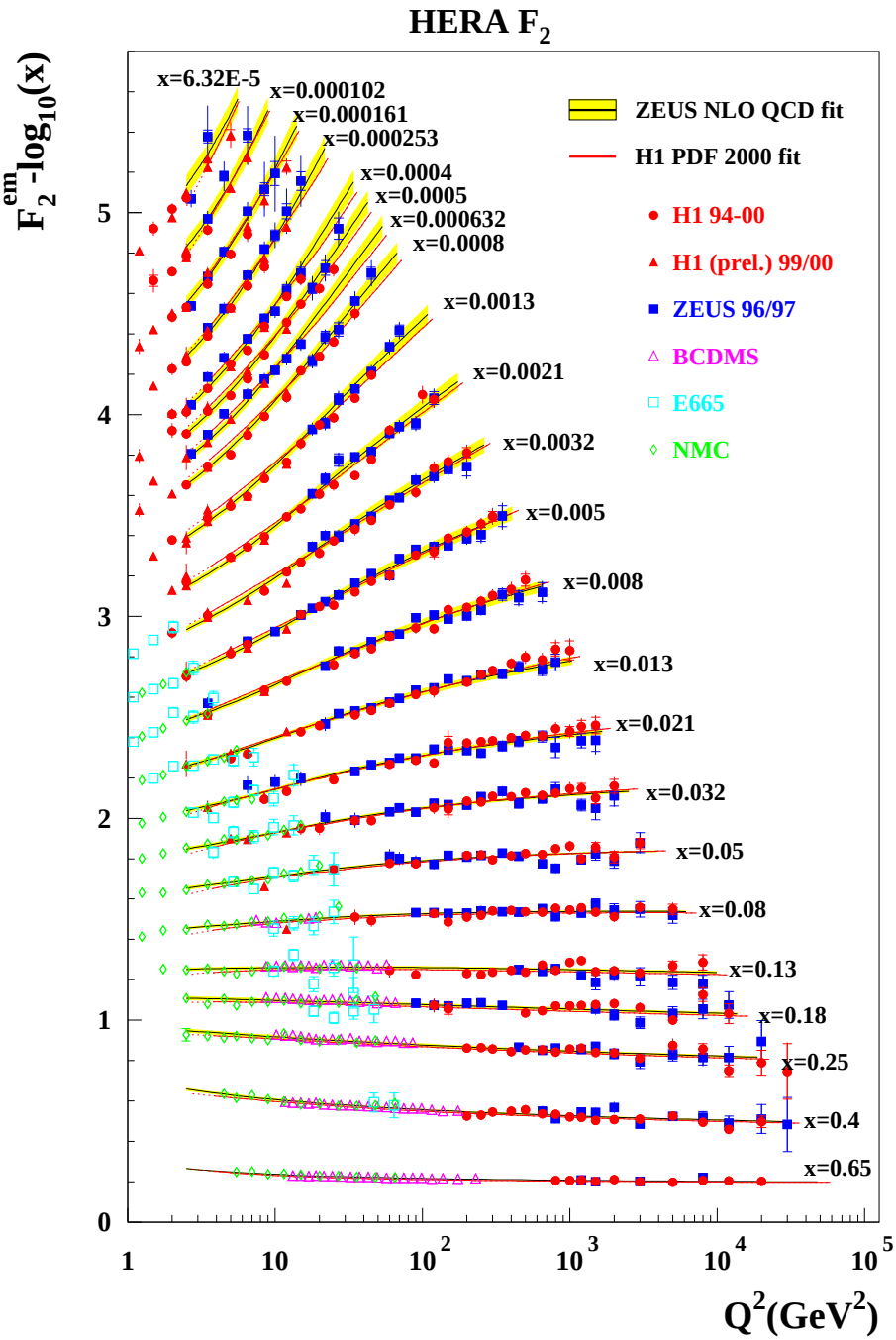

Figure 1.3: *Measurements of the proton structure function F_2 as a function of Q^2 at x fixed values, from ZEUS, H1 and fixed-target experiments. The prediction of DGLAP evolution equations (eqs. 1.14 and 1.15)* are in excellent agreement with the data.

1.4 The evolution equations

The structure functions can not be calculated from perturbative QCD (pQCD). However, the evolution of the structure functions with Q^2 is dominantly a perturbative effect and the predictions of the Q^2 evolution can be therefore based on QCD calculations and provide a test of QCD. The Q^2 evolution of the quark $q_i(x, Q^2)$ and gluon $g(x, Q^2)$ density distributions in pQCD is governed by the Dokshitz-Gribov-Lipatov-Altarelli-Parisi (DGLAP) equations [16], which at the leading order in the running QCD coupling constant $\alpha_s(Q^2)$ are given by:

$$\frac{dq_i(x,Q^2)}{d\ln Q^2} = \frac{\alpha_S(Q^2)}{2\pi}\int_x^1 \frac{dy}{y}\left[P_{qq}\left(\frac{x}{y}\right)q_i(y,Q^2) + P_{qg}\left(\frac{x}{y}\right)g(y,Q^2)\right], \tag{1.14}$$

$$\frac{dg(x,Q^2)}{d\ln Q^2} = \frac{\alpha_S(Q^2)}{2\pi}\int_x^1 \frac{dy}{y}\left[\sum_j P_{gq}\left(\frac{x}{y}\right)q_j(y,Q^2) + P_{gg}\left(\frac{x}{y}\right)g(y,Q^2)\right].$$

At high Q^2 partons can split to form additional partons or additional partons can be created by gluon radiation. The rate at which these additional partons are created is described by the parton splitting functions P_{ij}. They represent the probability of a parton j emitting a parton i with momentum fraction z of the parent parton when the scale changes by $d\log Q^2$. The splitting functions cover four cases: a quark emits a gluon (P_{qg}) or a quark (P_{qq}) and a gluon emits a gluon (P_{gg}) or a quark (P_{gq}). These splitting functions can be calculated in pQCD and are given to first order by:

$$P_{qq}(z) = \frac{4}{3}\frac{1+z^2}{1-z}, \tag{1.15}$$

$$P_{qg}(z) = \frac{1}{2}\left[z^2 + (1-z)^2\right], \tag{1.16}$$

$$P_{gq}(z) = \frac{4}{3}\frac{1+(1-z)^2}{z}, \tag{1.17}$$

$$P_{gg}(z) = 6\left[\frac{z}{1-z} + \frac{1-z}{z} + z(1-z)\right]. \tag{1.18}$$

If the parton distribution function $f_i(x, Q^2)$ is measured over a range from x up to 1 at a fixed scale Q_0^2, then f_i can be predicted for any $Q^2 \neq Q_0^2$ within this range of x. Figure 1.3 shows how well the DGLAP equations describe the evolution of the structure functions measured at HERA [17–19] and fixed-target experiments.

1.5 Diffraction

The term diffraction was introduced in nuclear physics in the 50's of last century by Landau and Pomeranchuk [20]. The high energy diffractive reactions are characterized by the presence of large rapidity[1] gaps in the final state and by the exchange of vacuum quantum numbers.

Hadronic diffraction has always been classified as a *soft* process, in the sense that it has an energy scale of the hadron size $R(\sim 1$ fm). In these interactions the squared momentum transfer is generally small, $|t| \sim 1/R^2$ (few hundred MeV)^2, and the t-dependence cross section is exponential ($d\sigma/dt \sim e^{-R^2|t|}$).

On the contrary, the Diffractive Deep Inelastic Scattering (DDIS) has both *soft* and *hard* properties. Indeed these precesses are characterized by a *hard* scale given by Q^2 and a *soft* scale, typical of diffractive scattering.

The Diffractive DIS events with a large rapidity gap were first observd by the HERA experiment ZEUS [21] and H1 [22]. In standard DIS the rapidity gaps between the proton remnant and the current jet are exponentially suppressed due to the parton radiation in the resulting QCD colour field. In diffractive events a colour singlet object is exchanged and the parton radiation between the current jet and the proton remnant is strongly suppressed.

DDIS events are usually selected in two ways: either select events with a large rapidity gap between the beam-pipe (where the proton is normally lost) and the first hadronic deposit, or record the diffractively scattered proton in a specially designed detector, like the ZEUS Leading Proton Spectrometer (chapter 3). In addition, the mass distribution of the hadronic system M_x can be used to separate the diffractive part from DIS peak [23].

Diffraction is mostly described by the picture of a colorless exchange between the virtual photon and the proton. The exchanged object is called *Pomeron* (*IP*). A diffractive event is illustrated in fig 1.4.

To describe the diffractive events it is useful to define the following variables:

$$x_L = \frac{E_{p'}}{E_p}, \qquad p_T^2 = p_{xp'}^2 + p_{yp'}^2, \tag{1.19}$$

$$t = (p - p')^2 = -\frac{p_T^2}{x_L} - m_p^2 \frac{(1 - x_L)^2}{x_L}, \tag{1.20}$$

$$x_{IP} = \frac{M_X^2 + Q^2 - t}{Q^2 + W^2 + m_p^2} \simeq 1 - x_L, \tag{1.21}$$

$$\beta = \frac{x}{x_{IP}} \simeq \frac{Q^2}{Q^2 + M_X^2}, \tag{1.22}$$

where the primed variables refer to the final state proton.

[1] The rapidity is defined by $\eta = -\ln(\frac{E+p_z}{E-p_z})$

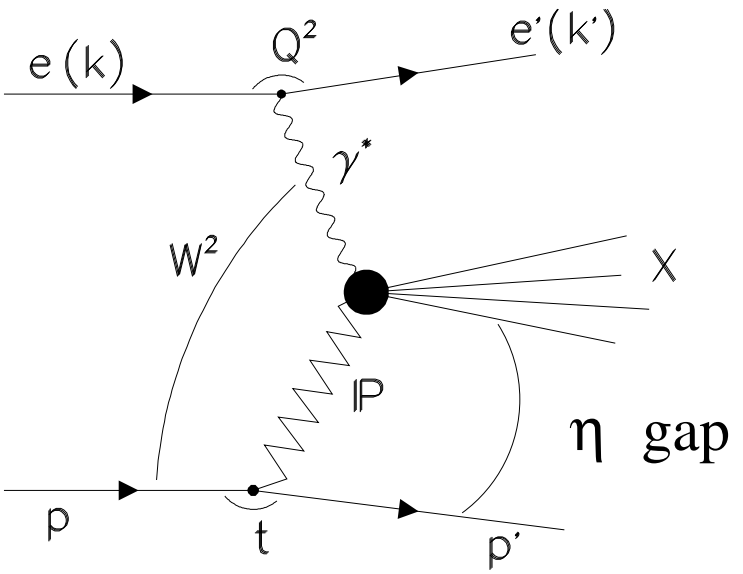

Figure 1.4: *Feynman diagram of a diffractive DIS event.*

In the picture of diffraction mediated by the exchange of a *IP*, x_{IP} gives the fraction of the proton momentum carried by the *IP*. If the Pomeron is viewed as a hadronic object with a partonic substructure, the variable β is equivalent to x in the ordinary DIS reaction and, in the Pomeron rest frame, gives the momentum fraction of the *IP* carried by the struck parton in the diffractive scattering process. The cross section for diffractive scattering can then be written in terms of a diffractive structure function $F_2^{D(4)}$:

$$\frac{d^4\sigma}{d\beta dQ^2 dx_{IP} dt} = \frac{4\pi\alpha^2}{\beta Q^4}\left(1 - y + \frac{y^2}{2}\right) F_2^{D(4)}(\beta, Q^2, x_{IP}, t) \tag{1.23}$$

where the longitudinal and parity-violating terms were neglected.

In the model of Ingelman and Schlein [24] the diffractive scattering is described in two steps: first the proton emits a Pomeron, then the Pomeron is hard scattered by the virtual photon. In this picture, the Pomeron has a partonic structure. The diffractive structure function F_2^D factorizes as:

$$F_2^{D(4)}(\beta, Q^2, x_{IP}, t) = f_{pIP}(x_{IP}, t) F_2^{IP}(\beta, Q^2) \tag{1.24}$$

where f_{pIP} is the the probability for finding a Pomeron in the proton and F_2^{IP} is the Pomeron structure function.

So far, there is no model which describes all aspects of diffractive DIS correctly. This difficulty arises from the fact that diffractive type of reactions combine soft physics, described by phenomenological models, and hard physics, which can be calculated by perturbative QCD. The Regge exchange

picture is related to leading-baryon production and will be described in section 1.6.1. The other diffractive phenomenological models will be discussed in the Event Simulation section (chapter 4).

1.6 Leading-baryon physics

In the framework of QCD the study of leading-baryon production represents an important field of investigation. Indeed leading-baryons carry a significant fraction of the initial momentum x_L and have low transverse momentum, therefore covering kinematic regions of the phace space not accessible from other processes. Due to difficulty of detecting the leading particles in high energy physics experiment, the data available are scarce.

Leading-baryon production has been studied in hadronic collisions, both at the ISR [2, 3] and in fixed-target experiments [4, 5]. Recently, measurements of leading-baryon production had been performed also at HERA [6–8, 25].

From the theoretical point of view, the leading-baryon production mechanism is still not completely understood. There are several models that try to explain the leading-baryon production. In analogy to the DIS and DDIS formalism, the cross section of leading-baryon production can be formulated in terms of leading-baryon structure functions $F_2^{LB(4)}$:

$$\frac{d^4\sigma^{LB}}{dxdQ^2dx_Ldp_T^2} = \frac{4\pi\alpha^2}{xQ^4}\left(1 - y + \frac{y^2}{2}\right) F_2^{LB(4)}(x, Q^2, x_L, p_T^2)(1 + \Delta_{LB}), \tag{1.25}$$

were Δ_{LB} takes into account the effect of the longitudinal structure function F_L and the violating parity terms arising from the Z^0 exchange contribution (eq. 1.9).

Within this formalism the leading-baryon production can be set into a more general framework, consisting of all structure functions measured at HERA.

An alternative model to describe the leading-baryon production is based on the Regge formalism, in which the leading-baryons are produced via the exchange of a particle mediating the interaction. Another picture is given by the Fracture Functions formalism, where the leading particles production is described in terms of structure functions of the fragmented nucleon. The leading particle production is also closely related to the nucleon fragmentation and parton hadronization: these models are widely used in the Monte Carlo simulation programs.

Another reason of interest in leading-baryon production comes from the fact that the ISR data revealed universality features of the hadronic final state produced in electro-weak and strong interactions if the hadronic systems are analysed in terms of the effective energy available for hadronization.

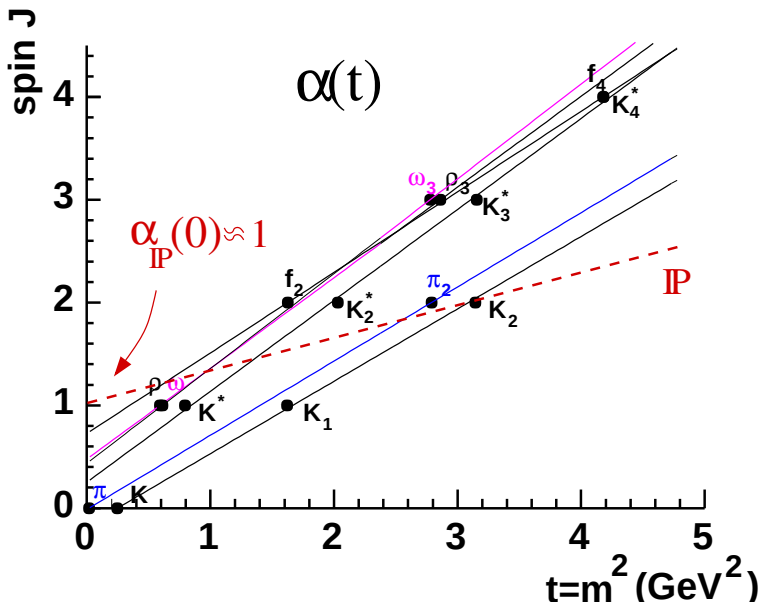

Figure 1.5: *Chew-Frautschi plane of the Reggeon trajectories. The regge poles with quantum numbers of mesons are plotted for spin J versus the squared mass. The lines are linear fits and correspond to the Regge trajectories.*

1.6.1 The Regge phenomenology

Regge theory [26] gives a good description of soft hadronic interactions and can explain the leading-baryon production mechanism, as explained by Szczurek et al. in [27] . In the Regge picture the interactions are mediated by exchanged particles that lie on linear trajectories in the complex $J-t$ plane (the so called Chew-Frautschi plane [28], shown in fig 1.5), where J is the angular momentum and t the virtuality of the exchanged particle. The trajectory $\alpha(t)$ is a continous function defined in the $J-t$ plane and its poles determine the particles mediating the interaction (namely the *Reggeon IR*). The cross section results from the sums of all possibles exchanges consistent with the exchanged quantum numbers. In the high squared energy s limit and at fixed t the scattering amplitude for each Regge pole can be written as:

$$A(s,t) \sim \beta(t) \left(\frac{s}{s_0}\right)^{\alpha(t)}, \tag{1.26}$$

where $s_0 \simeq 1$ GeV^2 is the hadronic mass scale. The differential cross section is then

$$\frac{d\sigma}{dt} = \frac{1}{s^2}|A(s,t)|^2 = F(t) \left(\frac{s}{s_0}\right)^{2\alpha(t)-2}, \tag{1.27}$$

where $F(t)$ is proportional to the squared residual function $\beta(t)$, and the total cross section is, according to the optical theorem,

$$\sigma_T = \frac{1}{s} Im[A(s, t = 0)] \propto \left(\frac{s}{s_0}\right)^{\alpha(0)-1} . \tag{1.28}$$

In this case $\alpha(t)$ is the dominant trajectory that can be exchanged in the elastic scattering.

The Regge scattering model was extended to the case, where the *IR* has a partonic substructure. The process then factorizes into a part that describes the emission of a *IR* from the proton and a part which models its interaction with the virtual photon. In this model the Reggeon behaves like any other hadron, having its structure function and parton densities.

Reggeon exchange

The leading-baryon production can be explained by the exchange of the Reggeon trajectory. The virtual exchanged particles can be neutral isoscalar and isovector (π^0, ρ^0, IP) or charged isoscalar ($\pi^+, \rho^+, \dots$). The parametrisation of the Reggeon flux is:

$$f_{IR}(x_L, t) \propto (1 - x_L)^{1-2\alpha_{IR}(t)} G_{IR} \tag{1.29}$$

with $G_{IR} = G_0 \exp(B_{IR} t)$ being the Reggeon form factor. G_0 and B_{IR} are two parameters, calculated from the Regge analysis of hadronic elastic scattering.

Pomeron exchange

The Pomeron is an object having vacuum quantum number and it was introduced to explain the diffractive scattering. Indeed for many reactions the cross sections result to be approximately constant in a wide range of s values and then grows slowly at high energies. This behavior implies a dominant trajectory with $\alpha(0) \simeq 1$ and vacuum quantum numbers. There is no trajectory with these characteristics, corresponding to experimentally observed particles and resonances. Therefore, it was necessary to introduce the Pomeron trajectory, α_{IP} with $\alpha_{IP}(0) = 1$ and with vacuum quantum number [29].

The process mediated by the Pomeron exchange produces only leading protons. The Pomeron exchange dominates at $x_L \simeq 1$.

The flux factor for this process is written like in eq. 1.29:

$$f_{IP}(x_L, t) \propto (1 - x_L)^{1-2\alpha_{IP}(t)} G_{IP} \tag{1.30}$$

with $G_{IP} = G_0 \exp(B_{IP} t)$ being the Pomeron form factor. G_0 and B_{IP} are two parameters, calculated from Regge analysis of hadronic diffractive scattering.

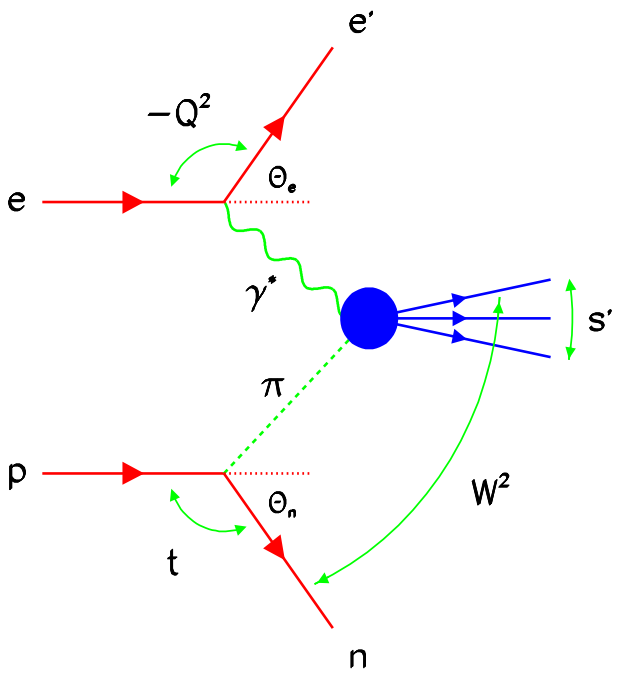

Figure 1.6: *Diagram describing the One-Pion-Exchange mechanism with the production of a leading-neutron.*

Sometimes, after the interaction with the Pomeron, the scattered proton can dissociate in a low mass state N carrying a large fraction of the initial proton longitudinal momentum (proton-dissociative diffraction [30]), that subsequently decays into a leading-proton with $x_L < 1$. Therefore Pomeron exchange can also induce leading-proton production at $x_L < 1$.

One-Pion-Exchange model (OPE)

This One-Pion-Exchange model [31] describes the process in which a leading-neutron is produced (fig. 1.6). In fact, the pion, due to its small mass, dominates the $p \to n$ transition amplitude, with its relative contribution increasing as $|t|$ decreases. The flux factor describing the splitting of the proton in a πN system (N being a nucleon) is

$$f_{\pi N}(x_L, t) \propto \frac{-t}{(t - m_\pi^2)^2}(1 - x_L)^{1-2\alpha_\pi(t)}[F_\pi(x_L, t)]^2, \qquad (1.31)$$

where the form factor $F_\pi(x_L, t)$ parametrises the distribution of the pion cloud in the proton and accounts for final-state rescattering of the neutron.

1.6.2 The Fracture Functions

The Fracture Functions [32] were introduced to extend the usual QCD-improved parton description of semi-inclusive DIS to the low transverse momentum region of phase space, where the target fragmentation contribution becomes important.

In the QCD parton model experimental cross-section can be computed by convoluting some uncalculable process-independent quantities with calculable process-dependent elementary cross sections.

Let us consider a general lepton-nucleon DIS process $l + N \to l' + h + H + X$. In the final state the hadronic system X and H are originated from the target fragmentation and from the hard interaction, respectively, and h is a singled out hadron. This process will receive contributions from two well separated kinematical regions for the produced hadron h:

$$\begin{aligned} \sigma_{l+N\to l'+h+H+X} &= \sigma_{current} + \sigma_{target} = \\ &= \sigma_{l+N\to l'+(h+H)+X} + \sigma_{l+N\to l'+H+(h+X)}, \end{aligned} \quad (1.32)$$

In the first term, apart the factor arising from target structure function, no knowledge other than the one of the fragmentation function is needed. The description of the second term does require a new non-perturbative (but measurable) quantity, a fragmentation-structure or "fracture" function:

$$\sigma_{target} = \int_0^{1-z} \frac{dx}{x} M^i_{N,h}(z, x; Q^2) \sigma^i_{hard}(x, Q^2). \quad (1.33)$$

In this form the factorization describes the full target fragmentation in terms of the single function M, without separating the contributions of the active parton and that of the spectators. The fracture functions tell about the *structure* function of the target hadron once it has *fragmented* into a specific final state hadron. M measures the parton distribution of the object exchanged between the target and the final hadron, without any model about what that object actually it is. Hence the fracture function model provides an alternative tool, in the framework of QCD, to that based on Regge factorization.

1.6.3 Proton remnant fragmentation in the Lund Model

The remnant system is broadly defined as the target nucleon "minus" the parton entering the hard scattering. The latter can be either a valence quark, a sea-quark or a gluon (boson-gluon fusion process).

When the interacting parton is a valence quark, the nucleon remnant is a diquark composed of the two left-over valence quarks as spectators. In the Lund model [33] a colour triplet string is stretched between the colour triplet charged struck quark and the diquark, that is a colour antitriplet. The system is then hadronized by the production of quark-antiquark and

diquark-antidiquark pairs from the energy in the string field, leading to hadron production. Assuming the leading-baryon number conservation, the leading-baryon is produced by a combination of diquark-quark systems. If the interacting parton is a sea-quark (antiquark) q_s, the nucleon remnant contains the corresponding antiquark (quark) in addition to the three valence quarks q_v. If $\bar{q}_s = \bar{u}$ or $\bar{d}$, it is canceled against the corresponding valence quark leaving a simple diquark system to be treated as above. For other flavours the sea-quark $\bar{q}_s$ forms a meson ($M = q_v\bar{q}_s$) with the valence quarks. The meson is given a fraction z of the energy-momentum $(E + p_z)$ along the beam direction from a probability distribution $P(z)$ and a small Gaussian distributed transverse momentum $p_\perp$. The left-over diquark, with longitudinal momentum $(1-z)$ and opposite $p_\perp$, forms a string system with the scattered quark and then hadronization is performed as usual. If an antiquark ($\bar{q}_s$) is scattered, then the corresponding quark q_s is combined with a random diquark to form a baryon ($B = q_v q_v q_s$). In both cases the probability distribution $P(z)$ is related to the mass of the remnant subsystems.

In the boson-gluon fusion process the removed gluon leaves the three valence quarks in a colour octet state. This remnant is split into a quark and a diquark, chosen with random flavours, which form two separate strings with the antiquark and quark produced in the fusion process, respectively.

1.7 The Leading Effect and the Effective Energy

It was observed in hadron-hadron collisions that the center of mass (c.m.) energy, $\sqrt{s}$, is shared among different processes: the Effective Energy is that fraction of initial energy "spent" in the hadronization processes [9, 10].

With the introduction of the Effective Energy, it is possible to put on the same basis all high energy processes, like hadron-hadron, lepton-hadron and lepton-lepton collisions. In nature there are some quantities that, when analysed in terms of the Effectve Energy, show the same behaviour whatever the kind of experiment and its nominal energy: Universality Features. In the following it will be shown that the concept of Effective Energy is striclty related to the Leading Effect, since it is possible to compute the Effective Energy from the measurement of the leading particle energy and momentum.

1.7.1 The Effective Energy phenomenology

In proton-proton interactions, the nominal c.m. energy, $\sqrt{s_{pp}}$, can be expressed in terms of the incoming proton beam energy:

$$\sqrt{s_{pp}} = 2E_{inc}, \qquad E_{inc} = E_1 = E_2 \tag{1.34}$$

where E_1 and E_2 are the energies of the colliding protons. After the collision, the two incoming protons keep, on the average, a large fraction

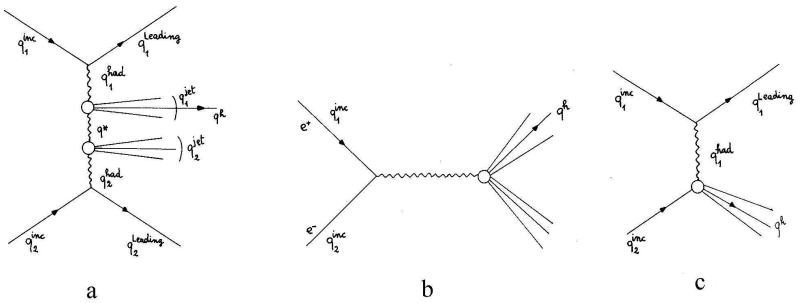

Figure 1.7: *Schematic diagrams for $p-p$ (a), e^+e^- (b) and DIS processes (c).*

of the available energy and play a privileged role in the energy-momentum sharing among the particles in final state. The idea is to subtract the energy carried by each proton in order to obtain, on each hemisphere, the Effective Energy ($E^{had}_{1,2}$) available for the hadronization.

If $q^{inc}_{1,2}$ are the quadrimomenta of the incoming protons, we introduce the relativistic invariant quantity:

$$(q^{inc}_{tot})^2 = (q^{inc}_1 + q^{inc}_2)^2 \tag{1.35}$$

This initial effective total squared mass splits into two effective hadronic systems, described by

$$q^{had}_1 = q^{inc}_1 - q^{lead}_1 \tag{1.36}$$

$$q^{had}_2 = q^{inc}_2 - q^{lead}_2 \tag{1.37}$$

where q^{lead}_i are the quadrimomenta of the two leading protons in each final state and q^{had}_i are the two quadrimomenta associated to the two multihadronic system produced in each hemisphere (fig. 1.7 a) and they are to a first approximation uncorrelated. The Effective Energies come out by projecting the two hadronic system into the total quadrimomentum:

$$E^{had}_1 \simeq \frac{q^{had}_1 \cdot q^{inc}_{tot}}{\sqrt{(q^{inc}_{tot})^2}}, \tag{1.38}$$

$$E^{had}_2 \simeq \frac{q^{had}_2 \cdot q^{inc}_{tot}}{\sqrt{(q^{inc}_{tot})^2}}. \tag{1.39}$$

The physics of each multihadronic system, associated with each quadrimomentum q^{had}_i, allows the validity of the following formulae:

$$E_1^{had} \simeq E_1^{inc} - E_1^{lead}, \tag{1.40}$$

$$E_2^{had} \simeq E_2^{inc} - E_2^{lead}. \tag{1.41}$$

In e^+e^- reactions (fig. 1.7 b) the Effective Energy is equal to the nominal c.m. energy:

$$\sqrt{(q_{tot}^{had})^2} = \sqrt{s_{e^+e^-}}. \tag{1.42}$$

In DIS reactions (fig. 1.7 c) the Effective Energy can be calculed from the quadrimomenta of the leading-proton and of the scattered electron

$$\sqrt{(q_{tot}^{had})^2} = \sqrt{[(k-k') + (p-p')]^2}. \tag{1.43}$$

Now we are in the position to consider the Universality Features; they are measurable quantities related to non-perturbative QCD. These quantities have identical properties, no matter what are the interacting particles in the initial state. A partial list of observables is:

- fractional momentum distribution of the leading particle[2]

$$\frac{d\sigma}{dx_L}; \tag{1.44}$$

- transverse momentum distribution of the leading particle

$$\frac{d\sigma}{dp_T^2}; \tag{1.45}$$

- average number of charged particles

$$\langle n_{ch} \rangle; \tag{1.46}$$

- average fraction of the energy carried by charged particles

$$\frac{\langle E_{ch} \rangle}{E_{tot}}; \tag{1.47}$$

The figures from 1.8 to 1.14 show that the Universality Features measured in different experiments exhibit the same behaviour, confirming the validity of the universality of the hadron production mechanism.

[2]The longitudinal fractional momentum of the leading-proton x_L is used in DIS . In $p-p$ interaction, the variable $x_F = 2p_L/\sqrt{s}$ is preferred.

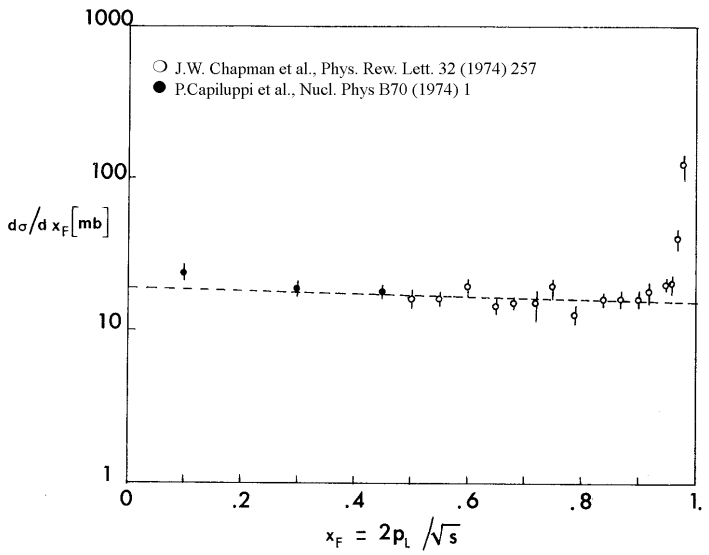

Figure 1.8: *Inclusive differential cross section $d\sigma/dx_F$ as function of x_F in the reaction $pp \to p + X$ at ISR energies [9, 10].*

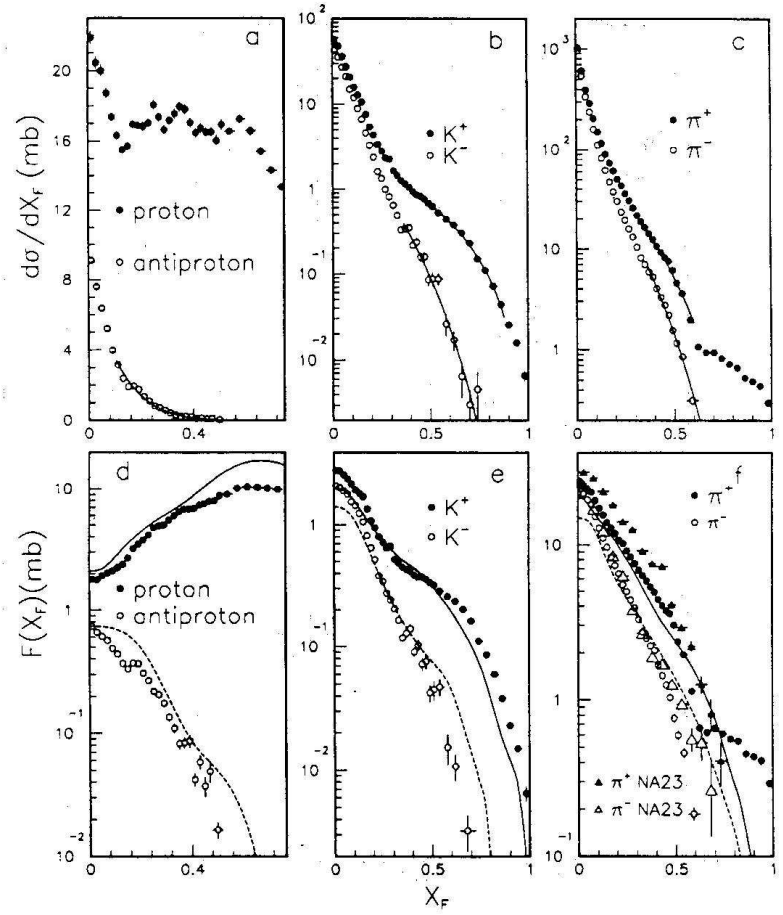

Figure 1.9: *Longitudinal x_F distributions for charged particles in fixed target NA27 experiment with 400 GeV beams [4] . The $d\sigma/dx_F$ (a-c) and $F(x_F)$ (d-f) for proton and antiproton (a, d), charged kaons (b, e) and pions (c, f).*

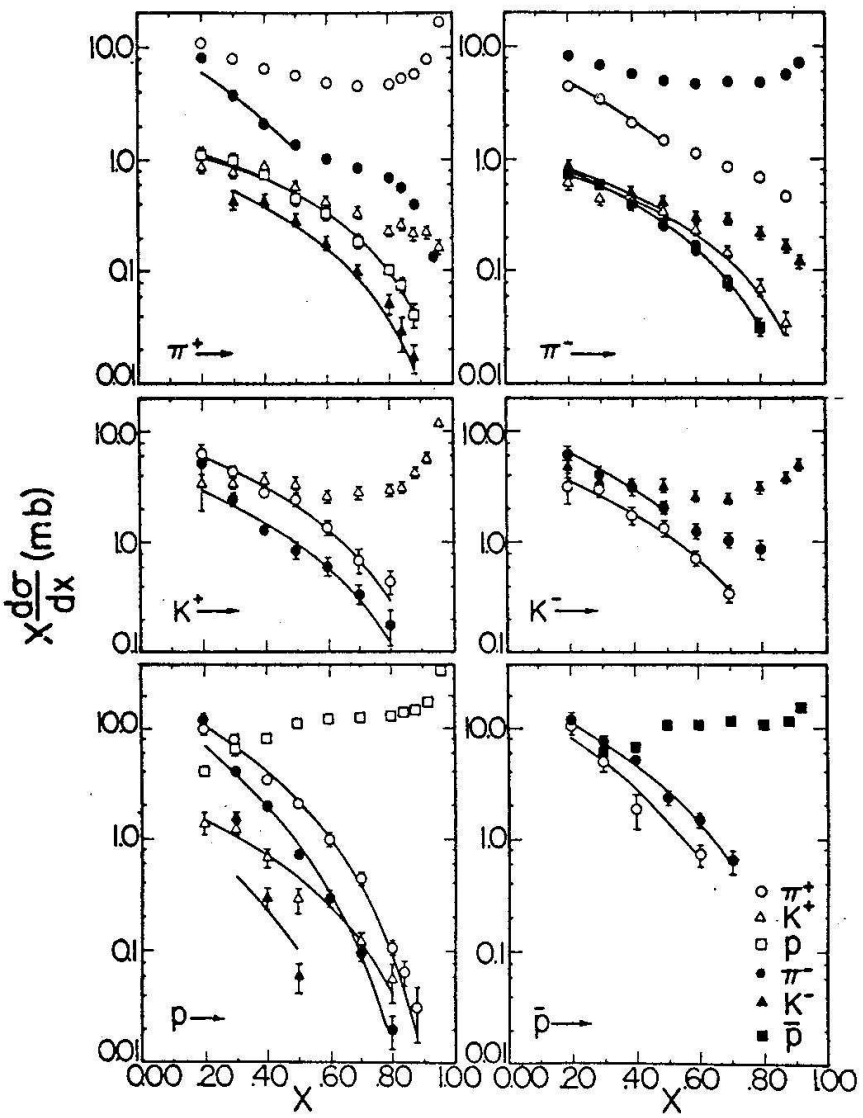

Figure 1.10: *The single differential cross section $xd\sigma/dx$ as a function of x with 100 GeV incident particles (Fermilab-SAS [5]).*

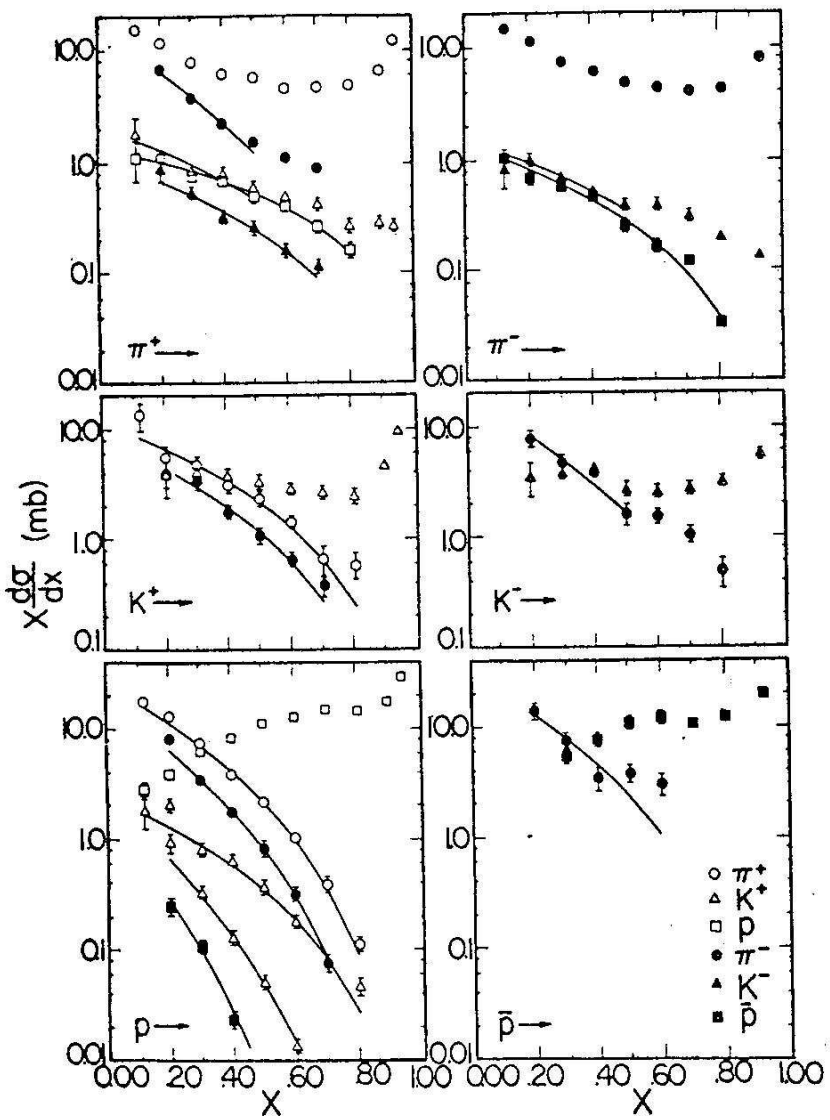

Figure 1.11: *The single differential cross section $xd\sigma/dx$ as a function of x with 175 GeV incident particles (Fermilab-SAS [5]).*

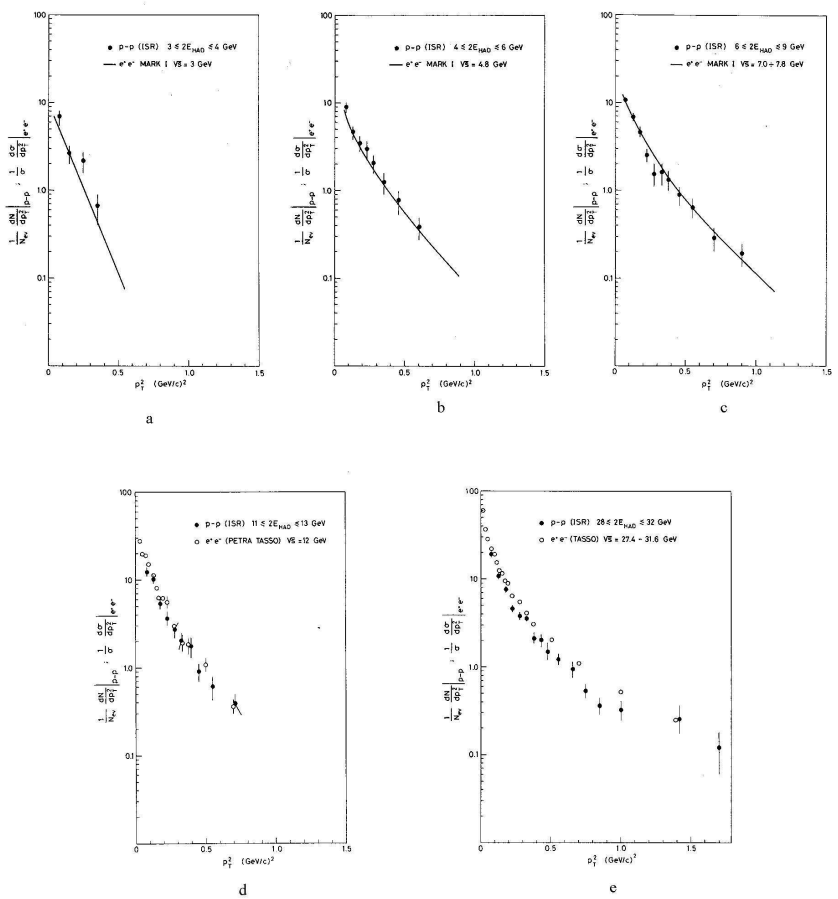

Figure 1.12: *Inclusive single particle transverse momentum distribution for data taken at* ($\sqrt{s_{pp}} = 30$ *GeV and for five different intervals of* $2E^{had}$.

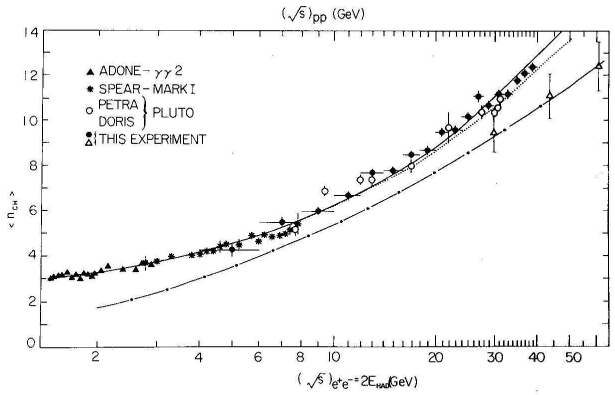

Figure 1.13: *Mean charged-particles multiplicity (averaged on different* $(\sqrt{s_{pp}})$ *versus* $2E^{had}$*, compared with* $e^+ - e^-$ *data. The continuos line is the best fit to the ISR data according to* $\langle E_{ch}\rangle = a + b \cdot \exp[c\sqrt{ln(s/\Lambda^2)}]$*. The dotted line is the best fit using PLUTO data and the dashed-dotted line is the standard* $p - p$ *total charged-particle multiplicity.*

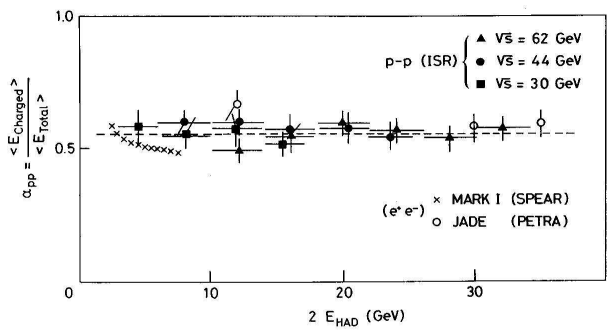

Figure 1.14: *The charged-to-total energy ratio obtained in* $p - p$ *collisions at ISR plotted versus* $2E^{had}$ *and compared with* e^+e^- *results obtained at SPEAR and PETRA.*

Chapter 2

The experimental apparatus

2.1 The HERA collider

The Hadron Electron Ring Anlage, HERA, located at the DESY (Deutsches Elektronen-SYnchrotron) laboratory in Hamburg is the first lepton-proton collider in the world. It was designed to study proton-electron (positron)[1] interactions in a kinematic regime with center-of mass energies one order of magnitude larger than available in previous experiments. In the first period of the HERA running (from 1993 to 1997), electron beams of 27.5 GeV collided on 820 GeV proton beams to achieve an energy $\sqrt{s} = 300$ GeV in the center of mass, that is equivalent to a fixed target experiment using 52 TeV electrons. After a first upgrade of the machine, in 1998, the proton beam energy has been increased up to 920 GeV, the center-of-mass energy $\sqrt{s} = 314$ GeV. Finally, after the 2000 shutdown, the specific luminosity was increased from $3.4 \cdot 10^{29}$ to $1.8 \cdot 10^{30}$ $\mathrm{cm}^{-2}\mathrm{s}^{-1}\mathrm{mA}^{-2}$ and polarized lepton beams are used.

The HERA tunnel has a circumference of 6.3 km and is situated 10-25 m underground. Along the HERA ring, the leptons collide on the protons in two interaction points, where are placed the H1 and ZEUS experiment, respectively in the North and South experimental halls. H1 and ZEUS are two complemetary large multipurpose experiments, designed to study the wide spectrum of HERA physics produced in electron-proton scattering.

Two other experiments are also installed, HERMES (East hall) and HERA-B (West hall). HERMES, installed on the lepton beam, is a polarised gas-jet internal target experiment devoted to mesure the spin distributions of quarks inside protons and neutrons, while HERA-B, that was operating until 2000, was designed to investigate on CP violation in the $B - \bar{B}$ system using an internal (Cu-wire) target in the proton ring.

In figure 2.1 a plan of the HERA collider with its pre-accelerator system

[1] Since in the machine the leptons can be either electrons and positrons, for convenience the word electron (e) will be used to refer either to electrons (e^-) or positrons (e^+).

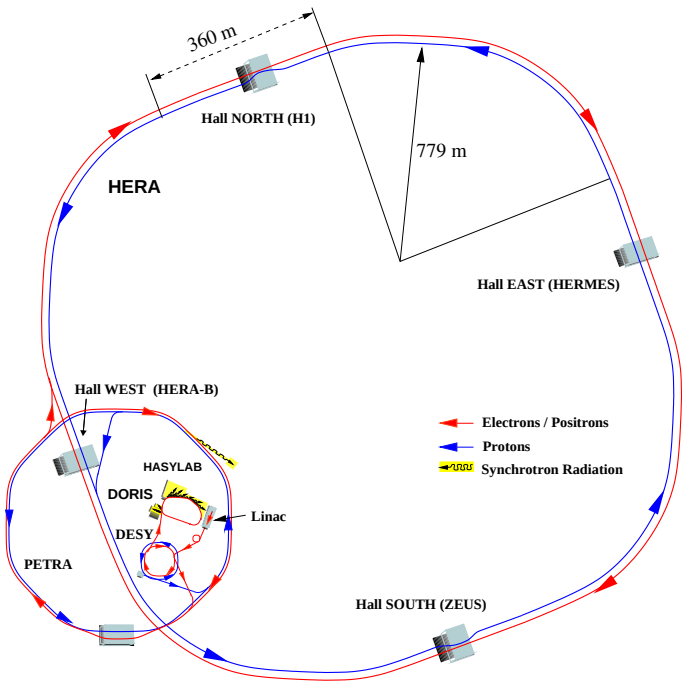

Figure 2.1: *Hera collider scheme with the four experimental halls and the pre-accelerator system.*

and injection scheme is shown.

One of the features that distinguishes HERA from others conventional colliders is the asymmetry in beam energy. While the high momentum of the proton beam requires superconducting magnets, the electrons are controlled with conventional magnets. The HERA proton ring consists of 422 main dipoles delivering a bending field of up to 4.65 T and 244 main quadrupoles. Standard cells of 47 m length combining 4 dipoles, 4 quadrupoles and 4 sextupoles and correction magnets are installed in the arcs of the proton ring and are cooled down to 4.2 K.

The conventional electron ring consist of 456 main dipoles of up to 0.164 T and 605 main quadrupoles grouped in 12 m long magnet modules containing one dipole, one quadrupole, one or two sextupole and several correction dipoles. The bending magnets are C-magnets with the open side of the magnet directed away from the proton beam.

The HERA injection system is based on a chain of pre-accelerators including the ring accelerators DESY and PETRA. The electrons are pre-accelerated in the linear accelerators LINAC I (220 MeV) and LINAC II (450 MeV) followed by an acceleration up to 9.0 GeV in the DESY II Synchrotron. Then the electrons are transfered to PETRA where the energy is increased to 14 GeV after which the leptons are injected into the HERA

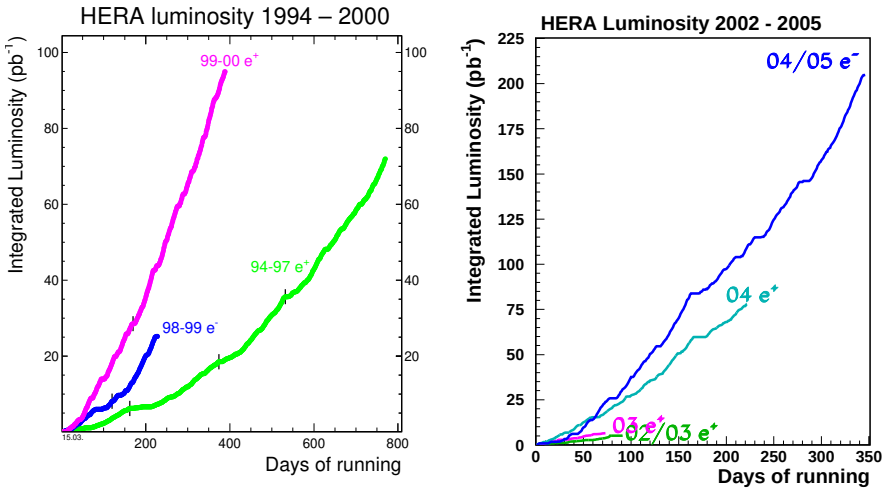

Figure 2.2: *Integrated luminosity delivered by HERA from 1994 to 2005.*

HERA parameters	**Design value**		**1997**	
	e^-	p	e^+	p
Energy (GeV)	30	820	27.5	820
Instantaneous luminosity ($\mathrm{cm^{-2}s^{-1}}$)	$1.5 \cdot 10^{31}$		$1.1 \cdot 10^{31}$	
Specific luminosity ($\mathrm{cm^{-2}s^{-1}(mA)^{-2}}$)	$3.4 \cdot 10^{29}$		$6.0 \cdot 10^{29}$	
Integrated luminosity ($\mathrm{pb^{-1}}$)	30		36.35	
Current (mA)	58	163	30	75
Beam σ_x at the I.P.	0.30	0.27	0.27	0.18
Beam σ_y at the I.P.	0.06	0.09	0.06	0.06
Beam σ_z at the I.P.	0.8	11	0.8	11

Table 2.1: *Hera design parameters and performance in 1997.*

electron ring. The proton injection starts with negative Hydrogen ions (H^-) from the 50 MeV proton LINAC. After the two electron have been stripped off, the protons are accelerated via DESY III and PETRA to 7.5 GeV and 40 GeV, respectively, which is the injection energy for the HERA proton ring.

The electrons and protons are stored in separate bunches with a distance of 28.8 m between two succesives bunches. This distance corresponds to a bunch crossing time of 96 *ns*. In order to achieve an adequate luminosity, each ring can be filled up to 210 bunches of particles. Under standard operation HERA is not filled with all bunches: in this way, the empty ("pilot") bunches are used to study the background related to the beam-gas interactions and cosmic rays.

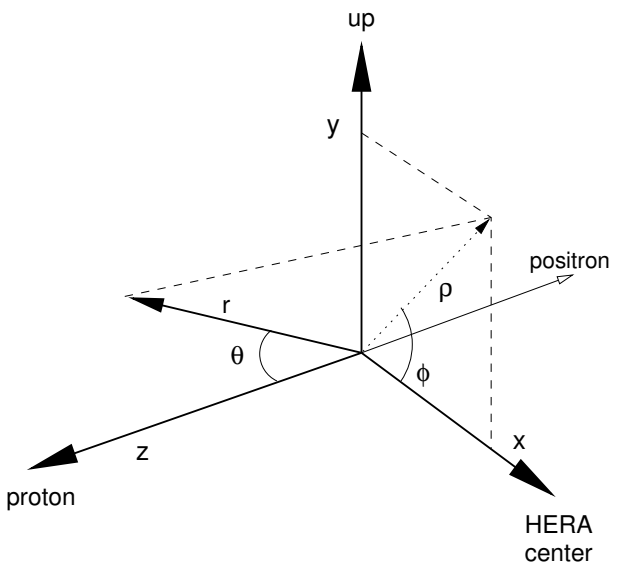

Figure 2.3: *Zeus coordinates system*

In the figure 2.2 the integrated luminosity delivered by HERA is shown. In table 2.1 the main HERA parameters and setting in 1997 are listed.

2.2 The ZEUS detector

The ZEUS detector is a multi-purpose detector which allows the study of final state particles produced in ep collisions. It is an asymmetrical detector to account for the momentum imbalance between the colliding beams. A detailed description of the ZEUS detector can be found in the technical status report [34].

In the ZEUS coordinate system (fig. 2.3) the nominal interaction point is at $(x, y, z) = (0, 0, 0)$. The z-axis points along the directions of proton beam (also called forward direction). The x-axis points towards the center of the HERA ring, the y-axis points upwards. The polar angle θ is measured with respect to the positive z direction and the azimuthal angle ϕ relative to the x-axis. Thus, the polar angles of the proton and electron beams are 0 and 180 degrees, respectively.

Around the interaction point is installed, from 2000, the Micro Vertex Detector [2] (MVD), a high presicion silicon detector designed to reconstruct both primary and secondary vertexes. The ZEUS tracking system consist of the Central Tracking Detector (CTD), in the center of the main detector. Additional tracking information and particle identification in the forward

[2]During 1992-1995 there was installed the Vertex detector (VXD), a cylindrical drift chamber surrounding the beam-pipe.

and rear directions are given by the Forward and Rear Tracking Detector (FTD and RTD). The whole tracking system is enclosed by a superconducting solenoid which provides an axial magnetic field of 1.43 T.

The tracking system is surrounded by a high resolution Uranium Calorimeter (UCAL), which is divided in three sections: the Forward Calorimeter (FCAL), the rear calorimeter (RCAL) and the Barrel Calorimeter (BCAL), enclosing the central region. The Small-angle Rear Tracking Detector (SRTD) is mounted behind the RTD on the face of the RCAL covering an area of 68×68 cm^2 around the rear beam-pipe hole. In front of the RCAL and FCAL, Rear and Forward Presampler detectors (RPRES and FPRES) are installed, consisting of a single layer of scintillator plates. The main calorimeter UCAL is enclosed by muon identification chambers (FMUI, BMUI and RMUI) on the inner side of an iron yoke, which provides the return path for the magnetic field. The yoke also serves as an absorber for the Backing Calorimeter (BAC), which measures the energy leakage from late showering particles. Outside the yoke, the outer muon chambers (FMUO, BMUO, RMUO) are installed. In the forward region, there is a supplementary toroidal magnetic field of 1.7 T. The central ZEUS detector is shown in figures 2.4 and 2.5.

Just behind the RCAL module, a small sampling calorimeter is installed near the beam-pipe to explore the low Q^2 region. This Beam-Pipe Calorimeter (BPC) is accompained by a small Beam-Pipe Tracker (BPT). An iron-scintillator detector (Vetowall) is located at z =-7.3 m behind the main detector to reject beam related background. Further down the electron beam direction (negative z-axis), three lead-scintillator electromagnetic calorimeters are located at z=-34 m, z=-44 m and z=-107 m to measure electrons from photoproduction events ($Q^2 \approx 0$) and photons from bremsstralhung events that are used to determine the luminosity at ZEUS.

In the forward direction (fig. 2.6) a lead-scintillator counter, the Proton Remnant Tagger (PRT), is installed at z=5.1 m around the beam-pipe. Between 20 m and 90 m in the positive z direction, six stations of silicon microstrip detectors of the Leading Proton Spectrometers (LPS) are located to measure the very forward scattered, outgoing proton. The Forward Neutron Calorimeter (FNC) is a lead-scintillator sandwich situated at z=105 m.

The short time spacing of the ep bunches at HERA of 96 ns results in a nominal beam crossing rate of about 10 MHz. To reduce the rate of detected events to the level of a few Hz at which data can be written to tape, ZEUS has a three-level trigger system.

In the following sections a more detailed description of the detector components used in the analisys will be given, and the next chapter is fully dedicated to the Leading Proton Spectrometer, the detector on which this analysis is mainly based.

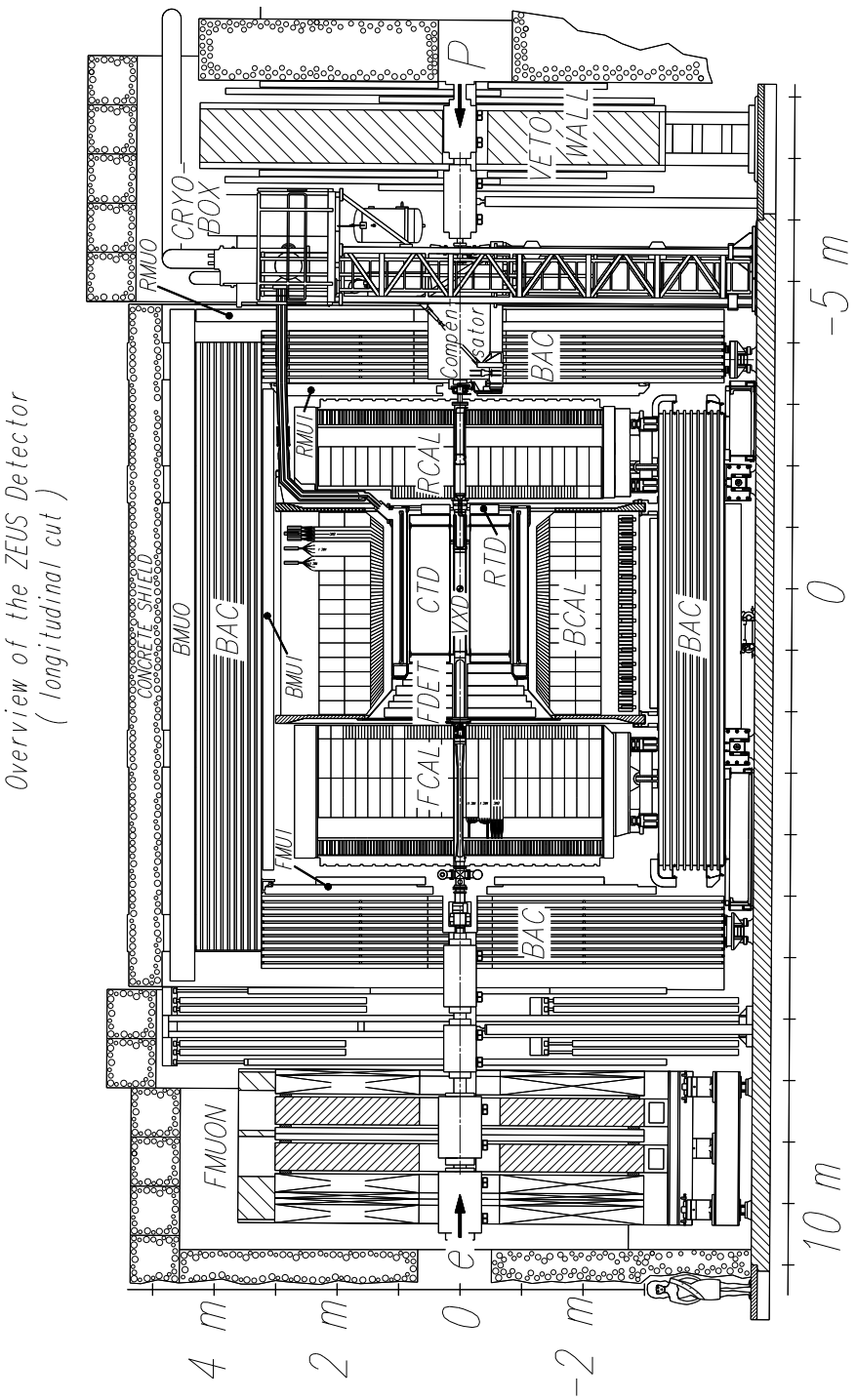

Figure 2.4: *Cross sectional view of the ZEUS detector along the beam direction.*

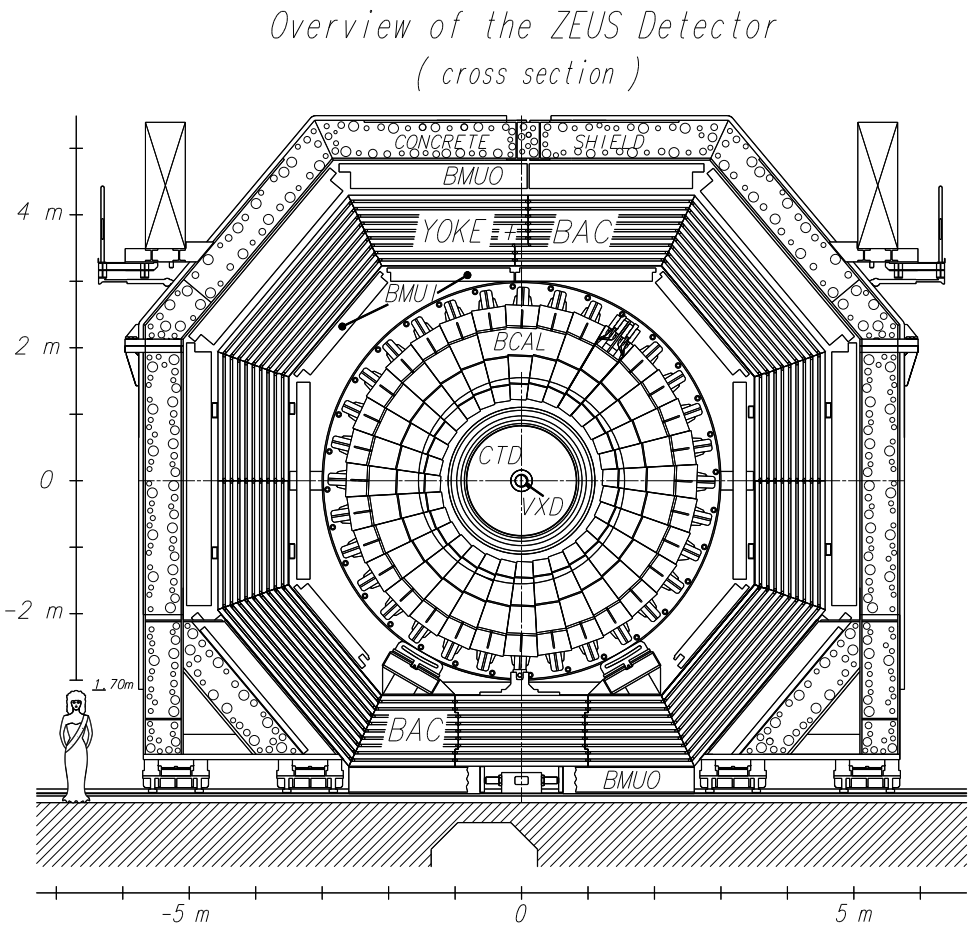

Figure 2.5: *Cross sectional view of the ZEUS detector perpendicular to the beam direction.*

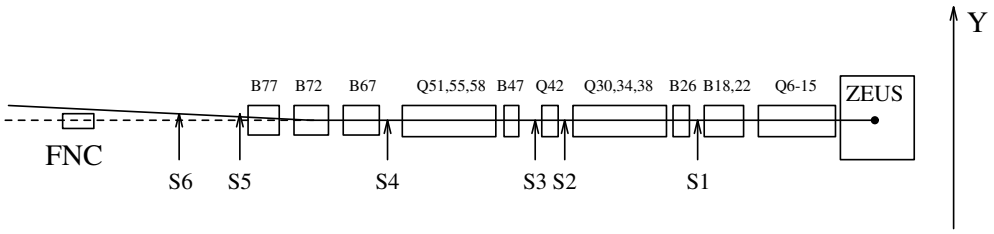

Figure 2.6: *Scheme of the ZEUS forward detectors. S1-S6 are the six stations of the Leading Proton Spectrometer. The elements B and Q are the binding magnets and the quadrupoles magnets, respectively.*

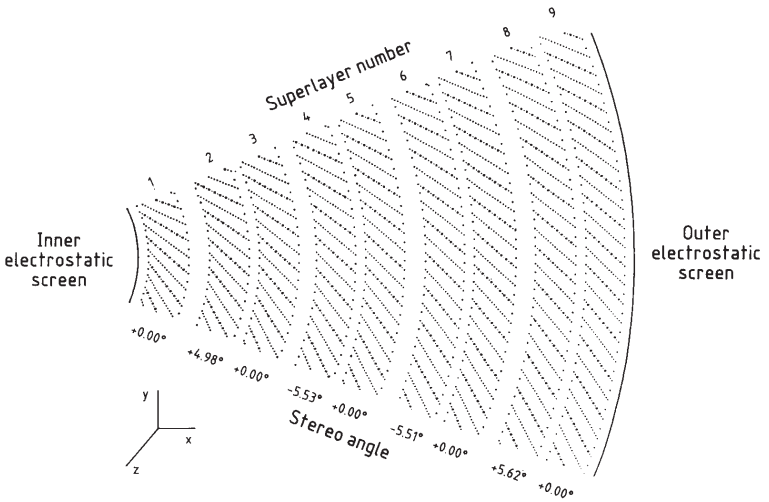

Figure 2.7: *Cross sectional view of a CTD sector.*

2.2.1 The Central Tracking Detector

The Central Tracking Detector (CTD) measures with high precision the direction and momentum of charged particles and gives additional information for particle identification via the mean energy loss dE/dx of charged particles within the gas chamber volume of the detector.

The CTD is a cylindrical drift chamber consisting of 72 layers organized in 9 superlayers. Its active volume gas has a length of 205 cm, with an inner radius of 18.2 cm and an outer radius of 79.4 cm. The fig. 2.7 shows one octant of the wire layout.

This gives a coverage of the polar angle of $15° < \theta < 164°$ (corresponding to $-1.69 < \eta < 2.04$ in pseudorapidity[3]) and a full coverage of the azimuthal angle. The chamber is filled with a mixture of argon, CO_2 and ethane. The superlayers alternate between those which have the wires oriented parallel to the beam axis (axial superlayers carrying odd numbers) and those which have a 5° angle with the beam axis (stereo layers carrying even numbers) allowing the determination of the z position of the hit. The three inner axial superlayers are also instrumented with a z-by-timing system to allow the measurement of the z position from the time difference in the arrival time on both ends of the chamber. The spatial resolution of the CTD is about 230 μm in $r - \phi$, corresponding to a momentum resolution of

$$\frac{\sigma(p)}{p} = 0.005 \cdot p \oplus 0.0016 \tag{2.1}$$

(p in GeV) for long tracks. The interaction vertex is measured on an event-by-event basis with a typical resolution along and transverse to the beam

[3]The pseudorapidity is defined as $\eta = -\ln(\tan\frac{\theta}{2})$ with θ being the polar angle.

axis of 0.4 and 0.1 cm, respectively.

2.2.2 The Uranium Calorimeter

The ZEUS calorimeter (figure 2.8) is subdivided in three parts: BCAL, FCAL and RCAL. The Barrel calorimeter (BCAL) covers the polar angle θ from 36.7° to 129.1° (corresponding to $-0.74 < \eta < 1.1$); the Forward Calorimeter (FCAL), the polar angle between 2.2° and 39.9° (corresponding to $1.0 < \eta < 4.0$); and the Rear Calorimeter (RCAL), the polar angle between 128.1° and 176.5° (corresponding to $-3.49 < \eta < -0.72$).

The UCAL is a sampling calorimeter consisting of alternating layers of 3.3 mm thick depleted uranium as an absorber and 2.6 mm thick plastic scintillator plates (SCSN-38). The thickness of these materials was chosen so that the calorimeter provides compensation, i.e., the response of the calorimeter to electrons (e) and hadrons (h) of equal energies is the same ($e/h = 1.00 \pm 0.02$). This is important for the energy resolution of the hadronic energy, since hadronic showers have a statistically fluctuating electromagnetic component. Under test beam conditions, the resolution of the calorimeter was measured to be for hadrons:

$$\frac{\sigma_h(E)}{E} = \frac{0.35}{\sqrt{E}}, \tag{2.2}$$

and for electrons:

$$\frac{\sigma_e(E)}{E} = \frac{0.18}{\sqrt{E}}, \tag{2.3}$$

with the energy E in GeV.

The three sections of the calorimeter are divided in modules (figure 2.9 shows a module of FCAL), which are oriented perpendicular to the beam axis in the BCAL and longitudinal to the beam axis for FCAL and RCAL. Each module is subdivided into towers of dimensions 20×20 cm^2 . Each tower has a longitudinal structure of one electromagnetic section (EMC) and two (one in RCAL) hadronic sections (HAC1, HAC2). Every EMC section consists of four 5×20 cm^2 cells (two 10×20 cm^2 in RCAL) to give a fine segmentation for electron reconstruction. Each cell of the calorimeter is read out on two sides by wavelength shifters, which are coupled to photomultipliers tubes (PMT). The energy corresponds to the sum of both PMTs and is therefore indipendent of the impact point of the particle on the cell. However, a comparison of both PMTs allows to determine a position reconstruction within a cell. Besides the energy measurement, the UCAL gives very precise timing information with a resolution for a single cell of better than

$$\sigma(t) = \frac{1.5}{\sqrt{E}} \oplus 0.5\ ns \tag{2.4}$$

for energy deposits over 3 GeV.

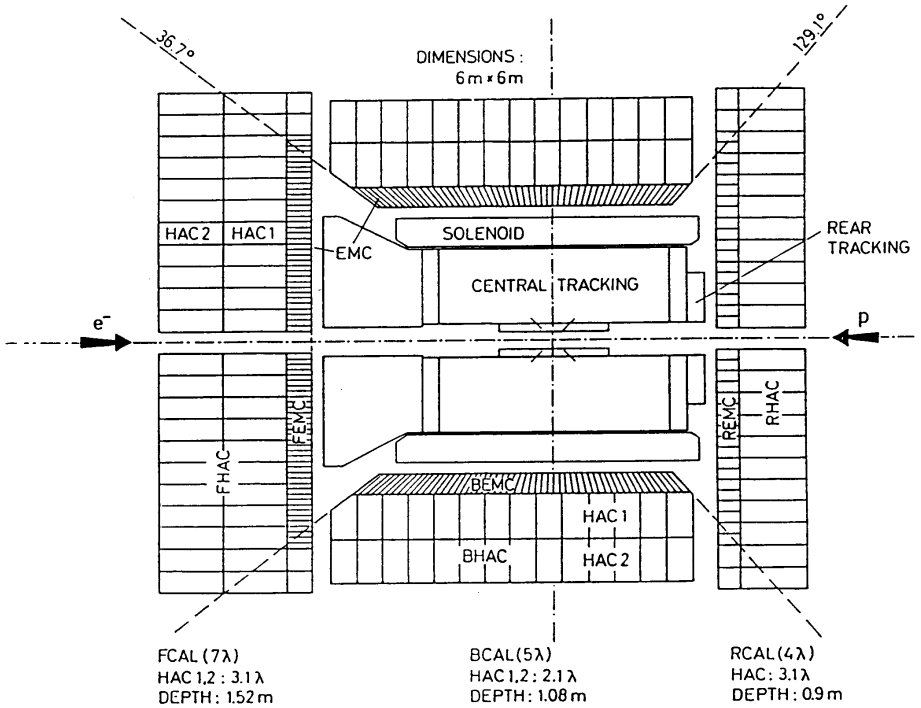

Figure 2.8: *Cross sectional view of the ZEUS calorimeter along the beam direction.*

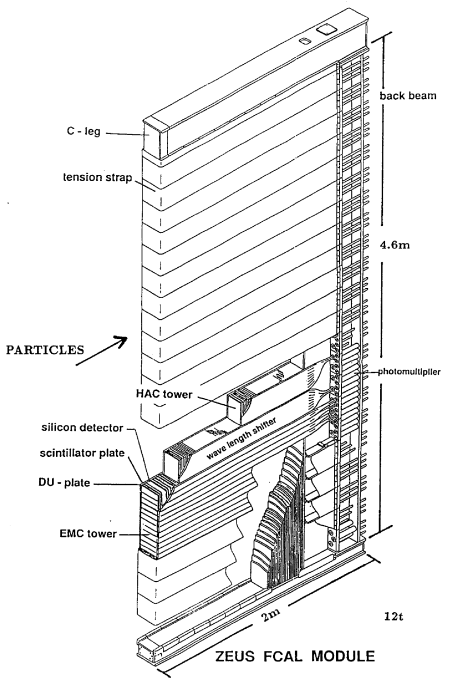

Figure 2.9: *Internal structure of a FCAL module.*

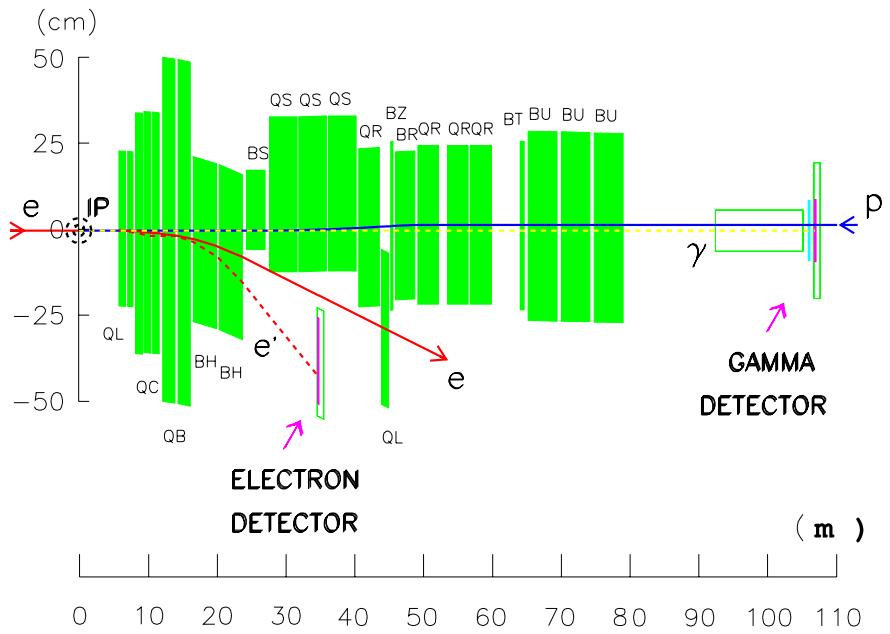

Figure 2.10: *Schematic view of the backward ZEUS elements, with the electron and photon calorimeters.*

The large forward-backward asimmetry of the ep final state due to the different energies of the incoming electron and proton is reflected in the forward-backward asymmetry of the calorimeter. The FCAL has a depth of 7 absorption lengths λ, while for the RCAL 4λ are sufficient.

2.2.3 The Luminosity Monitor

At HERA, the ep luminosity is measured using the rate of hard bremsstralhung photons from the Bethe-Heitler process $ep \to ep\gamma$, having this process a high cross section. The luminosity monitor (LUMI) consist of two calorimeters, an electron calorimeter (LUMI-e) and a photon calorimeter (LUMI-γ), as reported in fig 2.10. The LUMI-e is a lead-scintillator calorimeter located at $z = -35$ m. It measures small angle ($\theta < 4$ mrad) scattered electrons, which are deflected from the nominal orbit by the HERA magnets, whose energy is in the range of $(0.2 - 0.8) \cdot E_{beam}$. the LUMI-$\gamma$ is a lead-scintillator calorimeter as well, located at $z = -104$ m in the HERA tunnel. A $3.5X_0$ carbon/lead filter protects LUMI-γ against synchrotron radiation.

In the LUMI the total $e\gamma$ coincidence event rate R_{tot} is measured. Since only a fraction of $e\gamma$ events is produced in ep collision, the rate R_{ep} is determined subtracting to the total rate R_{tot} the pilot bunches rate weighted the ratio of the corresponding beam currents:

$$R_{ep} = R_{tot} - \frac{I_{tot}}{I_{pilot}} R_{pilot}. \tag{2.5}$$

The luminosity is then expressed as:

$$\mathcal{L} = \frac{R_{ep}}{\sigma_{obs}}, \qquad \sigma_{obs} = \int A_{LUMI} d\sigma_{BH}, \tag{2.6}$$

where σ_{BH} is the theoretical cross section for Bethe-Heitler process and A_{LUMI} is the acceptance of the LUMI monitor. The error on the luminosity results to be $\delta\mathcal{L}/\mathcal{L} \approx 2\%$.

2.2.4 The Forward Neutron Calorimeter

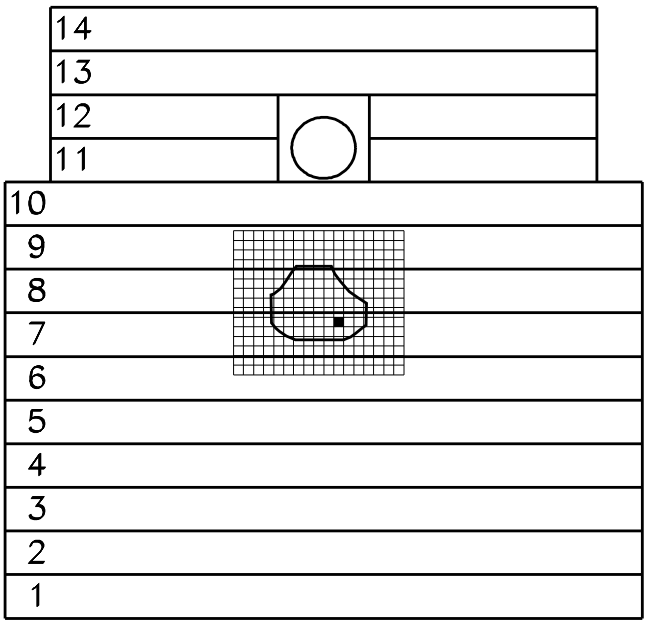

Figure 2.11: *Schematic picture of the Forward Neutron Detector.*

The FNC (figure 2.11) is a finely segmented compensating, sampling calorimeter with 134 layers of 1.25 cm-thick lead plates as absorber and 0.26 cm-thick scintillator plates as the active material. The scintillator is read out on each side with wavelength-shifting light guides coupled to photomultiplier tubes. It is segmented longitudinally into a front section, seven interaction lengths deep, and a rear section, three interaction lengths deep. The front section is divided vertically in 14 towers, each 5 cm high. The relative energy resolution for hadrons, as measured in a test beam, was $\sigma/E = 0.65/\sqrt{E}$. The FNC completely surrounds the proton beam, which passes through a 10×10 cm^2 hole in towers 11 and 12. Three planes of scintillation counters,

each $70 \times 50 \times 2$ cm^3, are located 70, 78 and 199 cm in front of the calorimeter. These counters completely cover the bottom front face of the calorimeter and are used to identify charged particles and so reject neutrons that interact in front of the FNC in inactive material such as magnets support structures, the beam-pipe wall and the mechanics and supports of the LPS.

2.2.5 The ZEUS Trigger and Data Acquisition System

The short bunch crossing time in HERA of 96 ns, with corresponds to a rate of about 10 MHz, requires an advanced trigger and data acquisition system. Out of a total interaction rate of about 10-100 kHz, which is dominated by interactions of the proton with residual beam-gas, the true *ep* interaction rate is only a few 10 Hz. Other sources for background are electron beam-gas interactions and cosmic rays events. The ZEUS three level trigger system, that is sketched in figure 2.12, selects physics events efficiently and reduces the total rate of accepted events to a few Hz, which can then be handled by the data acquisition system.

Each detector component has its own First Level Trigger (FLT), which is implemented as a hardware trigger and it is designed to reduce the event rate to below 1 kHz. The data are stored in a pipeline and the FLT makes its decision within 2 μs after the bunch crossing. The information is then passed to the Global First Level trigger (GFLT), which issues a global decision based on logical combinations of the component's trigger input. The decision by the GFLT of whether an event is accepted or rejected is returned to the component within 4.4 μs. The GFLT is designed to reduce the trigger rate below 1 kHz.

If an event is accepted by the GFLT, the data are transferred to the Second Level Trigger (SLT). The SLT is designed to reduce the input rate below 100 Hz. Each component has its own SLT,which is software based and runs on a network of transputers. The decisions of the local SLTs are then passed to the Global Second Level Trigger (GSLT), and are combined to issue a final decision.

If an event is accepted by the GSLT, the data from each component are sent to the Event Builder, which produces an event structure to combine all data in one data set. The data from Event Builder are then accessible to the Third Level Trigger (TLT) software that runs on a dedicated computer farm. The TLT finally reduces the input rate to a few Hz of *ep* physics events. Events which are accepted by the TLT are finally written to tape and the data files according to the ADAMO file management system [35].

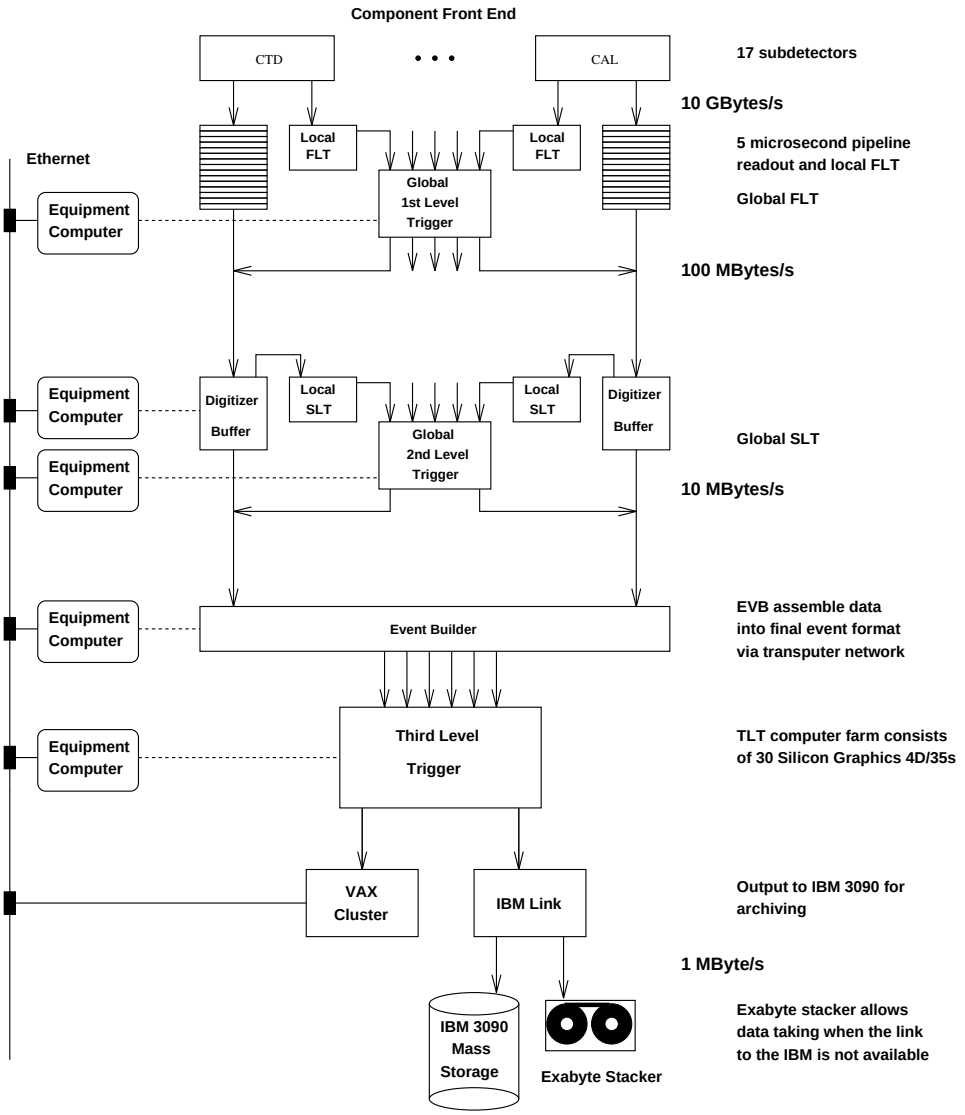

Figure 2.12: *Schematic diagram of the ZEUS trigger and data acquisition system.*

Chapter 3

The Leading Proton Spectrometer

The Leading Proton Spectrometer (LPS) is a single arm spectrometer positioned along the outgoing proton beam between z=20 m and z=90 m. It is designed to detect protons, which would otherwise escape though the beam-pipe. To achieve this task, a spectrometer consisting of 6 stations of silicon-microstrip detectors was placed in the proton beam line using beam optic magnets for particle deflection.

Since the accessible phase-space was squeezed between the 10σ profile of the beam and the vacuum chamber limits, lots of efforts were devoted in optimizing the number and the position of the detector stations within the constraints of finance and practicability so as to piece together a reasonable acceptance. The detectors had to be large in size and shaped to fit closely the elliptically-shaped beam. Custom front-end electronics had to be developed to work as close as 9 cm from 1 MJ of stored proton beam energy, pipelining and buffering data 90 m away from the acquisition system. A mechanical system capable of retracting detectors and pots during the beam fills and automatically reinstalling them with good position accuracy during beam collisions had to be designed, together with a fast extraction safety system to avoid detector damage. Finally, an alignment, calibration and reconstruction method had also to be developed.

The LPS was operating continuously up to the end of year 2000, when the HERA straight section had to be rebuilt to increase the specific luminosity.

3.1 Beam optics

Figure 3.1 is a simplified layout of the proton beam optics of the old[1] HERA straight section showing the optical function of the beam elements

[1] In year 2001 the straight section of HERA was redesigned to achieve an increased specific luminosity.

and the position of the six detector stations. The beam-line starts with a set of weak quadrupole magnets which focus the electron beam. Their effect on the proton beam is reduced by the ratio of the beam energies $E_e/E_p = 27.5/820 \sim 0.03$ but must be taken into account. Then follow two horizontal bending magnets which sweep the electron beam away from the proton beam. When protons arrive at the first station s1, the net effect is just a deflection of ~ 2 mm, whose direction depends on whether positrons or electrons are stored in the collider.

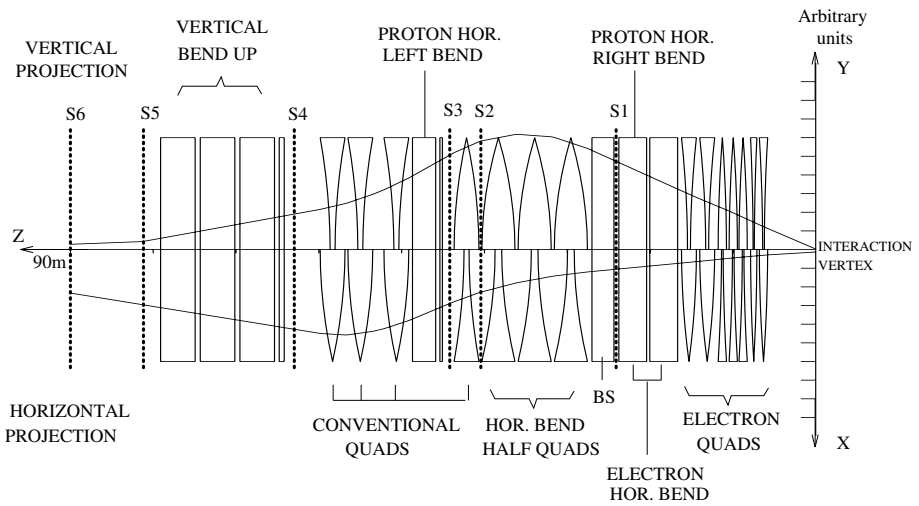

Figure 3.1: *Layout of the proton beam optics from the interaction vertex down to 90 m in the proton direction. The optical function of each beam element is shown. The curves represent the vertical (above) and horizontal (below) projection of the beam envelope. The position of the six detector stations is also shown as a dashed line.*

Immediately after s1, a septum magnet BS deflects the proton beam horizontally toward the outside of the ring and the deflection is further increased by the three magnetic half-quadrupoles which follow. Here is placed station s2 and, after the next conventional quadrupole, station s3. Here also ends the horizontally-bending section of the spectrometer, where the beam has been deflected horizontally by a distance of 15.8 mm.

Following s3 there is a horizontal bending magnet which brings back the proton beam parallel to its initial direction. A further three conventional quadrupoles completes the focusing system of the straight section. Finally comes the vertically-bending section of the spectrometer composed by stations s4 to s6 with three bending magnets in between and a total of 5.8 mrad bending angle.

Not shown in the figure are the horizontal and vertical orbit correction coils which were manually steered to optimize the luminosity in each fill; as their effect on the proton beam was not negligible, their current intensities

were added to the LPS data stream for offline correction. Also, beam position monitors were installed close to stations s3 and s4 which were used by the LPS safety system to detect beam instabilities.

Figure 3.1 also shows the 10σ envelope of the beam in the horizontal and vertical plane. The detector shapes were matched to these profiles and therefore varied between different stations. The intrinsic transverse momentum spread of the proton beam at the interaction vertex had a rms of about 50 MeV horizontally and 100 MeV vertically.

3.2 Spectrometer layout and construction

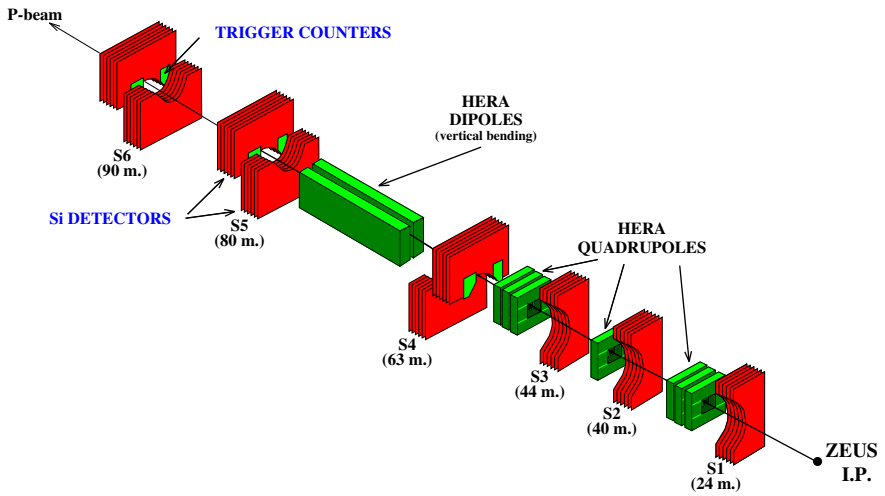

Figure 3.2: *Artistic view of the Leading Proton Spectrometer from the ZEUS interaction point (I.P.) up to the last detector station. The drawings of the detectors are not to scale.*

The layout of the LPS is schematically drawn in figure 3.2; it consists of six detector stations (s1 to s6) displaced along the beam line in the direction of the outgoing protons at the distances (measured from the interaction vertex) shown in the figure.
Each of the stations s1, s2 and s3 is equipped with an assembly of six planes of silicon microstrip detectors parallels to each other and mounted on a mobile arm which allow them to be positioned near to the proton beam by moving horizontally, from the outside of the HERA ring toward the ring center. The detector planes are inserted in the HERA beam-pipe by means of re-entrant Roman pots, stainless steel cylinders with an open end away from the beam and the other end closed. The silicon detectors are inserted from the open end and are moved until they are at about 0.5 mm from the closed end. The whole pot can be then inserted transversely into the beam-

pipe.
Stations s4, s5 and s6 each consist of two halves, each half containing an assembly of six planes similar to those of s1,s2 and s3. They are also mounted on mobile arms which can be moved and independently approach the beam from above and from below. In the operating position the upper and the lower halves partially overlap (cf. figure 3.5a). The offset along the beam direction between the upper and the lower pots is approximately 10 cm. The upper halves contain additional planes used for the trigger system.

In total, the LPS features 60 silicon planes and about 54000 readout channels.

3.2.1 Detectors and Front-end

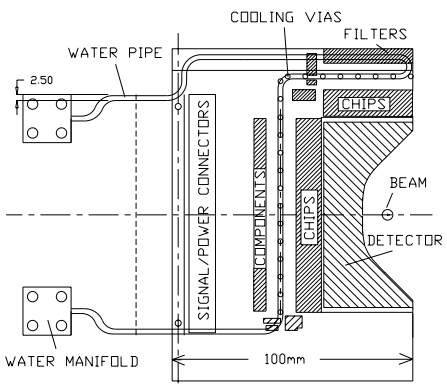

Figure 3.3: *Plan view of a detector plane mounted on the support board with indications of the chip, component layout and the cooling system.*

The basic front-end element is shown in figure 3.3. It consists of a shaped detector plane with up to 1024 strips mounted on a Cu-Invar multilayer printed circuit board which matches the coefficient of thermal expansion of the silicon. This board also carries the front-end readout chips and features thin layers of copper for thermal conduction and cooling vias which provide metal conducting paths from the metal planes to the exterior. Water cooled pipes of 1 mm^2 are also shown which are mounted in thermal contact with these vias.
In each pot, six of these units are closely packed together, mounted with their normal parallel to the beam. Detector strips are oriented at 0° and ±45° relative to the pot axis, two planes for each orientation, to provide redundancy and to remove reconstruction ambiguities. An additional unit is added in some pots with smaller planes used for the trigger system. A picture of the assembly mounted on the support is shown in figure 3.4. The distance between neighbouring planes is approximately 7 mm, therefore the overall thickness of the assembly is only about 5 cm. The detector planes

Figure 3.4: *Detector assmbly mounted on the support as seen from two opposite sides (only four planes out of six were installed for this picture). The small trigger planes are clearly visible in the picture on the right.*

are mounted in each assembly with a precision of about 30 μm. In the final arrangement, the detector packet is enclosed in a box which fits the shape of the detectors and provides both mechanical and electromagnetic protection; it is made of a thin copper layer enclosed in epoxy with a total thickness of 300 μm.

The detectors planes are 300 μm thick single-sided microstrip planes with up to 1024 p+ strips implanted on the n+ silicon substrate. The interstrip distance is 115 μm for the detectors with strips oriented at 0° and $115/\sqrt{2} = 81$ μm for the detectors with strips at $\pm 45°$. Typical depletion voltages range between 35 and 50 V; at these voltages, the strip capacity is about 1.2 pF/cm with a leakage current of few nA[2]. The size of the detectors vary between different stations but is approximately 6×4 cm^2. The precision of the elliptical shaped cut, which also vary from station to station, was measured to be of the order of 100 μm. In data taking conditions the distance of each detector plane from the beam center ranges between 3 and 20 mm depending on the station.

The frontend readout electronics [36] was designed based on a set of specifications derived from the HERA environment and from the pipelined readout architecture of the ZEUS experiment. In particular, radiation hardness to high energy protons and neutrons, low noise and low power consumption were required. The ability to sustain large input currents from the DC coupled silicon detectors without large loss of gain was also crucial in the design. As a result, a mixed technology combination is used: a bipolar amplifier-comparator VLSI chip (TEKZ) followed by a CMOS digital pipeline and multiplexer chip (DTSC), with each chip serving 64 strips.

[2]Some of the detector planes showed ageing effects leading to hundreds of nA of leakage current after six years of operations.

The system is binary, i.e. a bit is stored for every channel in the time slice corresponding to a bunch crossing, which is set if the pulse height exceeds a threshold, and is zero otherwise. No other information is kept.
The TEKZ chip [37] integrates a preamplifier followed by a comparator with a common programmable threshold. The shaping time is τ_s=32 ns and the overall gain is about 150 mV/fC. The amplifier noise scales linearly with the load capacitance C and was measured to be $\sigma_n = 690 + 40C$ [e$^-$]; even for the longest strip, the ratio signal over noise is over 20. The chip also features four calibration lines, each connected to the calibration capacitors of 16 channels, allowing to inject a known charge in each channel. The power consumption is about 2 mW/channel.
The task of the Digital Time Slice Chip (DTSC) [38] is to buffer the digital data until a trigger decision is made and to multiplex the data out serially on four data lines. It features a level-1 digital pipeline, 64 cells wide, which operates sincronous with the 10.4 MHz collision frequency and stores the data long enough to allow for the 5 μs latency of the ZEUS level-1 trigger decision. A level-2 buffer is also available. The power consumption is also about 2 mW/channel.

3.2.2 LPS Trigger

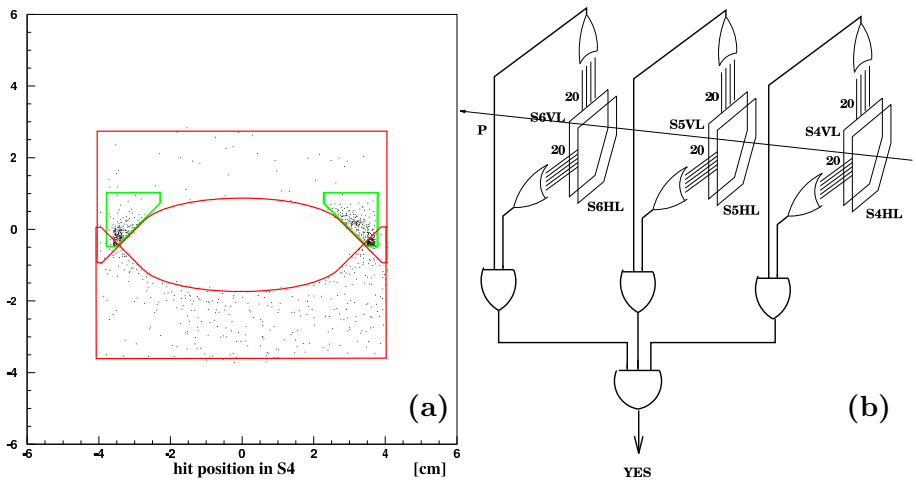

Figure 3.5: *(a) Hit positions in station s4: the outlines of the LPS detectors and of the two small trigger planes are shown. (b) Trigger logic implemented online; only left side is shown.*

A trigger system [39] was designed in stations s4-s6 to tag elastic and diffractive events where the scattered proton carry a fraction of the beam momentum x_L larger than 0.95. Because of the large vertical transverse momentum spread of the beam in the interaction region, these events cluster

in two opposite narrow regions in the left and right inner corners of the LPS detectors. To cover this area, μstrip silicon trigger planes were designed as small trapezoids (see figure 3.5a). Two planes are installed in each corner of the upper pots which overlap in position and have orthogonal strip orientation (0° and 90° relative to the pot axis). Each trigger plane is segmented into 20 strips with 750 μm strip pitch and is AC coupled to a TEKZ chip. The digitized data are sent in parallel 100 m away where the trigger logic is implemented in FPGA units. Here, a matrix trigger logic was designed where linear correlations can be required between hit positions to provide momentum selection. The simpler logic shown in figure 3.5b, corresponding to a coincidence of hits in all the three stations, has been used in the final implementation. The typical rate of triggers has been a few kHz at most, reducing to few Hz when some activity in the ZEUS central detector was required in conjunction.

3.2.3 Mechanical Construction

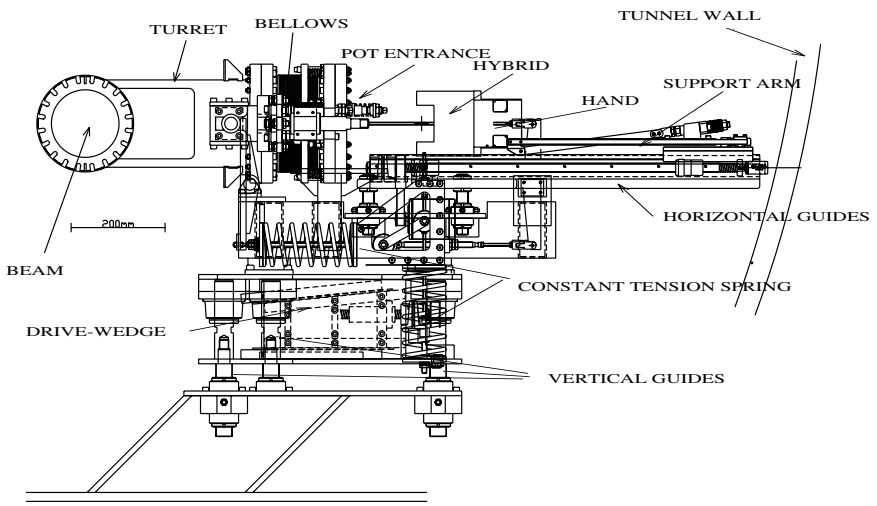

Figure 3.6: *Line drawing of the mechanical construction of a horizontally moving pot.*

Roman pots allow to operate the detectors at atmospheric pressure and to easily retract them in a safe position during machine fill or when beam instabilities occur. The pot lateral walls are 3 mm thick while, at its end nearest to the beam, the pots are only 0.4 mm thick and are shaped around the detector cutout so that the pot can fit snugly against the beam profile. Thin windows, 0.4 mm thick, are also let into the upstream and downstream sides of the pot to reduce multiple scattering.

Figure 3.6 is a labelled line-drawing of a horizontally mounted pot system. The detectors, support hand and arm are mounted on a small carriage

and move on the horizontal guide by a step-motor drive. The pot itself can be positioned nearer or further from the beam and has also limited lateral movement provided by a wedge and guide system; to ensure vacuum tightness and allow such movements, a bellow connects the pot to the vacuum pipe. The atmospheric force on the pot amounts to about 8 kN and is balanced by a constant tension spring system with two springs, a force summing system in a triangular frame and a system of levers to apply the force to the pot flange. The pot position is measured with resolvers mounted on the motor shaft with a nominal resolution of 5 μm .

Stations s5 and s6 somewhat differ in the design because they were inherited and modified from previous experiments at CERN [40]. In particular, to balance the atmospheric force, a pneumatic system with high pressure nitrogen is used. The pots are driven with DC motors and the pot positions are measured using linear transducers with a resolution of about 30 μm.

3.3 Detector operations and performance

The insertion of the pots and the detectors is a critical task which begins after the beams are brought in collision and stable conditions are observed. An automatic insertion program was developed. First, all the detectors are moved simultaneously into the pots. Later, one pot at a time is moved in steps of decreasing size (from 2 to 0.1 mm) into the operating position. Prior to the insertion, the program checks the proton beam positions measured by the HERA beam position monitors, the positions and rates of the HERA collimators, the rates of the trigger counters of the FNC [41] which is located 10 m downstream of s6. These quantities, together with the rates of the LPS trigger planes and of some additional scintillators positioned around the beam-pipe are also continuously monitored during the insertion. The insertion stops if any of these quantities exceeds a threshold and is recovered when the corresponding value decreases to a safe level. If several stops occur, the procedure is aborted and the pots are extracted. Otherwise, when all the pots are in the operating position, the procedure stops. During data acquisition, the proton beam positions and the LPS trigger rates are continuosly monitored and a hardware safety system triggers a fast extraction of the detectors if the rates are above a programmable threshold or if the beam drifts away from its nominal position.

About 25 minutes or more were necessary to insert the pots, depending on the beam conditions. This, and the fact that the beam conditions did not always allow a safe insertion of the detectors results in a reduced efficiency compared to other components of the ZEUS detector.
A total integrated luminosity of 72 pb^{-1} was collected by the LPS from 1994 to 2000, which should be compared to the 130 pb^{-1} collected by ZEUS in the same years. A breakdown is shown in table 3.3. The integrated luminosity

used in physics analyses (also shown in the table) was 14% lower because some HERA fills with very unstable beams, high background or bad detector conditions were excluded.

	Luminosity (pb^{-1})				Luminosity (pb^{-1})		
Year	ZEUS	LPS	LPS*	Year	ZEUS	LPS	LPS*
1994	3.0	0.9	0.9	1997	28	14	13
1995	6.6	3.5	3.4	1999	36	15	10
1996	11	4.0	0.0	2000	47	35	35
Total					132	72	62

Table 3.1: *Integrated luminosity collected by ZEUS and by the LPS. The column marked with an asterisk is the luminosity which is used in physics analyses.*

Note that the inefficiency caused by detector problems was negligible compared to that caused by bad beam condition and was mainly due to mechanical problems in the pot positionning system or dirt in the cooling water blocking the the small pipes of cooling system. Few planes showed occasionaly strong increase in leakage current or dead readout DTSCs and were replaced when possible during the machine shutdowns which occured once per year. Fortunately, the system was designed with sufficient redundancy that the loss of one or even two planes in a pot without immediate replacement can be tolerated. Excluding the malfunctioning planes, the noisy or malfunctionning channels were always less than 2% and were masked in the readout. The efficiency for the remaining channels was measured to be better than 99.5% in each plane. An average noise of less than 0.3 channels firing in each plane in a time slice corresponding to a bunch crossing was measured under data taking conditions by examining collisions of empty electron and proton bunches.

3.4 Reconstruction and alignment of the detector

3.4.1 How the Proton Momentum can be Measured

Figure 3.7 shows a simplified layout of the LPS beam optics. The LPS can be considered as a pair of two independent spectrometers with almost no acceptance overlap: s123 and s456, formed by the group of stations s1-s2-s3 and mboxs4-s5-s6, respectively. As shown in the figure, they exploit the horizontal and vertical bending sections of the beam line.
In the simplest case of a track being recorded in the three stations s4-s5 and s6 (see figure 3.7), the track projection on the horizontal plane is a straight line while the track deflection d_v in the vertical bending magnets between

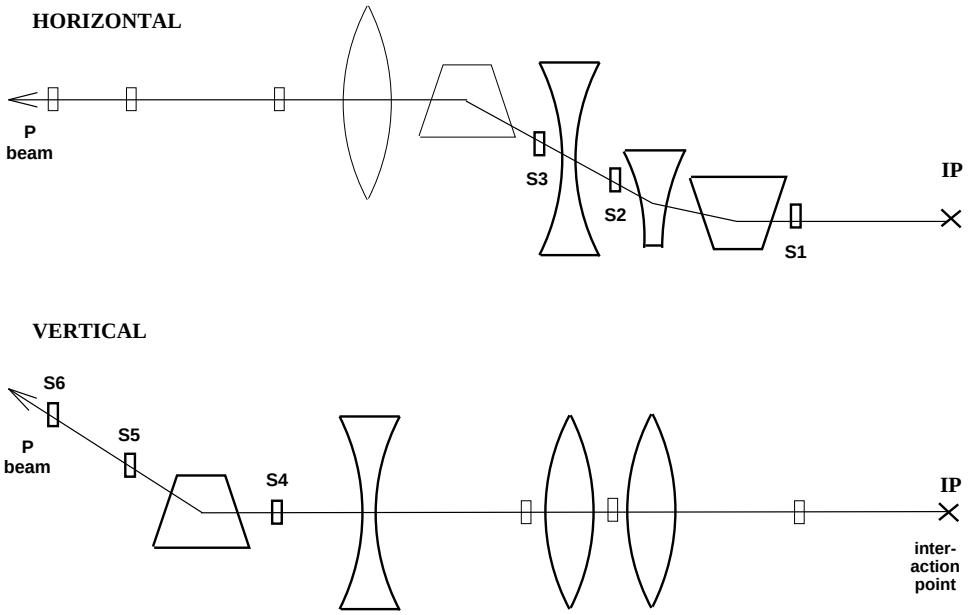

Figure 3.7: *Simplified LPS beam optics, where the beam elements have been grouped together to show the main optical function.*

s4 and s5 gives a direct momentum measurement, $p = const./d_v$. Tracks detected in these three stations can be extrapolated backwards to $z = 0$[3] to also measure the transverse position of the interaction vertex.

However, a method was developed for the case when only two stations are hit as a key to build up a viable acceptance; in this case, the interaction vertex position is used as a third point to measure the trajectory.
In a given projection, e.g. horizontal, the beam optics is described by a linear beam transport equation which relates the position h_k and the angle $h'_k = dh/dl$ of the track at each station to the position x_v and angle $x'_v = dx/dl$ of the track at the interaction vertex. Here l represents the coordinate along the nominal beam trajectory, while the positions and angles h and h' are relative to the nominal beam position and direction at that value of l (the nominal beam crosses the interaction vertex $z = 0$ at $x = y = 0$). One has:

$$\begin{bmatrix} h_k \\ h'_k \end{bmatrix}_{z=z_k} = \begin{bmatrix} T^k_{11}(x_L) & T^k_{12}(x_L) \\ T^k_{21}(x_L) & T^k_{22}(x_L) \end{bmatrix} \begin{bmatrix} x_v \\ x'_v \end{bmatrix}_{z=0} + \begin{bmatrix} B^k_1(x_L) \\ B^k_2(x_L) \end{bmatrix} \qquad (3.1)$$

An independent equation of the same form can be written for the vertical direction v. The transport matrix elements T^k are known functions of x_L which describe the effects of the beam quadrupoles and drift lengths. The

[3]The coordinate system used in ZEUS has the z axis pointing in the proton beam direction, hereafter referred to as "forward", the x axis pointing horizontally toward the centre of HERA and the y axis pointing upwards. The polar angle θ is defined with respect to the z direction.

vector elements B^k, also functions of x_L, describe the deflection induced by the beam dipoles and by the quadrupoles in which the beam is off axis; since the beam is taken as reference, they vanish as $x_L \to 1$.
Equation 3.1 and the corresponding one for the vertical direction can be written for a pair of stations (a,b); upon eliminating the unknowns x'_v and y'_v, one finds

$$\begin{array}{rcl} h_b & = & m_h^{ab}(x_L)h_a \;+\; c_h^{ab}(x_L, x_v) \\ v_b & = & m_v^{ab}(x_L)v_a \;+\; c_v^{ab}(x_L, y_v) \end{array} \tag{3.2}$$

where m^{ab} and c^{ab} are known functions of the matrix elements T^k and B^k. Equations 3.2 are independent, apart from the common dependence on x_L. If drawn in the coordinates (h_a,h_b) and (v_a,v_b), they represent a set of lines with slope and intercept being function of x_L. An example is shown in figure 3.8. For any pair of hits in stations a and b, two independent estimates of x_L can be obtained by determining on which of these lines the coordinates sit. Once x_L is determined, the equations 3.1 can be inverted to solve for x'_v and y'_v to give the transverse momentum.

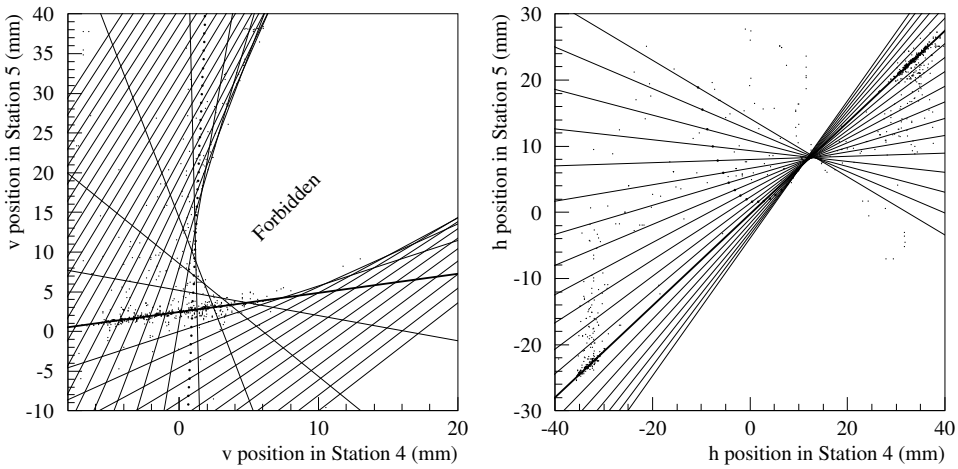

Figure 3.8: *Horizontal h and vertical v correlation between track positions in the two stations s4 and s5. Lines are for the correlations between the h and v coordinates measured in the two stations for tracks originating from the nominal interaction point. Each line corresponds to a fixed value of x_L, at intervals of fixed $1/x_L$, from 0.5 to 2. The thicker line is for $x_L = 1$ and the lines rotate clockwise as x_L decreases. The small dots are events and the large dots are the points on the fixed x_L lines where the transverse momentum p_x or p_y is zero. Diffractive physics shows up as the large fraction of events clustered around the $x_L = 1$ line.*

Note that, as shown in figure 3.8, there are regions where lines of different x_L cross. The corresponding x_L ambiguity is resolved by comparing the x_L solutions found in this projection with those found in the other projection.

Also, note that there are regions with no lines. Any pair of hits that reside in these forbidden regions cannot be caused by any track originating from the interaction point.

3.4.2 Track Reconstruction

To reconstruct tracks in the LPS, a pattern recognition is performed which is followed by a track fit [42, 43].

The task of the pattern recognition is to identify tracks in stages, starting with individual hits and gradually building to full tracks. Along the way, unlikely combinations of hits are eliminated. As several tracks can produce hits simulataneously in the detector, each track hitting up to 54 planes, this stage has to be carefully executed to avoid large combinatorial background or loss of track informations.

First, track segments are found independently in each detector assembly of six planes. Clusters of adjacent strips in each plane are matched between planes with the same strip orientation and combined with clusters (or matched clusters) belonging to the two other projections. In order to reduce the number of candidates, track segments that traverse the overlap region between the upper and lower halves of the stations are retained as a single candidate. All hits belonging to each candidate (up to twelve for tracks crossing the two halves, up to six otherwise) are used in a fit to find the transverse coordinates of the track at the z corresponding to the center of the station. Only the 10 best quality coordinates in each station are retained.

The next task is to combine from different stations pair of coordinates that belong to the same track. At initialization, the program calculates the transport matrices of equation 3.1 for each station at fixed values of x_L and stores the corresponding values in a lookup table. When comparing the h or v positions of two coordinates, the program builds the lines of equation 3.2 at intervals of x_L using the values stored in the lookup tables. The positions of the coordinates are then checked to see if they sit between two adjacent lines; if so, the distances to the two lines are used in a linear interpolation to determine the value of x_L. This process is illustrated in figure 3.9. In the regions of overlap (figure 3.9a) there may be more than one solution for x_L; only the value which is the closest to the solution found in the other projection is retained. The situation illustrated in figure 3.9b may instead occur if, for example, multiple scattering throws a track into the forbidden region; the x_L value of the closest line is chosen along with an appropriate error. Finally, the solutions found in the h and v projections are compared to make sure they are consistent within errors. If they are, the coordinate pair is saved as a two-station track candidate.

As a final step of the pattern recognition, three-station track candidates are built by merging those two-station candidates which share the same hit

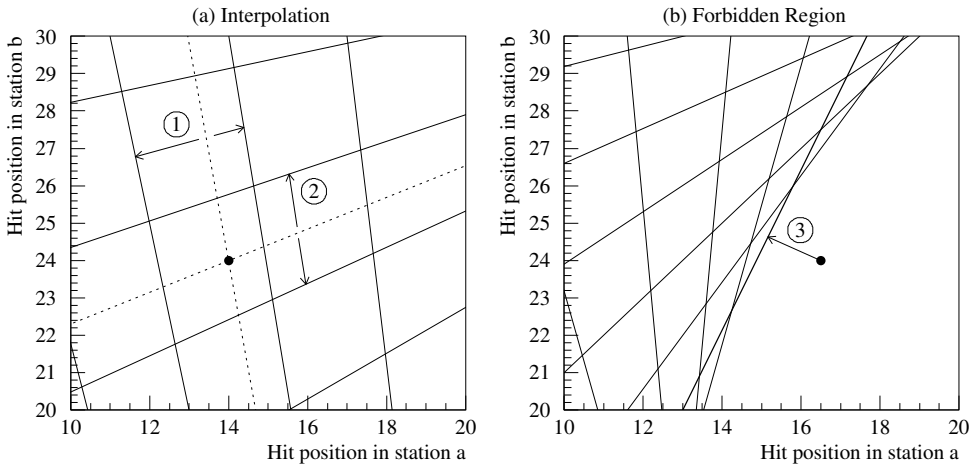

Figure 3.9: *Illustrating the two-station method of momentum reconstruction. The LPS reconstruction program generates a grid of lines of constant x_L from the lookup table. Most tracks (see large dot in* **(a)***) produce hits that fall between these lines. In this case, x_L solutions are obtained by interpolating between adjacent neighbouring lines as shown by ① and ②. For hits that fall in the forbidden region, the nearest line (dark line) is chosen as x_L solution ③.*

in the station in common and whose x_L value is compatible within errors. Two-station and three-station candidates are then passed to a conventional track-fitting stage.

The track χ^2 is defined as

$$\chi^2 = \left[\sum_i \frac{[s_i - S_i(x_v, y_v, x'_v, y'_v, x_L)]^2}{\sigma_i^2}\right] + \frac{(x_v - x_0)^2}{\sigma_x^2} + \frac{(y_v - y_0)^2}{\sigma_y^2}, \quad (3.3)$$

where the sum runs over all clusters in all planes assigned to a track. Here s_i is the cluster position, σ_i the uncertainty associated to it (which includes the effects of multiple scattering and the contribution of the cluster width; typical values range from 50 to 100 μm), (x_0, y_0) are the nominal interaction vertex coordinates and σ_x and σ_y the nominal widths of the vertex distribution. S_i, a function of the five track parameters $(x_v, y_v, x'_v, y'_v, x_L)$, is the predicted cluster position calculated from equation 3.1 and the corresponding one for the vertical direction. The last two terms in equation 3.3 constrain the track to the interaction vertex. This expression, for simplicity, assumes that the cluster errors are uncorrelated, which is not true because of the contribution of the multiple scattering. The effect of this approximation is expected to be small.

This χ^2 is minimised with respect to the five track parameters, and the best track parameters, together with the error matrix, are determined. In addi-

tion to the χ^2 value, other quantities are assigned to each track candidate which allow to reject unphysical tracks. In particular, the miss probability $P_m = \prod(1 - \varepsilon_i)$, where the product extends over the planes missing a hit and where ε_i is the plane efficiency, is expected to approach the unity for true tracks. Also, a detailed simulation of the shape of the beam elements allows to propagate the track through the beam-pipe and calculate the distance of closest approach to it; this quantity is required to be positive for all candidates.

3.4.3 Alignment and Calibration

The alignment is one of the most important and difficult problems. The parameters which affect the reconstruction are the magnetic fields of 23 beam elements (known with good accuracy), the positions of the quadrupole axes (known with less accuracy by the HERA survey), the positions of the LPS detectors and the position and tilt of the proton beam at the interaction vertex (all to be determined). In addition, the positions of the beam apertures are crucial in determining the acceptance of the detector. Furthermore, the spectrometer has some instabilities which are not under user control; these include vertex position and beam tilt in the interaction vertex, slow movements of the tunnel structure or even mechanical miscalibrations of the stations themselves. Fortunately, diffractive events provide a bright calibration line at $x_L = 1$. As an example, in elastic ρ^0 photoproduction $x_L \simeq 1 - (M_\rho^2 + |t|)/W^2$ where M_ρ is the ρ^0 meson mass and W is the photon-proton centre-of-mass energy; in these events the value of x_L at HERA differs from unity on average by 10^{-4}.

The detailed description of the alignment procedure can be found in ref. [43, 44]; here we will briefly focus on the main issues.
The relative position of stations s4, s5 and s6 can be determined with a precision of few μm by using a sample of diffractive events (e.g. elastic ρ^0's) because the h and v projection of the $x_L = 1$ tracks are straight lines in the bending field between s4 and s5. Once these three stations are aligned relative to each other, the momentum of any three-station track can be determined by measuring the track deflection as discussed in page 52. A global fitting procedure was set in which the position of the three stations, considered as a rigid body was adjusted so that all three-station tracks of all momenta were seen to originate from a common minimized vertex volume. Care is taken in this stage to reject beam-halo tracks which do not originate from the interaction vertex. Typical accuracy of this method is better than 20 μm. Adjustments to the position and the strengh of a quadrupole were also determined with this fit.
The next step is to determine where the beam lies in this reference frame as a key to measure the transverse momentum of the tracks relative to it. The procedure which follows was repeated for each fill of the machine. First,

three-station tracks are fitted using equation 3.3 without constraining to the vertex and the average vertex position is determined. Then, the beam tilt at the interaction vertex is determined to within a few MeV by using diffractively photoproduced ρ^0 mesons ($\gamma p \to \rho^0 p$) and by requiring that the transverse momentum of the ρ^0, as measured in the central tracking chamber of ZEUS, is opposite to the transverse momentum of the scattered proton measured in the spectrometer.
Finally, the position of the limiting beam apertures is cross-checked with a precision of 0.2 mm by propagating a large sample of well reconstructed tracks at the location of the main obstructions.

Chapter 4

The event simulation

In high-energy physics Monte Carlo (MC) simulation techniques play a crucial role. In fact it is not possible to have a complete analitical description of the physics processes and detector response.

The Monte Carlo simulation is widely used to compare experimental data with theoretical predictions, and in particular to determine the resolutions of the measured quantities, to understand the acceptance of the detectors and trigger systems, to test the physics models, to extract detector independent results and to evaluate the systematics uncertainties.

The Monte Carlo simulation for high-energy physics experiments consists of two main parts: first, the fundamental interaction is simulated with a MC "generator" describing the cross section dependence on the event kinematics and the hadronic final state topology. After that, the response of the experiment (detector plus trigger) to the final state particles is simulated (detector simulation). The degree of agreement between the simulation and the real data depends on how well we understand the physical process we are considering as well as the behaviour of the experimental apparatus.

4.1 Monte Carlo generators

4.1.1 Simulation of the standard Deep Inelastic Scattering

As mentioned in section 1.3, the inclusive cross section for ep deep inelastic scattering is given in terms of proton structure functions (eq. 1.9):

$$\frac{d\sigma(e^{\pm}p \to e^{\pm}X)}{dxdQ^2} = \frac{4\pi\alpha^2}{xQ^4}\left[\left(1 - y + \frac{y^2}{2}\right)F_2(x,Q^2) - \Delta_L \pm \Delta_3\right].$$

The distributions of the events in the kinematic phase space is determined by the dependence of the structure functions on the kinematic variables. The structure functions are chosen in the PDFLIB library [45], which

contains several sets of parton densities functions obtained by the fit of real data.

In addition to the cross section of Eq. 1.9, higher order contributions have to be taken into account. These corrections originate from QED and QCD radiation. Indeed a real or virtual photon can be emitted from the electrically charged lines, as well as gluons can be radiated from the interacting partons of the proton. These contributions change the observed cross section and can also affect the measurement of the kinematic variables. In this analysis the radiative QED corrections (real as well as virtual) are simulated by the HERACLES MC generator [46], and the QCD radiation is simulated using the LEPTO MC generator [47]. The two generators are interfaced via the program DJANGOH [48].

Experimentally only hadrons can be observed in the detector, and not the single partons. Since the strong coupling constant α_s becomes large at scales comparable with the hadron masses and perturbation theory is not applicable anymore, the hadronization of the partons needs to be described by phenomenological procedures. In LEPTO the QCD radiation is performed using the Matrix Elements plus Parton Shower (MEPS) model: the matrix elements of the hard subprocess are calculated at leading order in α_s. Higher orders are approximated by the emission of partons in the initial and final states, based on the DGLAP evolution equations (equations 1.14 and 1.15). After the Parton Shower the hadronization is performed with the LUND string fragmentation [33] using the JETSET package [49]: the partons are connected by colour strings and, as they move away from each other, these colour strings stretch and fragment into smaller pieces. If these pieces have not enough energy left to break further, hadrons are formed in the final state.

An alternative model to MEPS is the Colour Dipole Model (CDM), implemented in the ARIADNE package [50]. This model assumes that a colour dipole is created between the scattered quark and the proton remnant. The colour dipole then emits gluons which in turn form new dipoles with neighbouring partons. The parton cascade stops when no more energy is available and hadrons are then produced according to the LUND fragmentation.

4.1.2 Rapidity gaps and Soft Colour Interaction

The Soft Colour Interaction model (SCI) gives rise to rapidity-gap events and it can simulate the diffractive scattering without using the concept of Pomeron.

At small Bjorken-x, where the rapidity gaps occur, the events are frequently initiated by a gluon from the proton. This can either be directly from the boson-gluon fusion matrix element or after the initial state parton shower, including a possible split in the sea quark treatment. In the conventional string hadronization model this gives two separate strings from the q

and $\bar{q}$ to the proton remnant spectator partons. The gluons from the parton shower are represented as kinks on the string, thereby causing particle production over the whole rapidity region in between. The idea of SCI is that at this point additional non-perturbative soft colour interactions may occur. These have small momentum transfers, below the scale Q_0^2 defining the limit of pQCD. The SCI will change the colour of the involved partons and thereby change the colour topology as represented by the string, without significantly change the partons momenta.

All partons from the hard interaction plus the remaining quarks in the proton remnant constitute a set of colour charges. Each pair of charges can make a soft interaction changing only the colour and not the momenta, which may be viewed as soft non-perturbative gluon exchange. As the process is non-perturbative the exchange probability cannot be calculated and is described by a parameter connected to the probability that a SCI may occurr. The number of soft exchanges will vary event-by-event and causes a change of the colour topology of the event such that, in some cases, colour singlet subsystems arise separated in rapidity. In the LUND model this corresponds to a modified string stretching and rapidity gaps may arise when a gap at the parton level is not spanned by a string. In particular, when the hard process starts with a gluon from the proton, leaving a colour octet remnant and giving a colour octet hard scattering system, a soft colour exchange between the two octet systems can give rise to two colours singlets separated in rapidity.

4.2 The detector simulation

The events generated with the Monte Carlo Generators are passed through the ZEUS detector and trigger simulation, off-line reconstruction, and the physics analysis chain. The two last steps are exactly as applied to the real data.

The ZEUS detector simulation is based on the GEANT package [51], taking into account the geometry, position and material of various detector components and incorporates the present understanding of the detector from test beam results and physics analyses. Hadronic and electromagnetic particles are tracked through the detector volumes simulating the response of the detector materials to electromagnetic and hadronic interactions. The trigger decision, which is based on the detector component signals, is simulated with the trigger software package Zeus Geant Analysis (ZGANA [52]). The detector simulation together with the trigger software package is called Monte Carlo for Zeus Analysis, Reconstruction and Trigger (MOZART).

All these detector simulation programs run on FUNNEL, a Monte Carlo production facility that works on a large amount of machines distributed all over the world.

The input to the ZEUS detector simulation is a list of particles which includes their type, momentum four-vector, and production vertex from the *ep* event generator. The simulated detector response of the various components is stored in the same data structures (ADAMO tables) as real data and can be then processed with the same reconstruction and analysis code. In addition, the true MC event information is available.

4.2.1 MOLPS: the LPS standalone simulation

The simulation of the Leading Proton Spectrometer is performed by the MOLPS package. It is based on the MOZART LPS routines [53, 54], but it runs within the physics analysis program. The advantage of the method is that new calibration constants and geometrical positions for the LPS can be easily implemented and the LPS simulation can be repeated without the need of redoing the full simulation of the events.

Also the LPS simulation is based on the GEANT software to model the response, acceptance and efficiency of the detector. In the simulation not only the detector volumes of the silicon planes need to be included, but also the 90 m of the HERA beam line with its magnets, collimators and drift zones as well as the beam itself.

LPS detector: Since the LPS detector uses a digital readout system, a LPS channel responds if it is hit by a charged particle. On top of this simple procedure, inefficiencies, noise and dead channels need to be included. Inefficiencies in the planes were determined from physics data and randomly applied to each LPS detector plane. The noise is simulated assuming 0.2 hits per event per plane and is randomly generated following a Poisson distribution. These noise hits are randomly positioned on the detector and added to the simulated raw data. Dead and noisy channels are suppressed at the reconstruction level using dead and noisy channel lists in the Monte Carlo database, which were determined from the LPS data quality monitoring during the data taking period.

HERA magnets and apertures: Since the beam-pipe apertures have a strong influence on the acceptance of the LPS detectors, the exact shape of the beam-pipe is included in the LPS simulation, whenever possible. The position of these apertures can be checked using reconstructed tracks during the alignement procedure. If they are found to be inconsistent with the pot positions and the track fitting, they can be relocated. The accurate position and field strength of the dipole and quadrupole magnets inside the beam-pipe necessary for the track reconstruction is simulated in GEANT. These parameters are also reviewed during the alignment procedure and can be adjusted accordingly.

Beam simulation: The beam parameters are essential for the accurate momentum reconstruction of the scattered proton: the vertex position is needed for the tracks of events recorded in only two stations, as they have to be constrained by the vertex position. The angle of the beam at the interaction point determines the measurement of the transverse momentum and, indeed, the beam emittance dominates the momentum resolution[1]. The beam tilt parameters are determined from the alignment procedure and can be set externally as input for MOLPS in the simulation. The vertex information is taken from MOZART. The values of these parameters for the beam simulation in 1997 are:

- vertex position: $x = -0.21$ mm and $y = -0.38$ cm;
- vertex Gaussian width: $\sigma_x = 0.33$ mm and $\sigma_y = 0.90$ mm;
- proton beam tilts: $p_x = 33$ MeV and $p_y = -68$ MeV;
- beam emittance of Gaussian width: $\sigma_{p_x} = 40$ MeV and $\sigma_{p_y} = 90$ MeV.

4.3 Summary of Monte Carlo samples used in the analysis

Since the Leading Proton Spectrometer has a very low acceptance (see section 6.2), it was necessary to generate a very high number of Monte Carlo events. The main sample consists of ten millions of DIS ($Q^2 > 2$ GeV^2) events generated with LEPTO-MEPS, taking into account the initial state radiation. The proton structure functions used in all MC samples are the CTEQ5N [55] . A smaller sample of events have been generated with LEPTO-ARIADNE, to study the effect of the Colour Dipole Model on the leading-proton production. In LEPTO the simulation of the leading-baryon kinematics is described in terms of proton remnant hadronization, as explained in section 1.6.3. The generated x_L and p_T^2 spectra of the leading-baryons are reported in figures 4.1 and 4.2 for LEPTO-MEPS and LEPTO-ARIADNE, respectively. In the figures, the leading-baryon is defined as the most forward baryon of the event, i.e. the one having higher x_L. For $x_L \gtrsim 0.97$ the leading-baryon is always a proton, because in this region the diffractive process dominates.

The motivations for which LEPTO-MEPS has been choosen as the main Monte Carlo generator in the analysis of the leading-proton production will be explained in section 5.3.

For the study of the migration from lower Q^2 region due to the finite resolution (see section 5.5), two further samples have been generated, using LEPTO-MEPS, with a generation cut on $0.5 < Q^2 < 2$ GeV^2, and

[1]The emittance is the measurement of the beam particles parallelism. The resolution will be explained in section 6.1.

Generator	Generated events (millions)	Luminosity pb^{-1}
LEPTO-MEPS (main sample)	10	18
LEPTO-MEPS (low Q^2)	17	18.9
PYTHIA	2.5	8.5
LEPTO-ARIADNE	1	1.8

Table 4.1: *Summary of Monte Carlo generators used for this analysis with the number of generated events and the MC luminosity.*

Generator	Generation cuts	Generation cuts efficiency
LEPTO-MEPS (main sample)	$Q^2 > 2$ GeV^2	100%
LEPTO-MEPS (low Q^2)	$0.5 < Q^2 < 2$ GeV^2 $x_L > 0.3$, $\theta_e < 3.105$ $y_{gen} > 0.02$	11%
PYTHIA	$x_L > 0.3$, $p_T^2 < 0.6$ GeV^2 $y_{gen} > 0.02$, $\theta_e < 0.0013$ $E - p_z > 35$ GeV	1.2 %
LEPTO-ARIADNE	$Q^2 > 2$ GeV^2	100%

Table 4.2: *Summary of Monte Carlo generators. The generation cuts have been applied to preselect the events before the detector simulation and analysis chain. The generation cut efficiency corresponds to the fraction of events that was submitted to the detector simulation.*

PYTHIA [56], for photoproduction events at $Q^2 \approx 0$ GeV^2. The two low-Q^2 samples were generated requiring a set of additional cuts on global DIS variables, as reported in table 4.2. The generation cuts were optimized to enhance the selection efficiency, that will discussed in section 5.1.

Tables 4.1 and 4.2 contain the generation parameters with which each Monte Carlo sample has been generated.

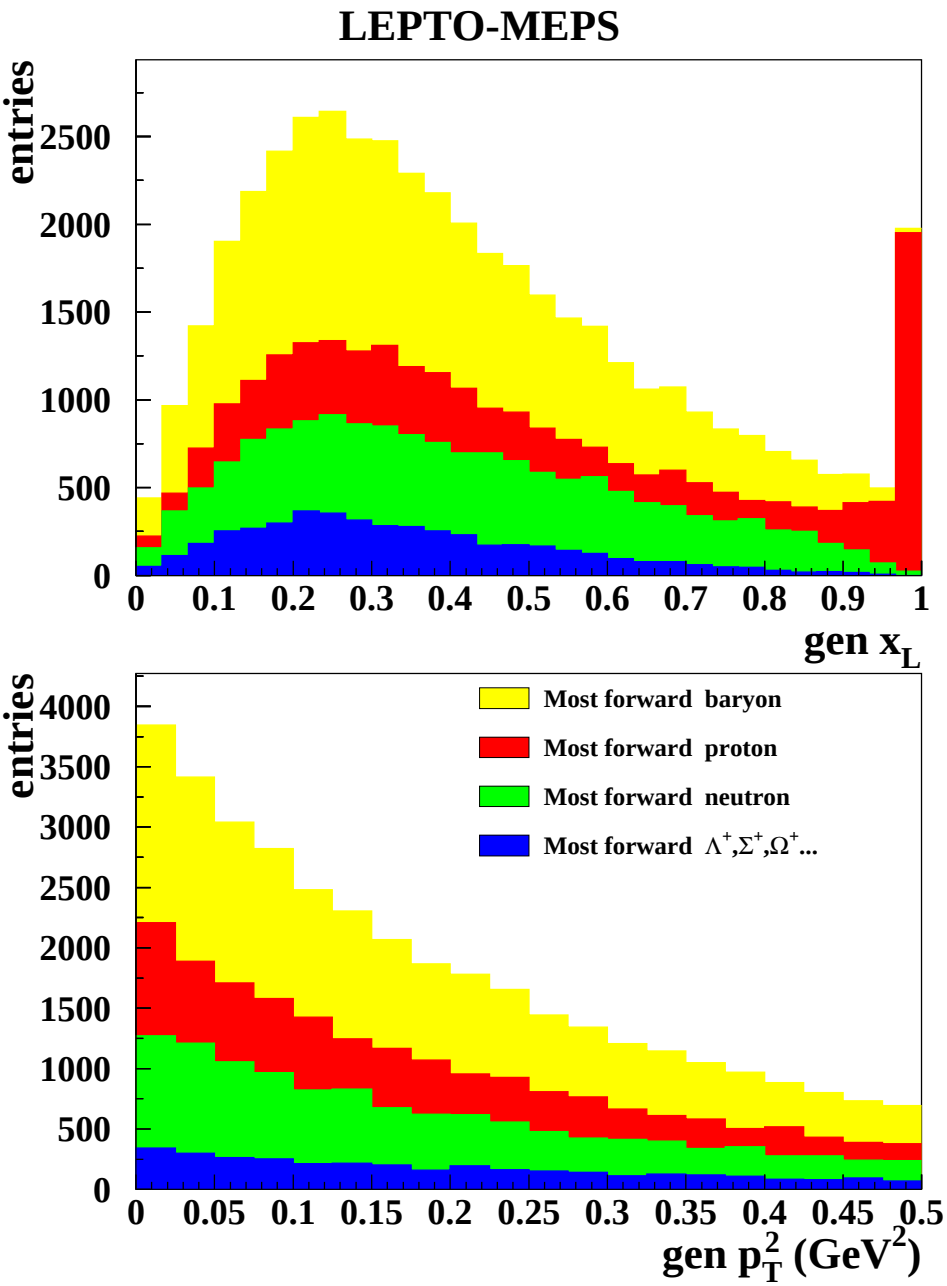

Figure 4.1: *Generated x_L and p_T^2 spectra of the leading-baryons as simulated in LEPTO-MEPS. The most forward baryon is the one having the higher x_L.*

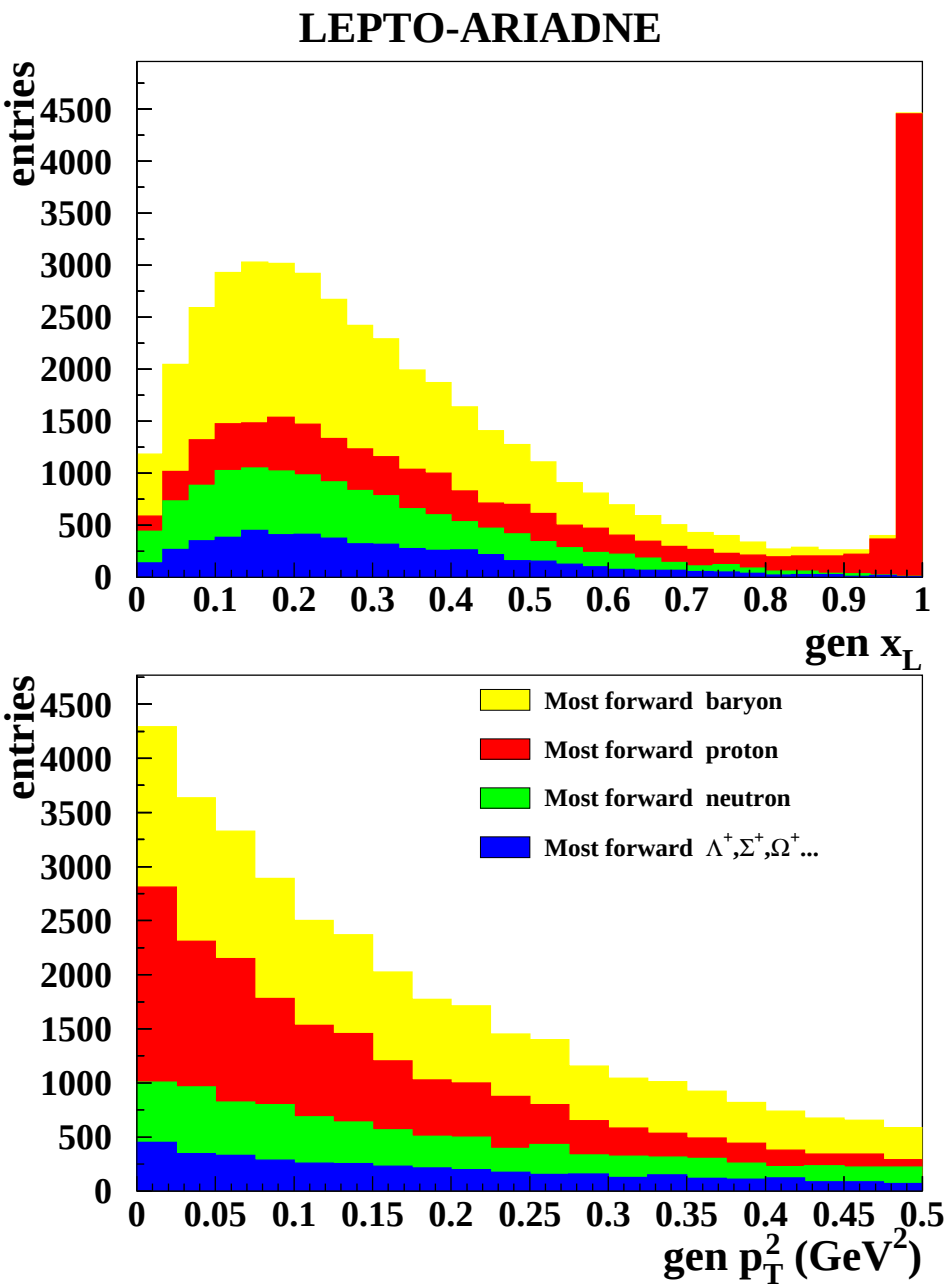

Figure 4.2: *Generated x_L and p_T^2 spectra of the leading-baryons as simulated in LEPTO-ARIADNE. The most forward baryon is the one having the higher x_L.*

Chapter 5

The event selection

The analysis has been performed using the data taken by the ZEUS experiment in 1997. During that year HERA collided protons of energy $E_p = 820$ GeV and positrons of energy $E_e = 27.5$ GeV. The integrated luminosity available for physics analysis gated by the ZEUS experiment is 27.85 pb^{-1}.

In 1997 the Leading Proton Spectrometer was fully operating and a large amount of statistics has been collected during that year. The LPS luminosity is 12.8 pb^{-1} for the spectrometer s456 and 9.0 pb^{-1} for the spectrometer s123.

The goal of the analysis is to measure the cross sections of the semi-inclusive process $e^+p \to e^+p'X$, with a leading-proton p' detected in the LPS, and to compare the leading-proton production rate to the inclusive DIS process $e^+p \to e^+X$. Even if the leading-proton production is a sub-class of the inclusive DIS processes, the selections of the LPS and DIS samples have to be carried out in a slightly different way and hence two distinct procedures were used.

The event selection chain that is going to be described, was applied to both data and Monte Carlo. For the latter a reweighting procedure was needed because the distributions of the leading-proton kinematic variables are not well simulated.

The main background sources after the event selection come from the interaction of the protons with the residual gas present in the beam-pipe due to the non-perfect vacuum, the detection in the LPS of charged mesons (mainly π^+ and K^+) mis-interpreted as protons and the migrations of events from photoproduction and low-Q^2 processes.

5.1 The DIS selection

The selection of inclusive DIS events requires a specific trigger chain and a set of cuts on the measured DIS quantities. The selection cuts are optimized to collect the maximum number of events in the kinematic region in which

the analysis is performed and to reject the background events. The main requirement for a DIS analysis is the presence of a scattered positron with enough energy (in order to measure $Q^2 \gtrsim 2$ GeV^2). The positron detection is related to the conservation of the quantity $E-p_z$, that is the total sum of the energy deposit minus the longitudinal momentum in the whole detector. Due to kinematics, this variable is expected to peak at twice the positron energy ($2E_e = 55$ GeV) when the positron is detected. In the photoproduction reactions the positron escapes through the beam-pipe and the $E-p_z$ results to be lower than 40 GeV. Very low or very high values of $E-p_z$ are associated to unphysical background processes. Indeed the $E-p_z$ is widely used in the selection procedures, either on-line (at the trigger level or at the generator level in the MC) and off-line.

Triggers. The trigger chain that is required is:

- FLT bit 46: a minimum energy deposit in the calorimeter or good tracks, vetoes related to non-*ep* events;
- SLT DIS01: $FLTDIS$ bits and $E - p_z + 2 * E_\gamma > 29$ GeV.

  The $FLTDIS$ is a combination of several FLT bits for the DIS selection. The quantity $E-p_z$ is calculated from the energy deposits in the calorimeter and the E_γ is the photon energy measured in the LUMI-γ detector.
- TLT DIS01 (LOW Q^2):
  - FLT DIS bits, SLT DIS bits,
  - $E - p_z + 2E_\gamma > 30$ GeV, $E - p_z < 100$ GeV,
  - reconstructed positron energy $E_e > 4$ GeV,
  - rejection of the events impinging on the RCAL in a 12×6 cm^2 box around the beam-pipe,
  - prescale=1 in run range 25190-25336 (equivalent luminosity 749.670 nb^{-1}),
  - prescale=100 in run range 25344-27889 (equivalent luminosity 270.956 nb^{-1}).

  If a trigger is prescaled of a factor N, it means that only one event every N is taken. The prescale is applied when a trigger has a very high rate in order to reduce the number of events to be acquired, nevertheless mantaining a high statistics for physics analysis.

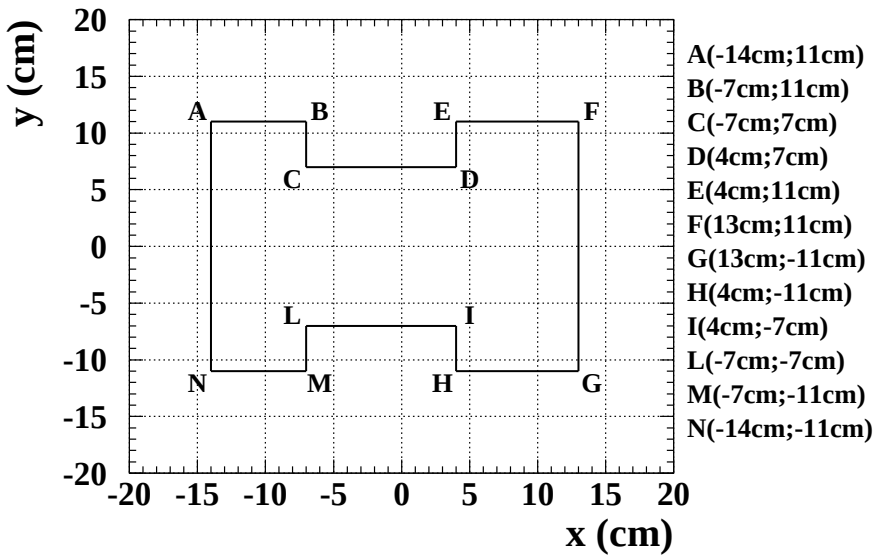

Figure 5.1: *H-box cut in the RCAL. The coordinates of the edges are reported.*

The positron quantities have been reconstructed using SINISTRA [57], an electron finder alghoritm based on neural networks. The list of the selection cuts applied off-line is:

- reconstructed vertex $-50 < z_{vtx} < 50$ cm;
- $38 < E - p_z < 65$ GeV; for an event fully contained in the detector, this quantity is expected to be $2E_e \simeq 55$ GeV. Lower values are associated to photoproduction events. In that case the positron emits a quasi-real photon ($Q^2 \approx 0$ GeV^2) and its momentum does not change significantly and it is lost in the beam-pipe. On the other hand, high $E-p_z$ are associated to the interaction of the protons with the residual gas in the beam-pipe and cosmic rays;
- a scattered positron with energy $E_e > 10$ GeV found by the electron finder. In addition it is required that the electron finder probability is greater than 90% and that the energy in a cone of radius $R = 0.8$ around the positron direction associated to hadronic activity is $E^{had}_{cone} <$ 5 GeV;
- H-box cut in the RCAL. Near the rear beam-pipe, the presence of inactive material reduces the precision of the positron energy measurement. A schematic picture of the box cut is reported in figure 5.1;

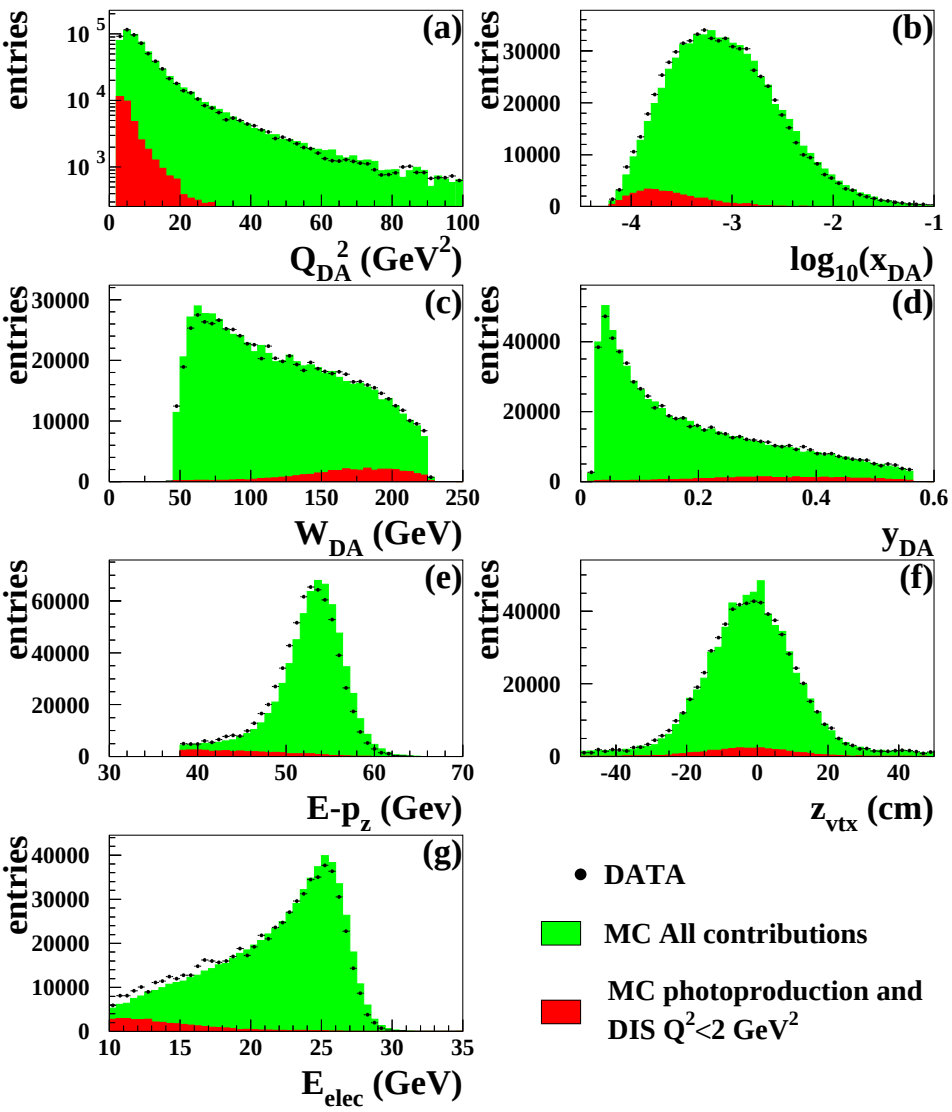

Figure 5.2: *DATA-MC comparison after the DIS selection. The dots are the real data distributions. The green histograms are the sum of all MC and are normalized to the data. The red histograms are the contribution of the events generated at low Q^2. (a) Photon virtuality Q^2_{DA} distribution; (b) Bjorken variable x_{DA} distribution; (c) invariant mass of the hadronic system W_{DA} distribution; (d) inelasticity y_{DA} distribution; (e) $E - P_z$ distribution; (f) z-vertex distribution; (g) scattered positron energy distribution.*

- virtuality of the exchanged photon $Q^2_{DA} > 3$ GeV and total hadronic mass $45 < W_{DA} < 225$ GeV.
- the hadronic variable $y_{JB} > 0.03$ in order to ensure hadronic activity away from the forward direction.

In figure 5.2 the distributions for the inclusive DIS are reported. The Monte Carlo describes quite well the data distribution. The small differences observable in the $E - p_z$, E_e and x_{DA} are due to the fact that the energy scale of the calorimeter is not corretly simulated. The number of events surviving to each DIS selection cut and the selection cut efficiency with respect to the intitial number of events are reported in table 5.1.

Cut	**# of selected events**	**Cut efficiency**
Before selection	2067878	–
Trigger	384994	18.62%
Positron cuts	353096	17.07%
H-box cut	280974	13.59%
$\|z_{vtx}\| < 50$ cm	277277	13.41%
$38 < E - p_z < 65$ GeV	264511	12.79%
$y_{JB} > 0.03$	200374	9.69%
$Q^2_{DA} > 3$ GeV^2	190129	9.19%
$45 < W_{DA} < 225$ GeV	139703	6.75%

Table 5.1: *The DIS selection cuts with the number of events after each cut and the cut efficiencies.*

5.2 The LPS selection

As explained in section 3.4, the Leading Proton Spectrometer is composed of six stations (s1→s6) , but it can be considered as a pair of two independent spectrometers: s123 and s456, formed by the group of stations s1-s2-s3 and mboxs4-s5-s6, respectively. Indeed s123 and s456 have different acceptances overlapping only in a small region.

Since the spectrometer s123 is the nearest to the interaction point, they are more sensitive to the proton kinematics and a small mis-calibration or mis-alignement of the stations and of the magnets could affect considerably the acceptance of the spectrometer. For this reason these stations have not been commissioned for a long time and up to now they have never been used for physics analysis.

The analysis will be mainly performed using the data collected with the LPS spectrometer s456. Since the work on the LPS spectrometer s123 is still

in progress, only some new, but yet preliminary result will be presented in chapter 7.

The LPS data selection is carried out with a different trigger configuration with respect to the inclusive DIS. The same DIS offline cuts are applied and in addition a further set of conditions are requested for a good quality track selection in the LPS.

DST bits and triggers The LPS data sample was first preselected using the Data Selection Trigger (DST) bits. At least one of the following DST has been requested to be fired:

- DST11, Nominal neutral current: TLT-NC and $E - p_z + 2E_\gamma > 30$ GeV;
- DST15, Diffractive bit: presence of a large rapidity gap ($\eta_{max} < 3$) or a track reconstructed in the LPS.

TLT-NC stands for a set of TLT requirements to select neutral current DIS events and η_{max} is the pseudorapidity of the most forward energy deposit in the calorimeter exceeding 400 MeV. The FLT and the SLT bits are the same used in the DIS selection. The following TLT trigger condition was requested:

- TLT DIS08 (DIS LPS):
  - FLT DIS bits, SLT DIS bits, $E - p_z > 30$ GeV,
  - reconstructed positron energy $E_e > 4$ GeV, LPS track,
  - 12×6 cm^2 box cut for RCAL positron.

The trigger chain selection was applied to data and Monte Carlo, with the exception of the TLT DIS08. This trigger condition is not well simulated in the MC, and therefore a study has been performed to apply a correction on the final result (section 5.8).

LPS selection cuts

- Good LPS run. During the data taking period, in some runs (or fraction of run) the LPS was excluded from the DAQ chain, because of the bad background conditions of the machine. The good LPS runs are selected taking into account the data taking conditions and the information from the data quality monitoring.
- A reconstructed track in the LPS with $x_L > 0.4$ and $p_T^2 < 0.5$ GeV^2.

Cut	# of selected events	Cut efficiency
Before selection	2067878	–
Track in LPS	221088	10.69%
Trigger	211298	10.21%
Positron cuts	188604	9.12%
H-box cut	151864	7.34%
$\|z_{vtx}\| < 50$ cm	148685	7.19%
$38 < E - p_z < 65$ GeV	141528	6.84%
$y_{JB} > 0.03$	106083	5.13%
$45 < W_{DA} < 225$ GeV	101084	4.89%
$Q^2_{DA} > 3$ GeV^2	79076	3.82%
$x_L > 0.4$	75484	3.65%
$p_T^2 < 0.5$ GeV^2	74104	3.58%
$\Delta_{pipe} > 0.04$ cm	71665	3.46%
$\Delta_{pot} > 0.02$ cm	68640	3.31%

Table 5.2: *The DIS selection cuts with the number of events after each cut and the cut efficiencies.*

- Minimum track distance from the beam-pipe, $\Delta_{pipe} > 0.04$ cm. This cut reduces the sensitivity of the LPS acceptance to the uncertainty on the location of the beam-pipe aperture.

- Minimum distance of the track from the edge of any LPS detector $\Delta_{pot} > 0.02$ cm. This cut ensures that the tracks were well within the active region of the silicon detectors.

The number of events surviving each selection criteria and the cut efficiency with respect to the initial number of events are reported in table 5.2.

5.3 The Monte Carlo reweighting

The Monte Carlo programs available for the simulation do not give a good description of the leading-proton quantities measured in the LPS and it was necessary to apply a reweighting procedure. In the Soft Colour Interaction model, used in the LEPTO Monte Carlo generator to simulate the diffraction, the number of events with a large rapidity gap is overestimated in the LPS acceptance region [58].

Hence, the LEPTO Monte Carlo was first reweighted by tuning the distributions of the leading-proton longitudinal and transverse momenta. Then a further weight factor was applied to correct the large rapidity gap distributions.

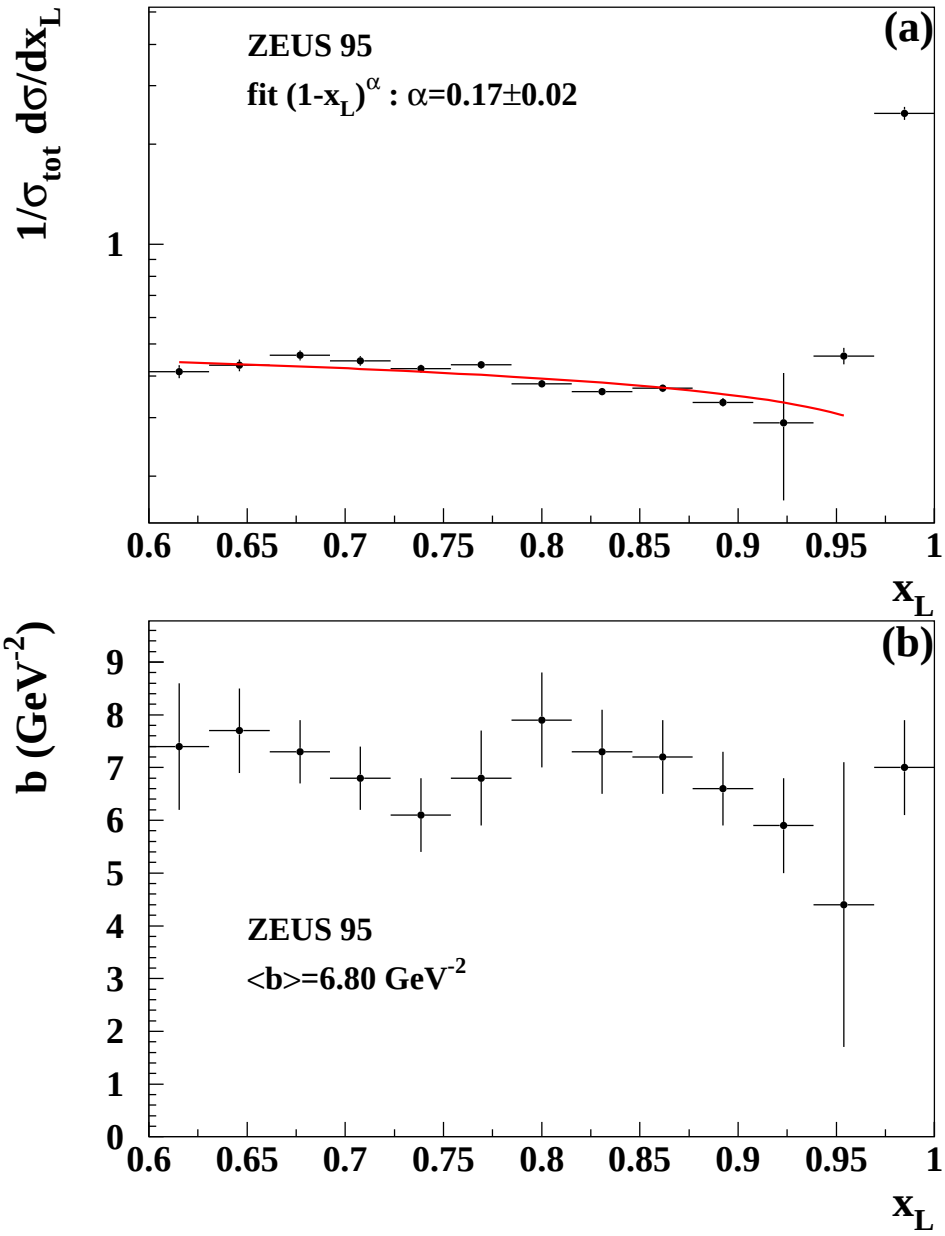

Figure 5.3: *Leading-proton measurement with ZEUS 1995 LPS data [8]. (a) Fit of the differential leading-proton cross sections normalised to the total DIS cross section* $1/\sigma_{tot} d\sigma/dx_L$ *to the function* $(1 - x_L)^\alpha$*. (b) Measured b-slope as a function of* x_L*.*

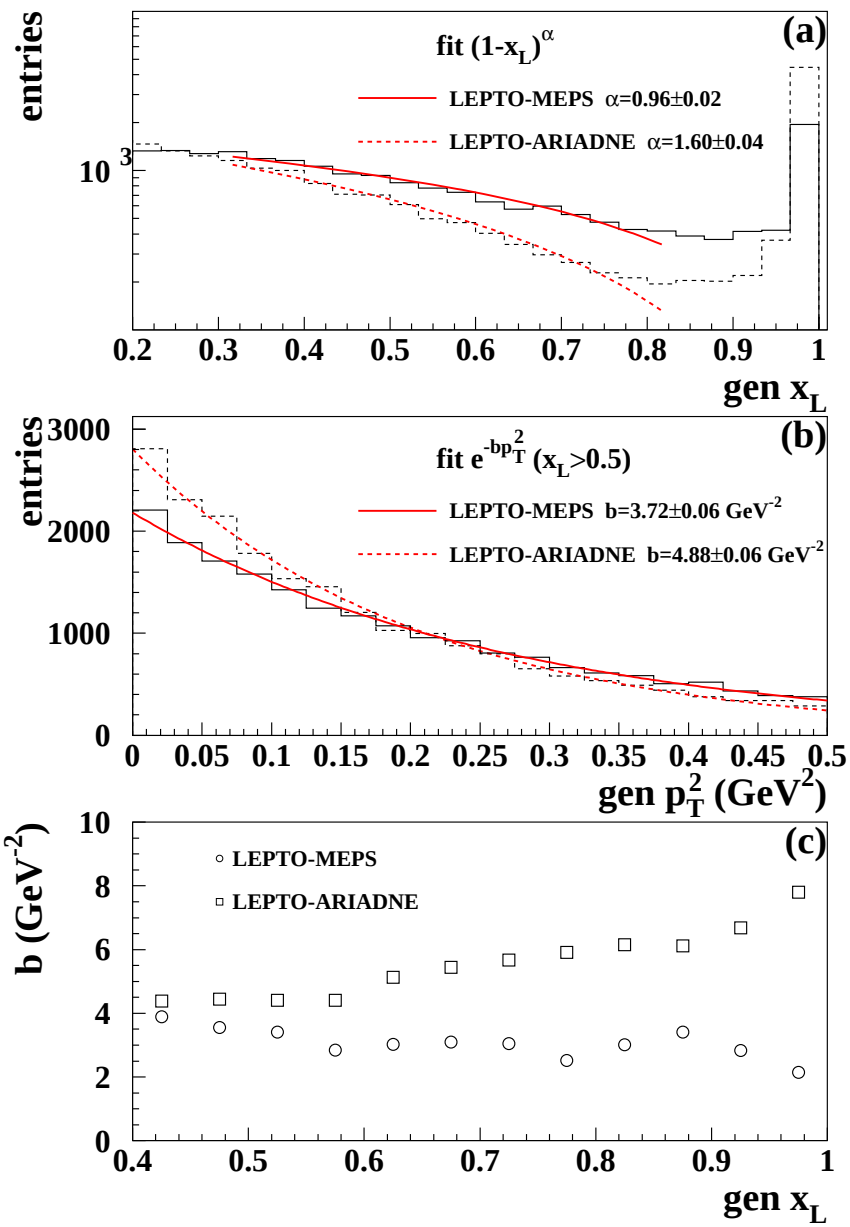

Figure 5.4: *Fit of the generated leading-proton momentum distributions for the Monte Carlo generators LEPTO-MEPS and LEPTO-ARIADNE. (a) Fit of the generated x_L distribution to the function $(1-x_L)^{\alpha}$. (b) Fit of the generated p_T^2 distribution to the function $\exp(-bp_T^2)$. (c) Generated b-slope as a function of x_L.*

Reweighting of the x_L and p_T^2 spectra The measurements of the leading-proton fractional longitudinal momentum x_L carried out in fixed target [4, 5] and DIS experiment [6–8], showed that the x_L spectrum can be approximated with the function $(1 - x_L)^\alpha$. This approximation is valid for non diffractive processes ($x_L \lesssim 0.95$). The parameter α can be evaluated from the fits of the differential cross sections $d\sigma/dx_L$ to the function $(1 - x_L)^\alpha$, and its value is found to be in the range $0 - 0.2$ (fig. 5.3a).

The squared transverse momentum p_T^2 spectrum falls down exponentially ($d\sigma/dp_T^2 \propto e^{-bp_T^2}$), as observed in fixed target experiment and DIS. The b-slope turned out to be ~ 6.80 GeV^{-2} with no strong dependence on x_L (fig. 5.3b).

In the LEPTO Monte Carlo, the longitudinal and transverse momentum spectra of the leading-proton differ significantly from the measurements. In particular, when MEPS is used for the hadronization, the x_L^{gen} spectrum[1] behaves like $(1 - x_L)^{\alpha_{MC}}$ with $\alpha_{MC} \simeq 1.$ and using the Colour Dipol Model (ARIADNE) we found $\alpha_{MC} \simeq 1.6$ (fig. 5.4a). The p_T^{2gen} spectrum has an exponential distribution, but with different slopes with respect to those measured (fig. 5.4b). In figure 5.4c the b-slopes were obtained from the fit of the p_T^2 distributions in x_L bins.

In the LEPTO-MEPS the mean slope is $b_{MC} \sim 3.7$ GeV^{-2} and it has a x_L dependence similar to the measured slopes. In the LEPTO-ARIADNE the mean slope is $b_{MC} \sim 4.9$, but the b_{MC} value rises slowly with x_L (fig. 5.4c).

Since the Monte Carlo does not describe the leading-proton quantities, the reweighting procedure is performed by tuning the leading-proton longitudinal and transverse spectra. The weight factor given to each event depends on the generated x_L^{gen} and p_T^{2gen} and is defined by:

$$w(x_L^{gen}, p_T^{2gen}) = \frac{(1 - x_L^{gen})^\alpha}{g(x_L^{gen})} \cdot \frac{e^{-bp_T^{2gen}}}{e^{-b_{MC}p_T^{2gen}}} \tag{5.1}$$

The function $g(x_L^{gen})$ describes the x_L^{gen} spectrum provided by the generator. In the case of diffractive events ($x_L^{gen} > 0.98$) the weight only depends on p_T^{2gen} and it is equal to the esponential ratio. The parameter α was set to zero as it was found to give the best description of the data. As a systematic check it was increased to 0.1. The b-slope was set to the measured value 6.8 GeV^{-2} and it was varied of ± 0.4 GeV^{-2} for the systematic checks (see section 6.3).

The leading-proton quantities measured in the LPS are well reproduced by the reweighted LEPTO-MEPS Monte Carlo and for this reason it was chosen as the main Monte Carlo generator. In figure 5.5 are reported the LPS quantities for the real data and the Monte Carlo, before and after the

[1] The *gen* superscripted variables refer to the generated quantities before the detector simulation.

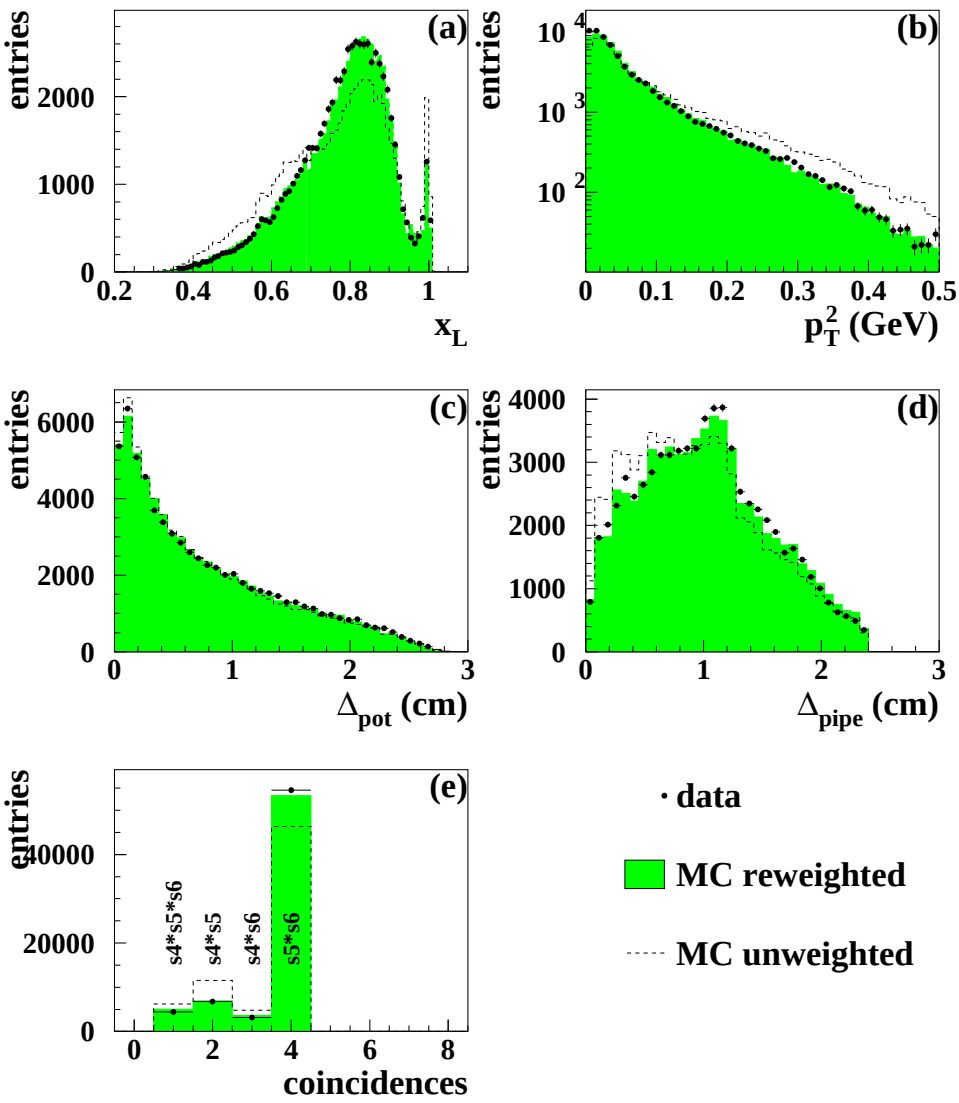

Figure 5.5: *Comparison of the LPS variables distribution with the MC before (dashed histogram) and after (green histogram) the leading-proton distributions reweighting. The MC distributions were normalised to the data. (a) fractional longitudinal momentum x_L distribution; (b) transverse momentum p_T^2 distribution; (c) minimum track distance from the edge of the pot Δ_{pot} distribution; (d) minimum track distance from the beam-pipe Δ_{pipe} distribution; (e) LPS station coincidence code distribution.*

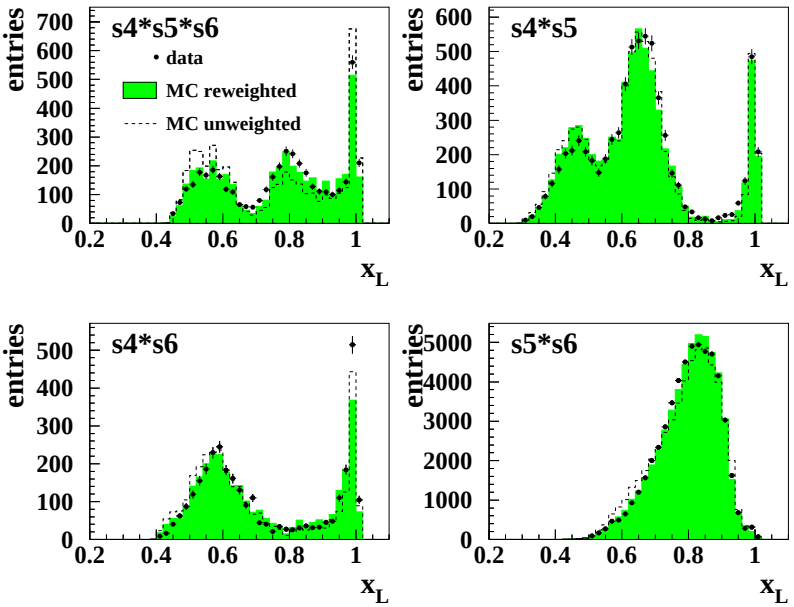

Figure 5.6: x_L *distributions for each LPS station coincidence.*

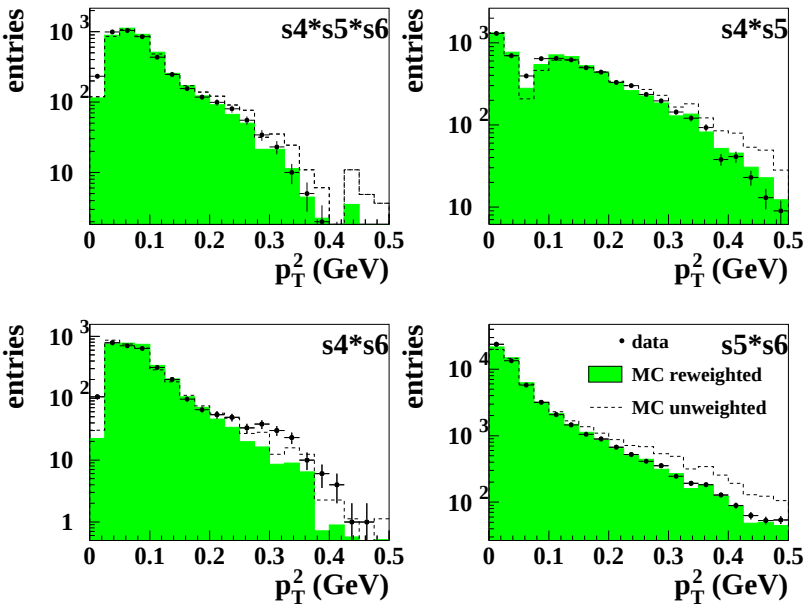

Figure 5.7: p_T^2 *distributions for each LPS station coincidence.*

reweighting procedure. In figures 5.6 and 5.7 , the x_L and p_T^2 distributions for each LPS coincidence combination (s4*s5*s6,s4*s5,s4*s6,s5*s6) are reported, respectively.

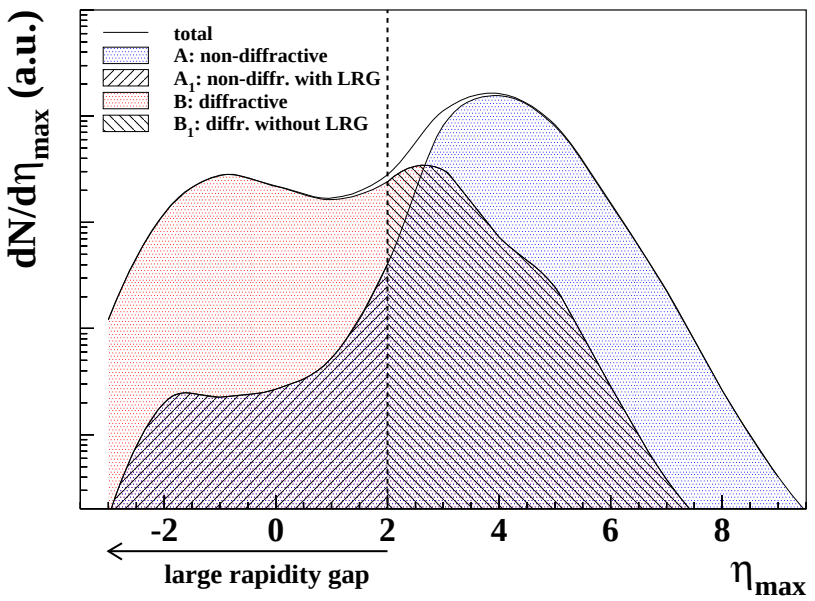

Figure 5.8: *Schematic view of the η_{max} distribution in a given x_L bin. The total η_{max} distribution (solid line) is the superposition of diffractive (red shaded-area B) and non-diffractive (blue shaded-area A) events. In evidence the subclasses of the diffractive events without LRG (hashed-area B_1) and non-diffractive events with a LRG (hashed-area A_1).*

Reweighting of rapidity gaps Although the LPS quantities are well reproduced by the Monte Carlo after tuning the generated x_L^{gen} and p_T^{2gen} spectra, an excess of events with a large rapidity gap is observed in the Monte Carlo. The excess is observed for those events having a leading-proton with low x_L, below the diffractive peak. The events with a large rapidity gap and low x_L come from the diffraction with proton dissociation. In order to correct for this effect, an additional weight has been applied to each event. Let us consider the η_{max} distibution in a given x_L analysis bin (figure 5.8), where η_{max} is the pseudorapidity of the most forward energy deposit in the calorimeter exceeding 400 MeV. Diffractive events usually have a large rapidity gap (defined by $\eta_{max} < 2$) because the QCD radiation between the proton and the photon vertex (fig 1.4) is sharply suppressed. The distribution shown in figure 5.8 comes from the superposition of two classes

of events: non-diffractive (A) and diffractive (B). Let us also consider the two subclasses of non-diffractive events with a large rapidity gap (A_1) and diffractive events without a large rapidity gap (B_1).

In the Monte Carlo it is possible to separate the diffractive and non-diffractive classes in the plane $x_L^{gen} - \Delta\eta$ (fig 5.9), where $\Delta\eta$ is the maximum gap in rapididy between two final-state hadrons calculated at the generator level. The function $\Delta\eta_{cut}(x_L^{gen})$ shown in the figure was evaluated empirically. In the $x_L^{gen} - \Delta\eta$ plane, the diffractive events have $\Delta\eta > \Delta\eta_{cut}$ and are assigned to class B (B_1 if the reconstructed $\eta_{max} > 2$).

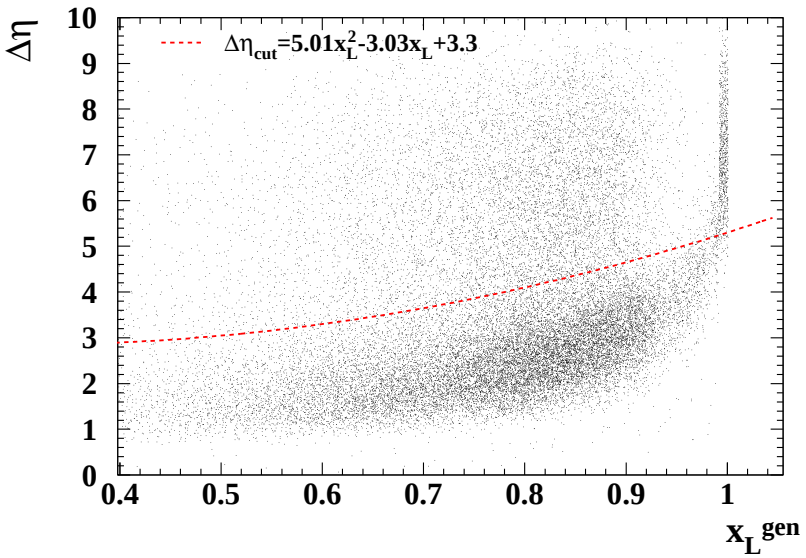

Figure 5.9: *Plane $x_L^{gen} - \Delta\eta$. The events with $\Delta\eta > \Delta\eta_{cut}$ are tagged as diffractive.*

From the above definitions, it is possible to calculate the weights w_{diff} to be assigned to the diffractive events for each x_L bin.

Let us define the quantities:

$$R^{data} = \frac{data^{LRG}}{data^{TOT}}, \qquad R^{MC} = \frac{MC^{LRG}}{MC^{TOT}}, \tag{5.2}$$

where $data^{LRG}$ and MC^{LRG} are the events with $\eta_{max} < 2$. For the MC is valid the following:

$$MC^{LRG} = A_1 + B - B_1, \qquad MC^{TOT} = A + B, \tag{5.3}$$

The weight factor is calculated imposing that R^{data} is equal to the diffractive-weighted R^{MC}:

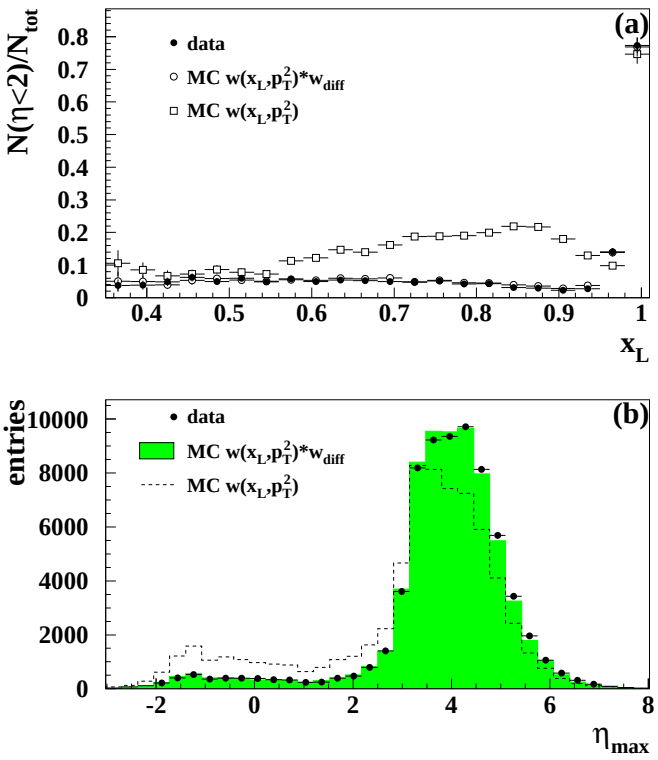

Figure 5.10: *(a) Fraction of events with a large rapidity gap ($\eta_{max} < 2$) as a function of x_L. The black filled dots are the data. The white squares represent the MC reweighted only in x_L and p_T^2 and the white circles represent the MC after the rapidity gaps reweighting; (b) η_{max} distribution for data and Monte Carlo before (dashed line) and after (green histogram) the rapidity gap reweighting.*

$$R^{data} = \frac{A_1 + (B - B_1)w_{diff}}{A + B * w_{diff}}, \tag{5.4}$$

and hence

$$w_{diff} = \frac{A * R^{data} - A_1}{B(1 - R^{data}) - B_1}. \tag{5.5}$$

This weight alone is not sufficient, and it is necessary another factor to take into account the conservation of total number of events:

$$w_{all} = \frac{A + B}{A + Bw_{diff}} \tag{5.6}$$

The weight w_{diff} is then applied to all MC diffractive events (those for which $\Delta\eta > \Delta\eta_{cut}$) while w_{all} is applied to all the events. This reweighting procedure modifies the η_{max} distribution and does not affect the leading-proton momentum. The fraction of events with a LRG as a function of x_L is now well reproduced by the Monte Carlo (fig. 5.10).

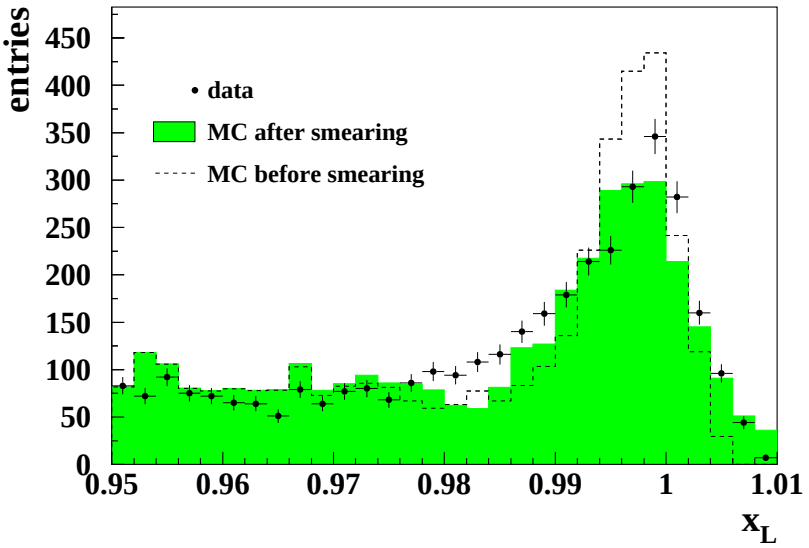

Figure 5.11: *Comparison data-MC at $x_L > 0.95$, before (dashed line) and after (green histogram) the smearing of the diffractive peak.*

Diffractive peak smearing. The last Monte Carlo tuning consists in a "smearing" of the diffractive peak to better reproduce the LPS resolution. For the MC events having $x_L > 0.95$, the quantity $0.8(x_L^{LPS} - x_L^{gen})$ is added to x_L^{LPS} when $|x_L^{LPS} - x_L^{gen}| < 0.05$, where x_L^{LPS} is the value of x_L reconstructed from the track parameters. In this way also the diffractive peak is better simulated (fig 5.11).

5.4 Comparisons data-MC

After all the reweighting and smearing procedures were applied, a comparison between the distributions of the real data and Monte Carlo quantities is carried out. The contribution coming from photoproduction ($Q^2 \approx 0.$ GeV^2) and DIS events with $Q^2 > 0.5$ GeV^2 are also included. The Monte Carlo samples for the three processes are normalised to the total number of events in the data, according to their luminosities (see section 4.3).

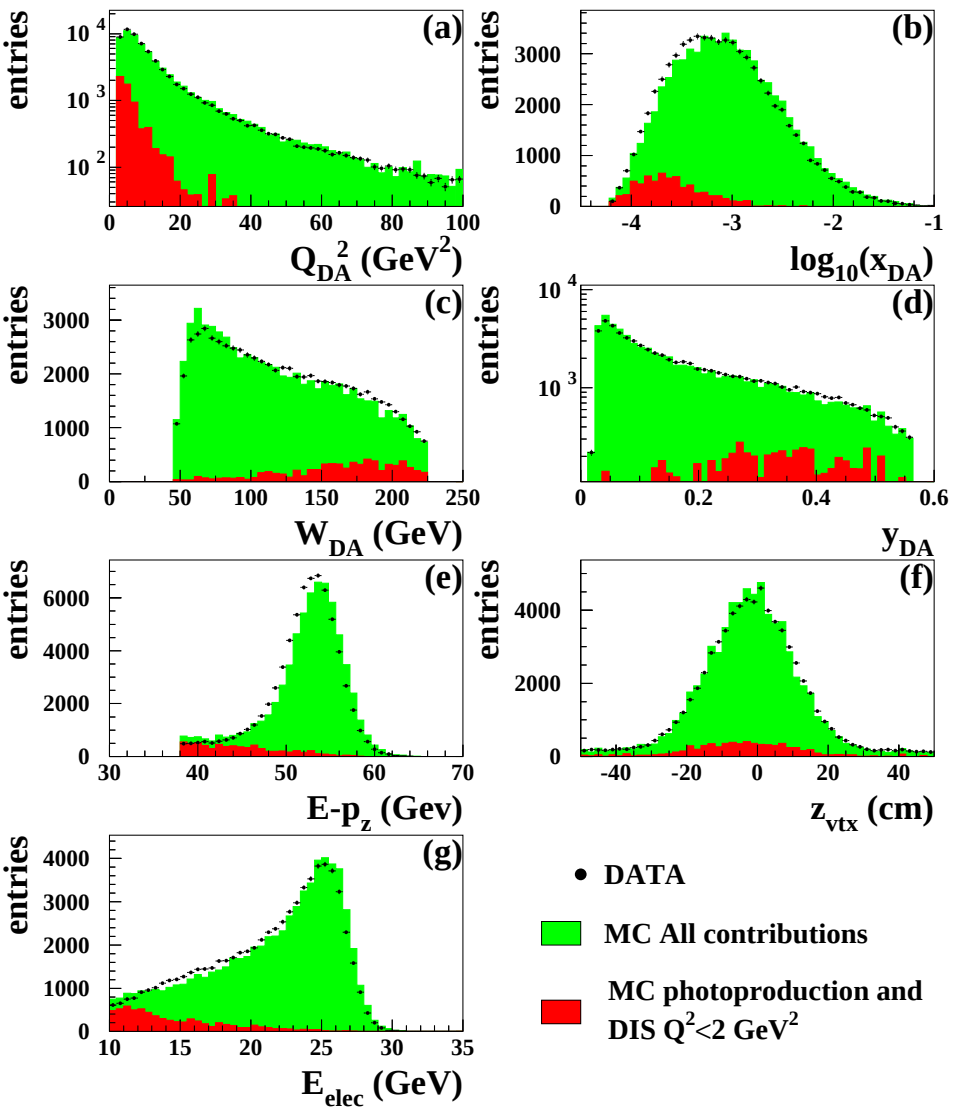

Figure 5.12: *DATA-MC comparison after the LPS selection. The dots are the real data distributions. The green histograms are the sum of all MC and are normalized to the data. The red histograms are the contribution of the events generated at low-Q^2. (a) photon virtuality Q^2_{DA} distribution; (b) Bjorken variable x_{DA} distribution; (c) invariant mass of the hadronic system W_{DA} distribution; (d) inelasticity y_{DA} distribution; (e) $E - P_z$ distribution; (f) z-vertex distribution; (g) scattered positron energy distribution.*

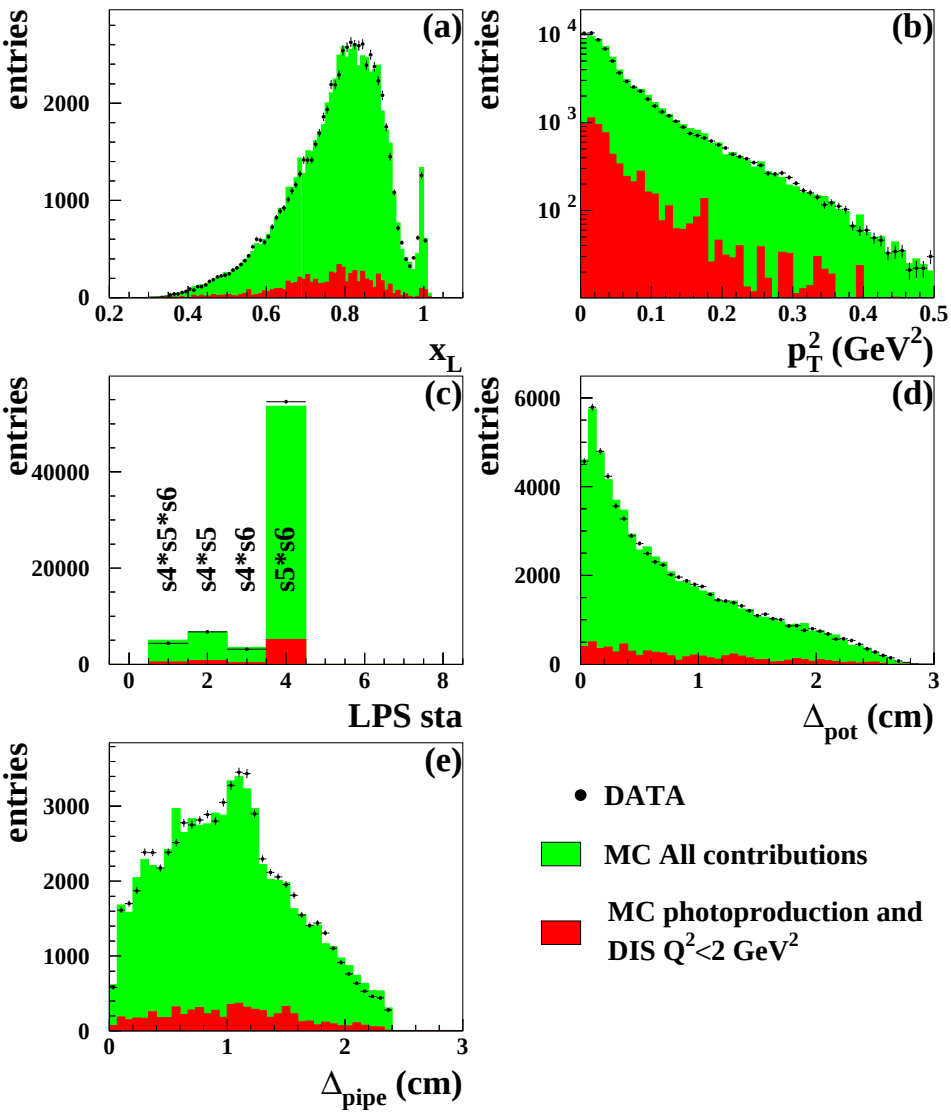

Figure 5.13: *DATA-MC comparison for the LPS quantities after the LPS selection. The dots are the real data distributions. The green histograms are the sum of all MC and are normalized to the data. The red histograms are the contribution of the events generated at low-Q^2. (a) fractional longitudinal momentum x_L distribution; (b) transverse momentum p_T^2 distribution; (c) LPS station coincidence code LPSsta distribution; (d) minimum track distance from the edge of the pot Δ_{pot} distribution. (e) minimum track distance from the beam-pipe Δ_{pipe} distribution;*

In figure 5.12 the same distributions shown in figure 5.2 for the inclusive DIS sample are plotted when a leading-proton is tagged. The Monte Carlo describes well the data characteristics when a leading-proton is detected in the LPS. It can be noticed that the reweighting does not affect the DIS quantities, as expected.

Finally in figure 5.13 the LPS quantities are shown: the reweighted Monte Carlo gives a very good description of the leading-proton kinematics (fig. 5.13 *a* and *b*) and of other quantities that characterize the LPS reconstrucion, as the number of events in each LPS station coincidence (fig. 5.13*c*) and the variables Δ_{pot} (fig. 5.13*d*) and Δ_{pipe} (fig. 5.13*e*).

The correct simulation of the leading-proton quantities is crucial, since the Monte Carlo simulation will be used to calculate the LPS acceptance, as shown in chapter 6.

5.5 Migrations from photoproduction and low Q^2 processes

The measurement of the leading-proton production cross sections will be carried out in the kinematic range $Q^2 > 3$ GeV^2 and $45 < W < 225$ GeV. The data set has been selected requiring $Q^2_{DA} > 3$ GeV^2 and $45 < W_{DA} < 225$ GeV. Due to the finite resolution a certain number of events "migrates" from outside the kinematic domain in which the measurement is performed. The migration is studied with the Monte Carlo, since the generated kinematic quantities are exactly known.

In this analysis the main Monte Carlo sample was generated requiring $Q^{2gen} > 2$ GeV^2, in order to enhance the selection efficiency, but this sample is not sufficient for a full study of the migrations. It is necessary also to consider the events with $Q^{2gen} < 2$ GeV^2 and two more Monte Carlo samples have been produced for this purpose, as explained in section 4.3.

The correction factor was evaluated using the Monte Carlo, considering the fraction of the leading-proton x_L and p_T^2 distributions of the low-Q^2 sample that survives the final selection.

In figure 5.14 the x_L and p_T^2 distributions of the events generated with $Q^{2gen} > 0.5$ GeV^2 are shown. In this case the average fraction of migrated events is 0.0270 ± 0.0006. In figure 5.15 the photoproduction sample is reported and the fraction is found to be 0.0745 ± 0.0011.

5.6 Background from overlay events

The overlay events are caused by the interaction of the beam proton with the residual gas in the beam-pipe and by the halo of particles surrounding the proton beam. Most of the overlay events are usually rejected by the trigger decision logic and by the $E - p_z$ selection cut. The protons interacting

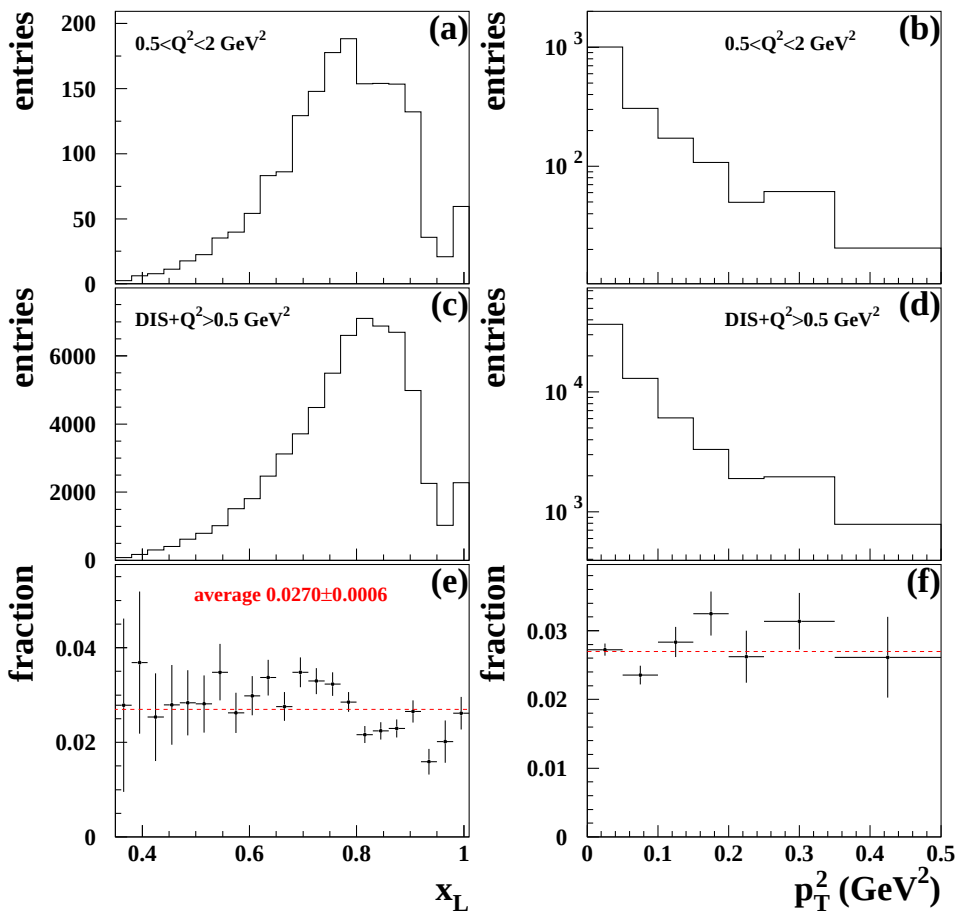

Figure 5.14: *Migrations from* $0.5 < Q^2 < 2\ GeV^2$. *(a)* x_L *distribution of the events with* $0.5 < Q^{2gen} < 2\ GeV^2$; *(b)* p_T^2 *distribution of the events with* $0.5 < Q^{2gen} < 2\ GeV^2$; *(c) sum of* x_L *distributions of the events with* $0.5 < Q^{2gen} < 2\ GeV^2$ *and DIS sample with* $Q^{2gen} > 2\ GeV^2$; *(d) sum of* p_T^2 *distributions of the events with* $0.5 < Q^{2gen} < 2\ GeV^2$ *and DIS sample with* $Q^{2gen} > 2\ GeV^2$; *(e) Fraction of the events with* $0.5 < Q^{2gen} < 2\ GeV^2$ *on the total as a function of* x_L, *the dashed line is the average fraction; (e) Fraction of the events with* $0.5 < Q^{2gen} < 2\ GeV^2$ *on the total as a function of* p_T^2, *the dashed line is the average fraction.*

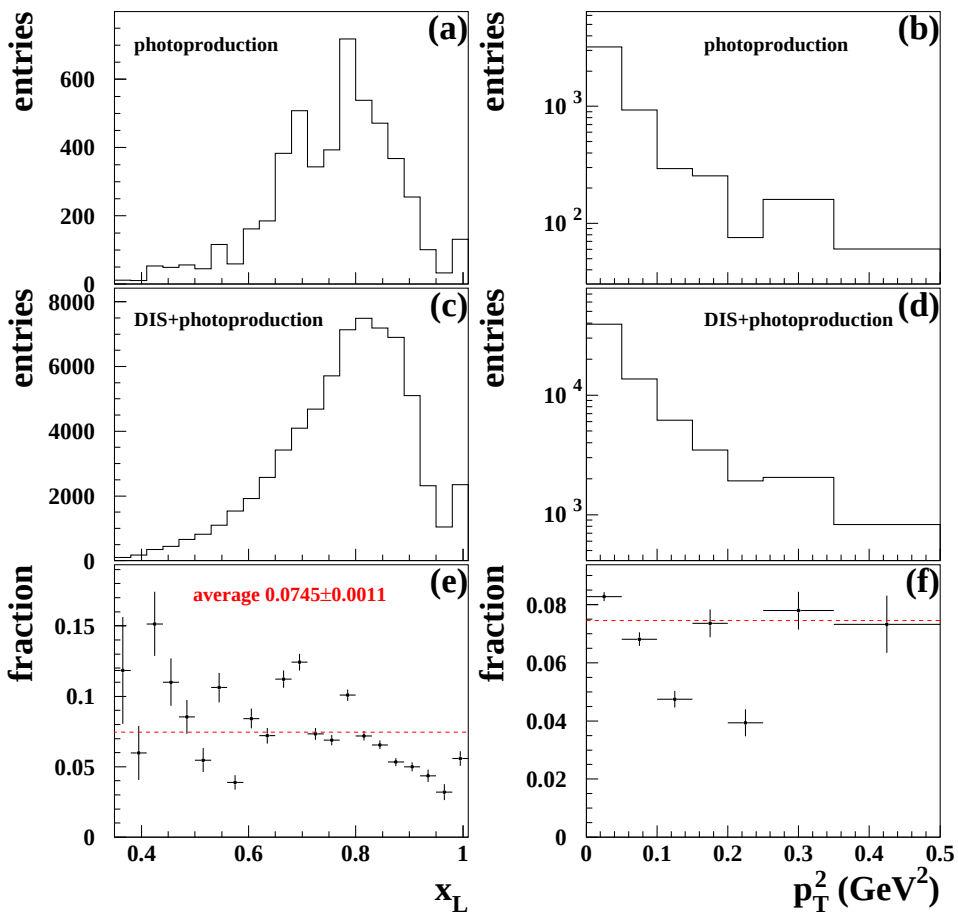

Figure 5.15: *Migrations from photoproduction. (a) x_L distribution of the photoproduction events; (b) p_T^2 distribution of the photoproduction events; (c) sum of x_L distributions of the photoproduction events and DIS events with $Q^{2gen} > 2$ GeV^2; (d) sum of p_T^2 distributions of the photoproduction events and DIS events with $Q^{2gen} > 2$ GeV^2; (e) Fraction of the photoproduction events on the total as a function of x_L, the dashed line is the average fraction; (e) Fraction of the photoproduction events on the total as a function of p_T^2, the dashed line is the average fraction.*

with the beam-pipe gas are scattered at very small angles, carrying a large fraction of initial momentum, and they can be detected in the LPS. The rate of the overlay events is assumed to be approximately constant over the running period. The overlay events can be rejected by imposing a cut on the

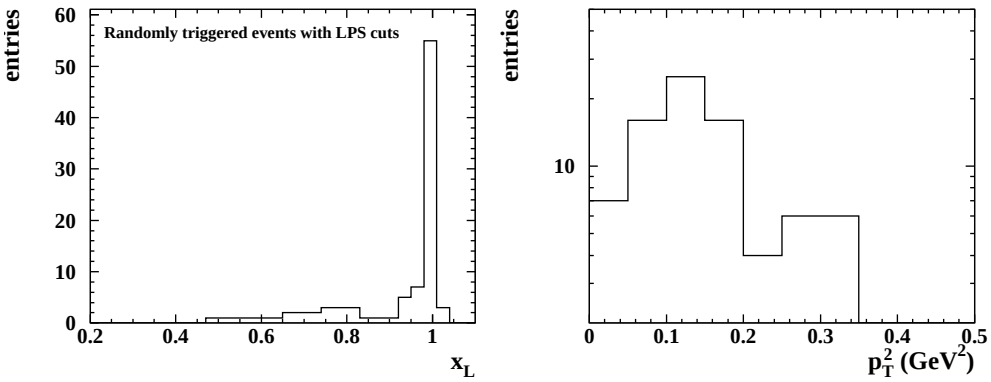

Figure 5.16: *x_L (left) and p_T^2 (right) distributions of the randomly triggered events.*

quantity $E + p_z$, calculated by summing over all the energy deposits in the calorimeter and in the LPS. For an event fully contained in the detector, this variable is expected to be twice the incoming proton energy, $E + p_z = 1640$ GeV. The background proton in the LPS tends to increase the total $E + p_z$.

Since the overlay events are uncorrelated to the DIS processes, they can be triggered by a special class of trigger bits that fire randomly. In our case a small sample of overlay events has been selected using the FLP16 trigger bit[2] and requiring the LPS selection cuts. A total of 80 events has been found and the x_L and p_T^2 spectra of the overlay events are shown in figure 5.16.

Given an inclusive DIS data sample, one can assign to each event a leading-proton having a momentum which is generated accordingly to the x_L and p_T^2 spectra of the randomly triggered events. In this way it is possible to build the $E+p_z$ distribution expected for the overlay events. Using the $E+p_z$ distribution for the LPS data sample and for the overlay events, a cut on $E+p_z$ can be determined by comparing the two distributions (Fig. 5.17). The relative normalisation between the two samples was determined by imposing that the areas at $E + p_z > 1700$ GeV are equal. The events with $E + p_z > 1655$ GeV have been rejected. The remaining overlay events with $E + p_z < 1655$ GeV will be subtracted in each x_L analysis bin from the cross section measurement. The fraction of subtracted events is $< 1\%$ for $x_L < 0.95$ and rises up to 8% in the diffractive region (see figure 5.18 and table A.1).

[2]The FLP16 trigger bit fires randomly and therefore the selected events are totally uncorrelated to any spacific physical process and are used for the study of the background.

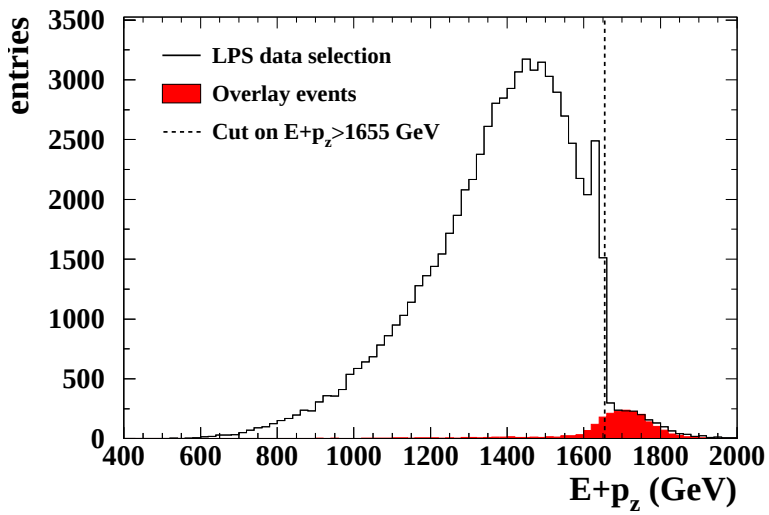

Figure 5.17: *Distribution of $E+p_z$ for the LPS event sample (solid line) and overlay events (red histogram). The dashed line indicates the cut applied for the overlay events rejection.*

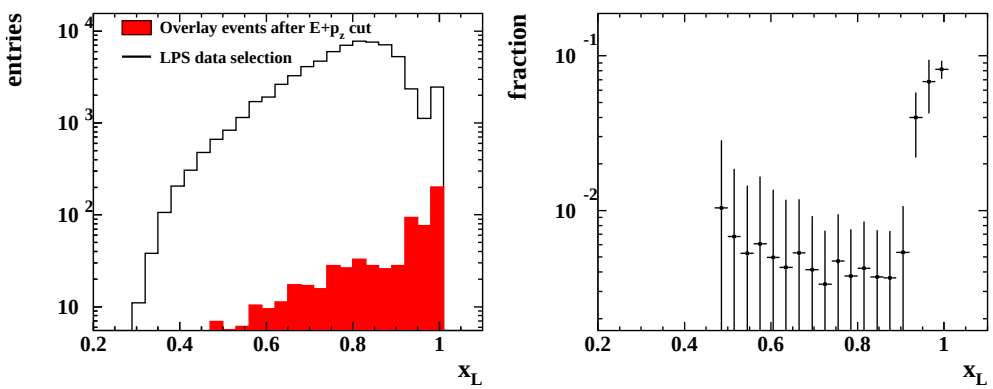

Figure 5.18: *Left: x_L distribution of LPS data sample (solid line) and of the overlay events surviving the $E+p_z$ cut (red histogram). Right: fraction of overlay event to be subtracted from the final results as a function of x_L.*

5.7 Background from π^+ and K^+

Another source of background comes from the reactions $ep \to en\pi^+X$ and $ep \to enK^+X$, in which the incoming proton momentum is shared between the leading-neutron n and the meson π^+ or K^+. When the leading-neutron has low longitudinal momentum, then the mesons π^+ or K^+ can be detected in the LPS. The background from π^+ and K^+ has been studied with the Monte Carlo. The LPS track is assigned to the particle (p, π^+, K^+) having the reconstructed x_L^{LPS} closer to the generated x_L^{gen} (minimum $\Delta x_L = |x_L^{LPS} - x_L^{gen}|$). It was found that the fraction of tracks associated to a π^+ or a K^+ grows up as x_L goes down (as expected from the decay of resonances $R \to n\pi(K)$) and it is almost independent from p_T^2. In figure 5.19 are reported the distributions of the reconstructed x_L of the leading protons and of the π^+ and K^+, as well as the meson fractions as a function of x_L. In figure 5.20 the same study is repeated as a function of p_T^2.

The fraction of events with a meson in the LPS are reported in the table A.2 and they will be used to correct the cross section measurements.

5.8 Trigger effects

The third level trigger TLT DIS08 (section 5.2) in the Monte Carlo is not well simulated. Let us define the trigger efficiency as:

$$\varepsilon = \frac{N_{events}^{\text{DIS08 on}}}{N_{events}^{\text{DIS08 off}}}, \tag{5.7}$$

after the full set of selection cuts is applied. Since the cuts required in the TLT DIS08 logic have also been applied off-line, ε is expected to be ≈ 1. In figure 5.21 and 5.22 it is shown the quantity ε for data and Monte Carlo as a function of x_L and p_T^2, resectively. In the Monte Carlo the TLT requirement totally changes the x_L and p_T^2 distributions, while in the data only a small fraction of events is cut away. For this reason the requirement of TLT DIS08 was applied only to the data, and in the calculation of the acceptance it is applied a correction factor given by eq. 5.7. The correction factors are listed in table A.3.

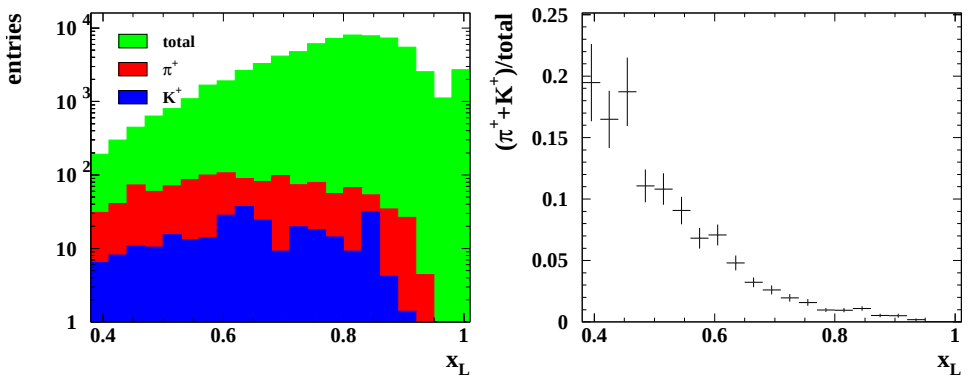

Figure 5.19: *Left: Monte Carlo x_L distribution when a π^+ is mis-reconstructed in the LPS (red histogram), when a K^+ is mis-reconstructed in the LPS (blue histogram) and total (green histogram). Right: fraction of events with a π^+ or K^+ on the total as a function of x_L.*

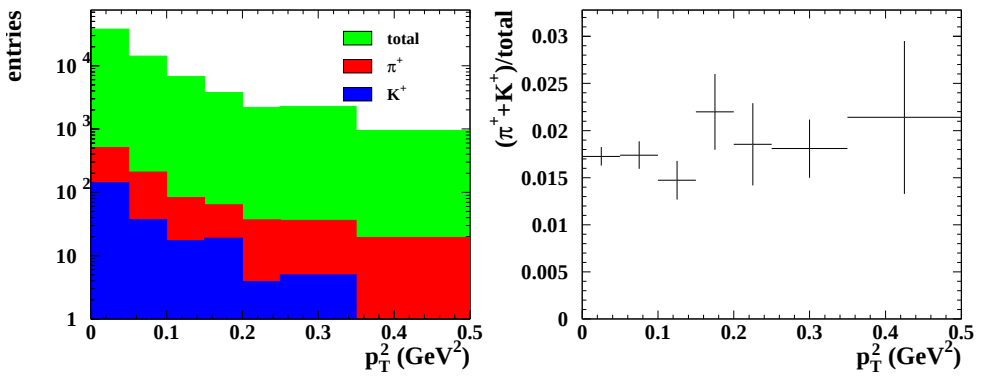

Figure 5.20: *Left: Monte Carlo p_T^2 distribution when a π^+ is mis-reconstructed in the LPS (red histogram), when a K^+ is mis-reconstructed in the LPS (blue histogram) and total (green histogram). Right: fraction of events with a π^+ or K^+ on the total as a function of p_T^2.*

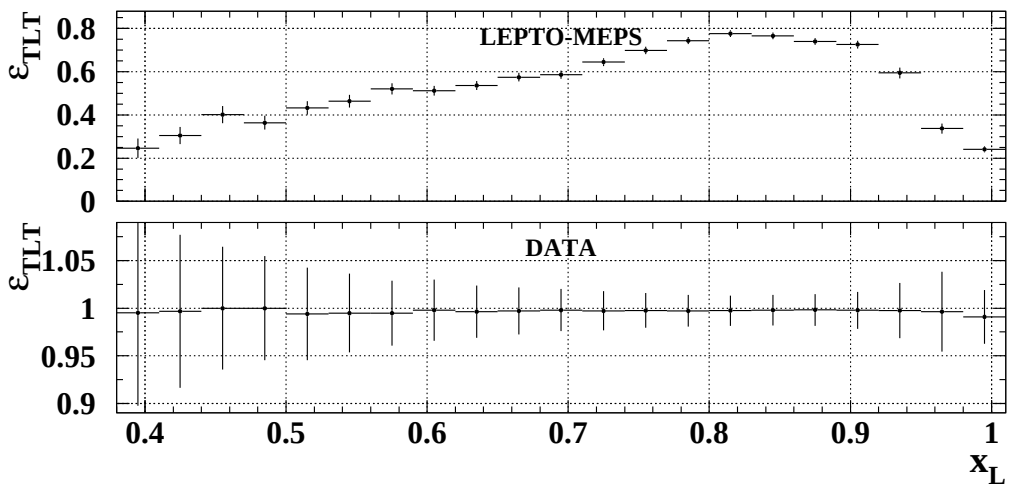

Figure 5.21: *Trigger efficiency ε_{TLT} as a function of x_L for the MC (up) and data (down).*

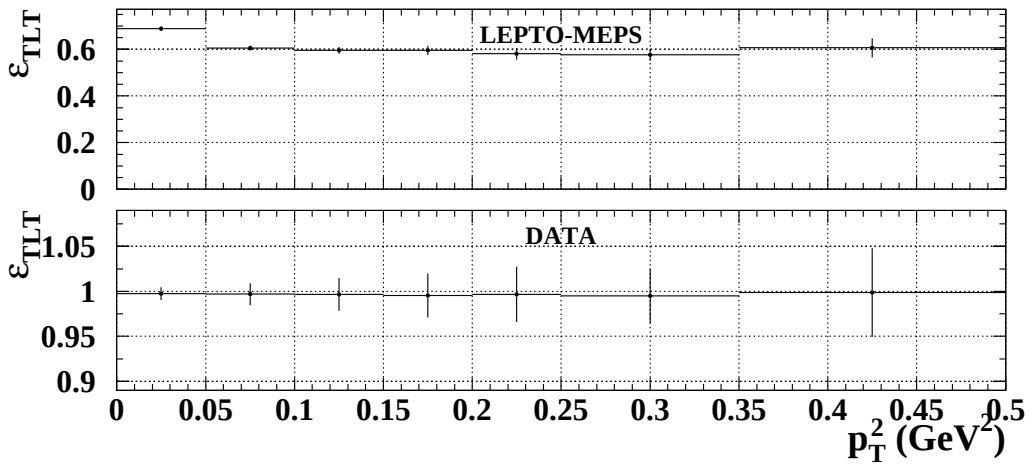

Figure 5.22: *Trigger efficiency ε_{TLT} as a function of p_T^2 for the MC (up) and data (down).*

Chapter 6

Measurement of the leading-proton production cross section

In this chapter a detailed description of the determination of the leading-proton production cross section is given. The general formulation of the cross section in a given kinematical range is given by:

$$\sigma = \frac{N^{data}}{A \cdot \mathcal{L}}, \tag{6.1}$$

where N^{data} is the number of data events after the selection cuts, $\mathcal{L}$ is the luminosity and A is the acceptance of the experimental apparatus (including the efficiency of the cuts), that corrects for geometrical and resolution effects.

After the calculation of the cross sections in x_L and p_T^2 and b-slopes, the ratios of leading-proton production to the inclusive DIS will be measured as function of the DIS kinematic variables x and Q^2.

The results will be then compared to the theoretical models and to the leading-proton measurements carried out in previous experiments.

The preliminary measurements of the leading-proton cross sections and of the b-slopes using the 1997 LPS data set were presented at the European Physical Society Conference in 2003 [59], while the published measurements of the ratios to the inclusive DIS were performed only with the ZEUS data collected in 1995 [8].

6.1 Resolution and binning

The choice of the analysis bin-width is strictly related to the resolution of the detector, that is evaluated using the Monte Carlo simulation, studying the distribution of the fractional residual:

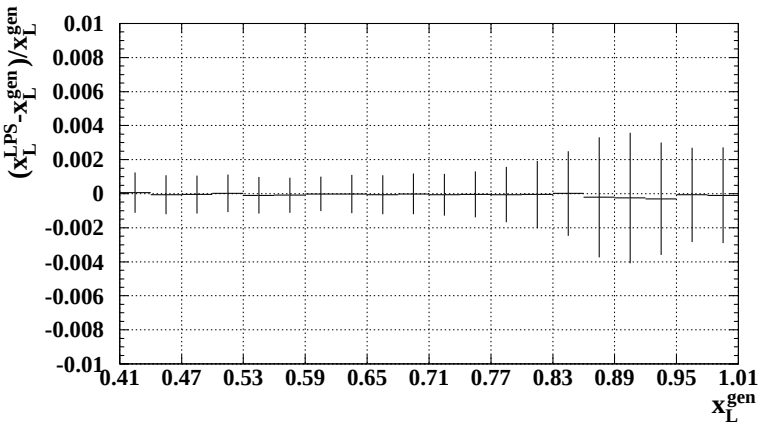

Figure 6.1: *Longitudinal momentum resolution as a function of* x_L^{gen}.

$$\delta = \frac{(x_L^{LPS} - x_L^{gen})}{x_L^{gen}} \tag{6.2}$$

where x_L^{gen} is the generated ("true") x_L value , while x_L^{LPS} is the value reconstructed by the LPS-reconstruction program. The mean value of the distribution of δ is called "bias", while its width gives a measure of the resolution. In figure 6.1 it is shown the bias as a function of x_L and the maximum resolution $\sigma(x_L)$ is $\simeq$0.4% for $x_L \gtrsim 0.85$. The Δx_L binning for each x_L value has been chosen such that:

$$\Delta x_L = 0.03 > x_L \sigma(x_L). \tag{6.3}$$

The p_T^2 resolution is dominated by the spread of the proton beam (fig. 6.2). In order to determine the Δp_T^2 bin width, the transverse squared momentum of the generated leading-proton has been calculated in two ways (using the generated quantities):

$$p_T^2 = (p_x - p_x^{beam} \cdot x_L)^2 + (p_y - p_y^{beam} \cdot x_L)^2, \tag{6.4}$$

where the transverse momentum is calculated with respect to the initial proton direction, and

$$p_T'^2 = p_x^2 + p_y^2. \tag{6.5}$$

The spread of the quantity $(p_T^2 - p_T'^2)/p_T'^2$ determines the resolution (fig. 6.3) and the Δp_T^2 bin width is chosen between 0.05 and 0.15 GeV. The resolutions and the bin widths in x_L and p_T^2 are summarised in table A.4.

Since the ratios to the inclusive DIS will be calculated as a function of the DIS variables x and Q^2, the resolution study has been carried out also for x and Q^2. The resolution plots are shown in figure 6.4. The bin widths have then been calculated according to the resolutions and are reported in table A.5. In the same table the mean values of the bin ,$\langle x_{DA} \rangle$ and $\langle Q_{DA}^2 \rangle$, are listed.

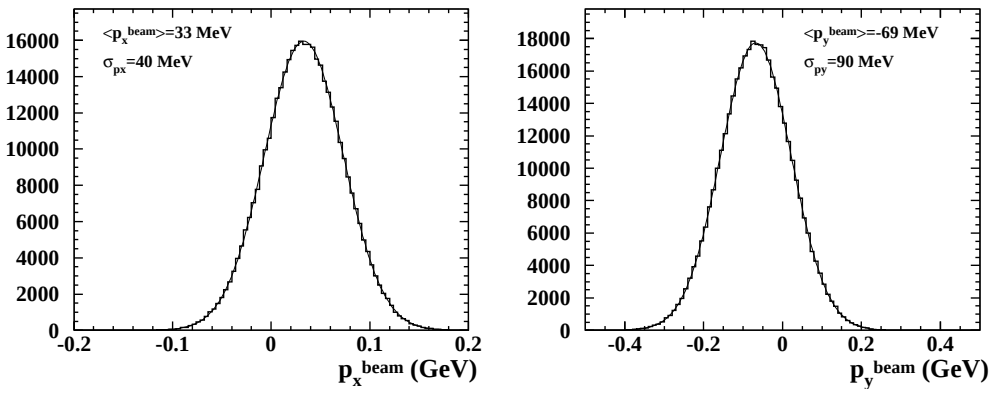

Figure 6.2: *Transverse momentum distribution of the proton beam (p_x^{beam} on the left and p_y^{beam} on the right) as simulated in the MC.*

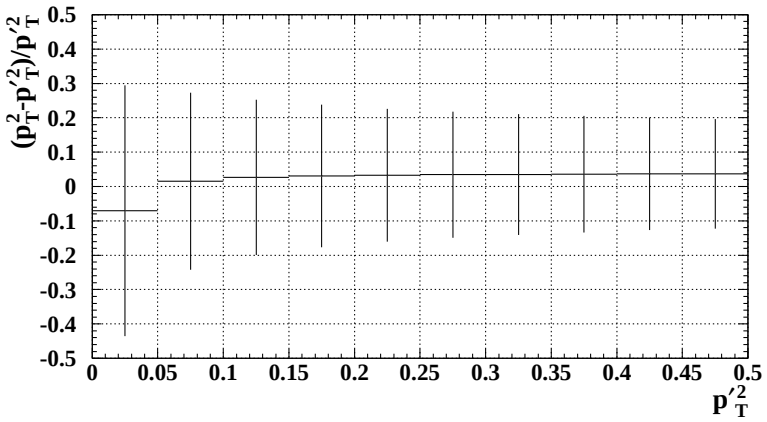

Figure 6.3: *Squared transverse momentum resolution as a function of $p_T'^2$*

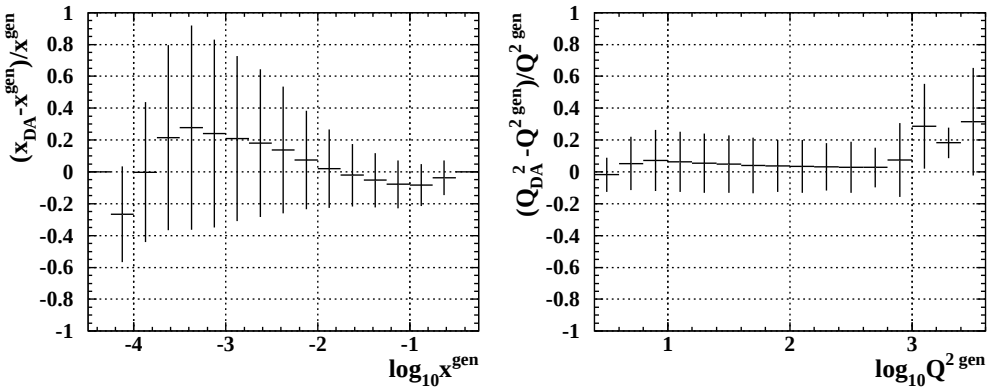

Figure 6.4: *Resolution of the DIS quantities x and Q^2.*

6.2 Acceptance

The acceptance, used for the definition of the cross section, is calculated using the Monte Carlo. It is defined as the ratio of the number of reconstructed events in a given analysis bin after the selection cuts (R) to the number of the events generated in that bin in the kinematic domain where the results will be quoted (G). The acceptance in a given x_L, p_T^2 bin is:

$$A(x_L, p_T^2) = \frac{R(x_L^{LPS}, p_T^{2LPS})}{G(x_L^{gen}, p_T^{2gen})}. \tag{6.6}$$

where x_L^{LPS} and p_T^{2LPS} are the variables reconstructed in the LPS and x_L^{gen} and p_T^{2gen} are the generated ("true") variables.

This definition includes the effects of the geometry, efficiency and resolution of the experimental apparatus and the event selection efficiency.

In the literature, the acceptance is also defined as the ratio of the efficiency to the purity. The efficiency is the ratio of the number of the events generated and reconstructed after the selection cuts ($\bar{R}$) to the number of the generated events (G) and is related to the effects of the selection procedure. In our case, the efficiency as a function of x_L and p_T^2 is given by:

$$\varepsilon(x_L, p_T^2) = \frac{\bar{R}(x_L^{gen}, p_T^{2gen})}{G(x_L^{gen}, p_T^{2gen})}, \tag{6.7}$$

The purity takes into account the geometry of the detector and it is defined as the ratio of the number of the generated and reconstructed events ($\bar{R}$) to the number of the reconstructed events after the selection cuts (R). The purity as a function of x_L and p_T^2 is given by:

$$\mathcal{P}(x_L, p_T^2) = \frac{\bar{R}(x_L^{gen}, p_T^{2gen})}{R(x_L^{LPS}, p_T^{2LPS})}. \tag{6.8}$$

The acceptance can be written as the sum of (omitting the index variables):

$$A = \frac{R_{in}}{G} + \frac{R_{out}}{G} = A_{in} + A_{out}, \tag{6.9}$$

where R_{in} is the number of events generated and reconstructed in the x_L, p_T^2 bin and R_{out} is the number of events reconstructed in the x_L, p_T^2 bin but generated in a different bin. As a first approximation R_{out} is uncorrelated with G, while R_{in} is certainly correlated with it. The error on A_{in} is therefore calculated from the binomial distribution:

$$\delta A_{in} = \sqrt{\frac{A_{in}(1 - A_{in})}{G}}. \tag{6.10}$$

Treating A_{out} as uncorrelated with G, we have:

$$\frac{\delta A_{out}}{A_{out}} = \sqrt{\frac{1}{R_{out}} + \frac{1}{G}}. \tag{6.11}$$

As discussed in section 5.3, the Monte Carlo events are reweighted and the "number " of events (R_{in}, R_{out}, G) to be considered is the number of "equivalent events", given by $N_{eq} = (\sum w_i^2)/\sum w_i^2$, where w_i are the weights associated to the events that populate the bin under consideration.

Finally the error on the acceptance is obtained by summing δA_{in} and δA_{out} in quadrature.

The acceptance in the x_L-p_T^2 plane is shown in figure 6.5 in a grey-level format. This plot gives an idea of the geometrical variation of the acceptance as a function of x_L-p_T^2. The larger acceptance values are in the region $0.74 < x_L < 0.86$ and $0 < p_T^2 < 0.05$ GeV^2 where the mean value is $\simeq 57\%$. In figure 6.6 the efficiency and the purity are plotted as a function of $x_L - p_T^2$. The efficiency is approximately distributed like the acceptance, reaching its maximum of $\simeq 50\%$ in the range $0.74 < x_L < 0.86$ and $0 < p_T^2 < 0.05$ GeV^2. The purity values are close to the unity in the most populated $x_L - p_T^2$ bins and become larger in the low acceptance regions.

In figure 6.7 the acceptance is plotted as a function of x_L (a), and p_T^2 (b). The acceptance reaches its maximum value of 23.4% at $0.80 < x_L < 0.83$ and 20% at $0 < p_T^2 < 0.05$ GeV^2. In the same figure are reported also the efficiency as a function of x_L (c) and p_T^2 (d) and the purity as a function of x_L (e) and p_T^2 (f). The values of the acceptance as a function of x_L and p_T^2 and the associated errors are reported in table A.6.

In figure 6.8 the acceptance in the $x_L - p_T^2$ plane is represented in a tabular format and in figure 6.9 are shown its relative errors.

In the analysis the bins where the acceptance is $< 1\%$ were excluded, since in those bins we can not rely on a good acceptance simulation. In figures 6.8 and 6.9 the excluded bins are written in red-italic font style. The measurements was carried out excluding also the region $x_L < 0.56$, since the acceptance in p_T^2 is limited in this range of x_L.

6.3 Systematic uncertainties

The measurements are affected by the dependence of the simulation on the physical processes, on the description of the detector and the beam-line elements and on the analysis cuts. To quantify the stability of the results against small variations of the analysis parameters, the measurements were repeated varying once at a time the following conditions:

- the slope of the generated p_T^2 distribution in the MC was reweighted to 6.4 and 7.2 GeV^{-2};

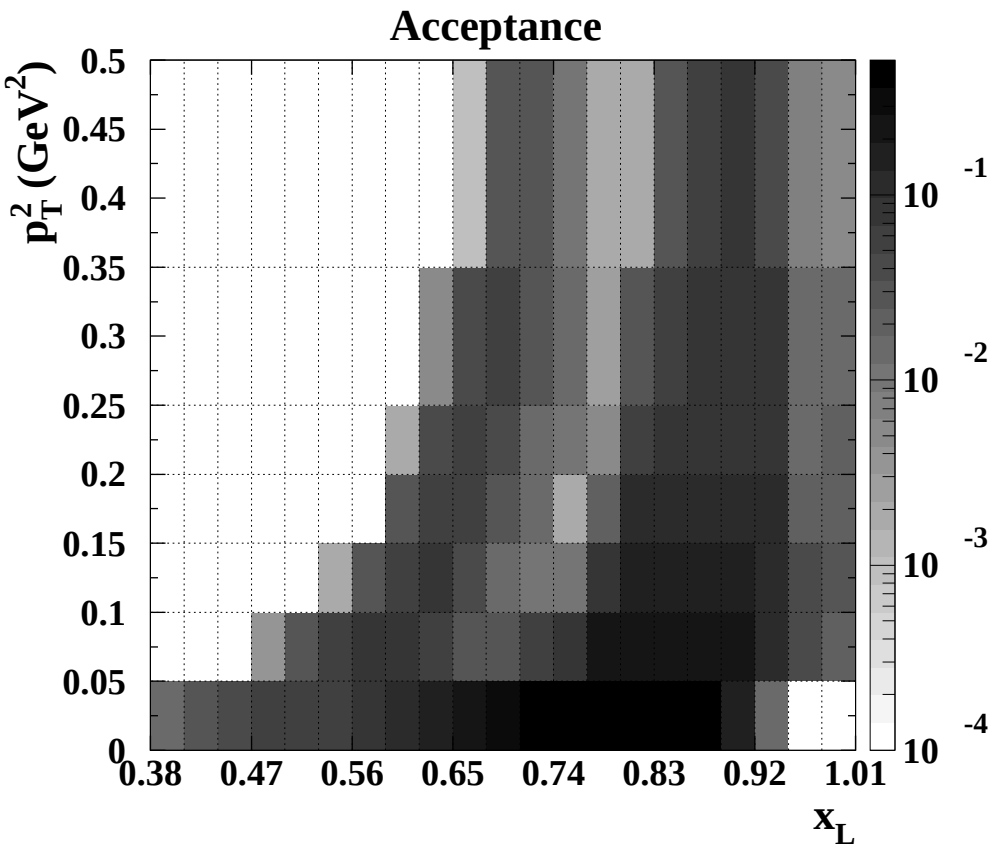

Figure 6.5: *Acceptance in the plane* $x_L - p_T^2$.

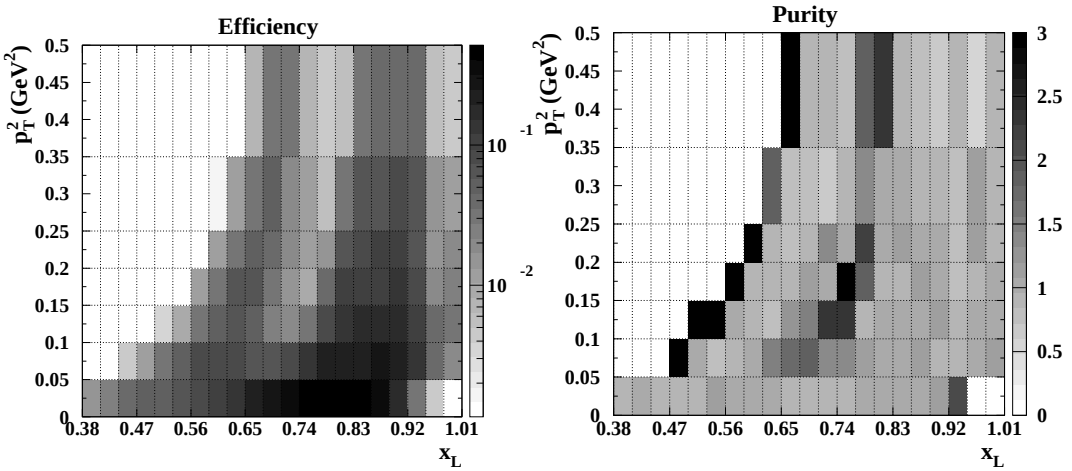

Figure 6.6: *Efficiency (left) and Purity (right) in the plane* $x_L - p_T^2$.

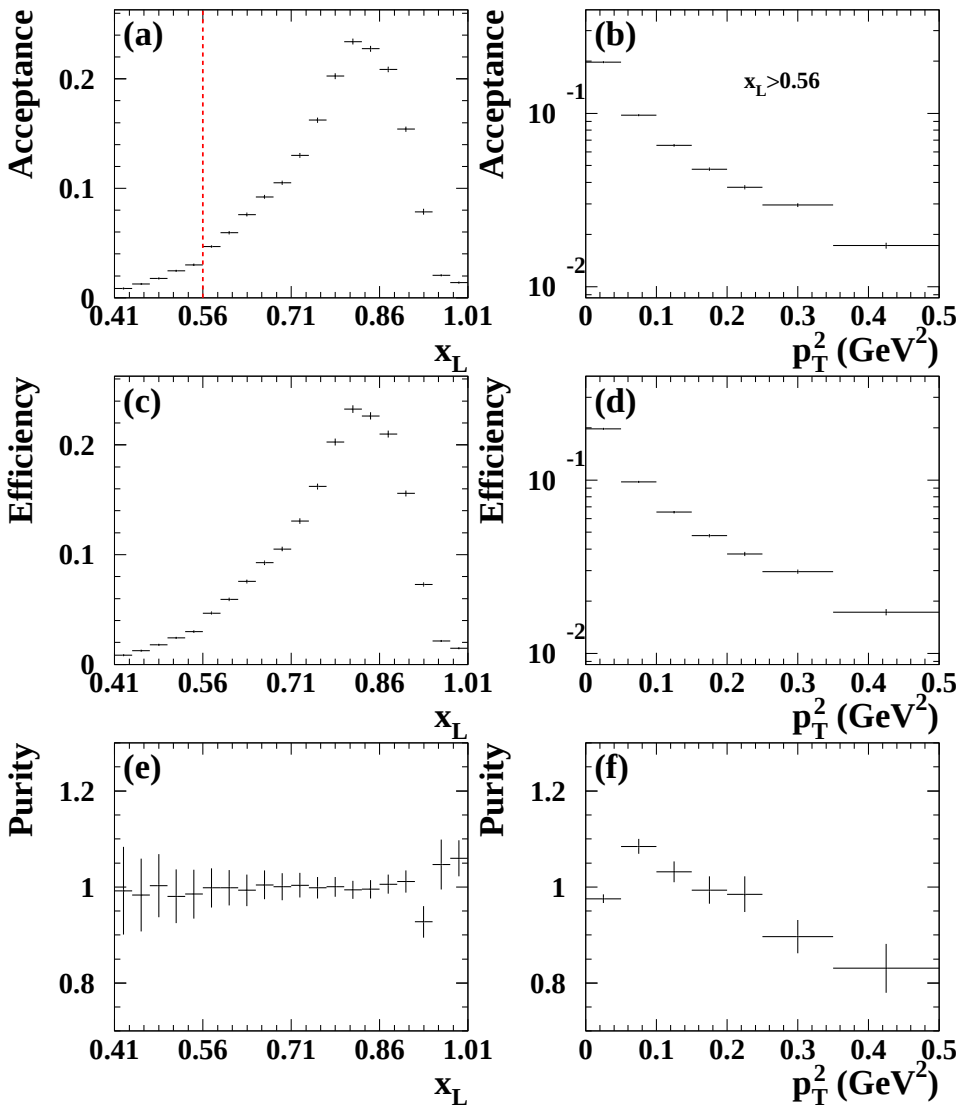

Figure 6.7: *(a) Acceptance as a function of x_L; the dashed line indicates the cut on x_L due to the low acceptance in p_T^2 in the region $x_L < 0.56$; (b) Acceptance as a function of p_T^2 calculated for $x_L > 0.56$; (c) Efficiency as a function of x_L; (d) Efficiency as a function of p_T^2; (e) Purity as a function of x_L; (f) Purity as a function of p_T^2.*

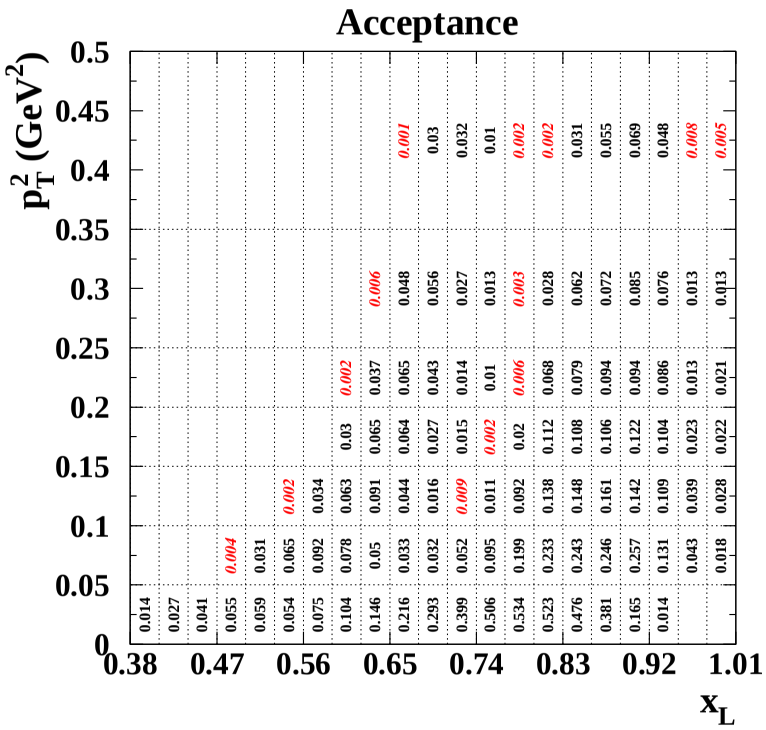

Figure 6.8: *Acceptance values in each x_L and p_T^2 bin of the analysis. The red-italic bins were excluded since the acceptance is $< 1\%$.*

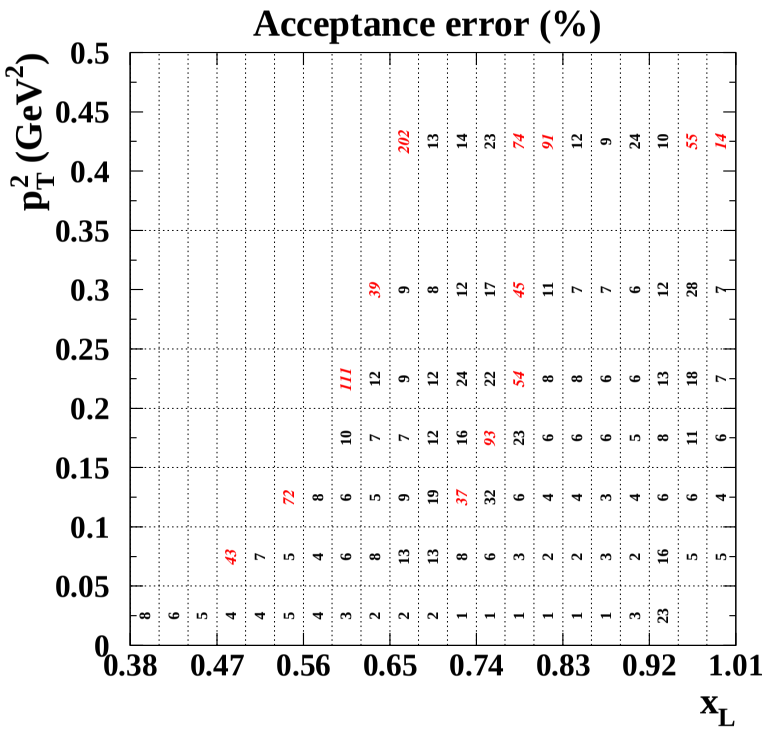

Figure 6.9: *Relative error of the acceptance in each x_L and p_T^2 bin of the analysis. The red-italic bins were excluded since the acceptance is $< 1\%$.*

- the parameter α of the x_L distribution $(1 - x_L)^\alpha$ was set to 0.1;
- the H-box close to the beam-pipe which was excluded, was increased by 0.5 cm in the x and y directions;
- the cut on the scattered-electron energy was varied by ± 2 GeV;
- the $E - p_z$ cut was changed to $35 < E - p_z < 68$ GeV and $41 < E - p_z < 62$;
- the DIS variable y_{JB} was varied to 0.04;
- the vertex cut $|z_{vtx}|$ was changed by ± 10 cm;
- the Δ_{pipe} threshold was varied by ± 0.02 cm and that on Δ_{pot} by ± 0.01 cm;
- the fraction of overlay events to be subtracted from the data was increased and decreased by their statistical uncertainties;
- the fraction of π^+ and K^+ was varied by $\pm 25\%$ as suggested by the maximum value of the statistical error.

Since all the systematic effects are supposed to be uncorrelated, the total systematic errors δ^{up}_{sys} and δ^{low}_{sys} on the measured quantity x^{meas} are calculated as follow:

$$\delta^{up}_{sys} = \sqrt{\sum_i (x^{meas}_i - x^{meas})^2} \qquad \forall x^{meas}_i > x^{meas}, \tag{6.12}$$

$$\delta^{low}_{sys} = \sqrt{\sum_i (x^{meas}_i - x^{meas})^2} \qquad \forall x^{meas}_i < x^{meas}, \tag{6.13}$$

where x^{meas}_i are the quantity measured varying the condition i. In the final plots of each measurement the systematic errors are added in quadrature to the statistical uncertainties.

The sistematic checks list is summarized in table 6.1 and the index number correspond to the x-axis value in the systematic checks plots that are reported in the following sections.

6.4 Measurement of the cross section

The single differential cross section $d\sigma_{ep\to ep'X}/dx_L$ for the semi-inclusive process $ep \to ep'X$ is calculated according to:

$$\frac{d\sigma_{ep\to ep'}}{dx_L} = \frac{N_{data}}{A(x_L)\mathcal{L}} \cdot \frac{1}{\Delta x_L} \tag{6.14}$$

Index	Systematic check
1	Central value
2	b-slope=7.2
3	b-slope=6.4
4	α=0.1
5	H-box +0.5 cm
6	$E_e > 8$ GeV
7	$E_e > 12$ GeV
8	$35 < E - P_z < 68$ GeV
9	$41 < E - P_z < 62$ GeV
10	$y_{JB} > 0.04$
11	$\|z_{vtx}\| < 40$ cm
12	$\|z_{vtx}\| < 60$ cm
13	$\Delta_{pipe} > 0.03$
14	$\Delta_{pipe} > 0.04$
15	$\Delta_{pot} > 0.01$
16	$\Delta_{pot} > 0.03$
17	$\pi^+ - K^+$ corr. +25%
18	$\pi^+ - K^+$ corr. -25%
19	overlay + stat. unc.
20	overlay − stat. unc.

Table 6.1: *Sistematic checks list and index number as reported in the x-axis of the systematic check plots.*

where N_{data} is the number of the events in each x_L bin after the selection cuts, $A(x_L)$ is the acceptance as a function of x_L, Δx_L is the x_L bin width and $\mathcal{L} = 12.8$ pb^{-1} is the luminosity.

The statistical error on the cross section was calculated adding in quadrature the relative errors on the acceptance and on the number of events ($\delta N_{data} = \sqrt{N_{data}}$).

The background corrections, discussed in sections 5.5, 5.6 and 5.7, were applied to the cross section and the effect of the background subtraction is shown in figure 6.10. The contamination from charged mesons mis-interpreted as protons in the LPS affects the low x_L region, while the overlay events contaminate the region at $x_L > 0.9$. The events migrated from the low-Q^2 region are uniformly spread in the whole x_L spectrum. The trigger effect correction (sec. 5.8) was also applied. It is not shown since its effect is very small.

The systematic checks (fig. 6.11) show that the cross section is stable in each x_L bin and the systematic shifts due to the variation of the analysis parameters are within the statistical uncertainty.

In figure 6.12 it is reported the plot of $d\sigma/dx_L$ in the kinematic range

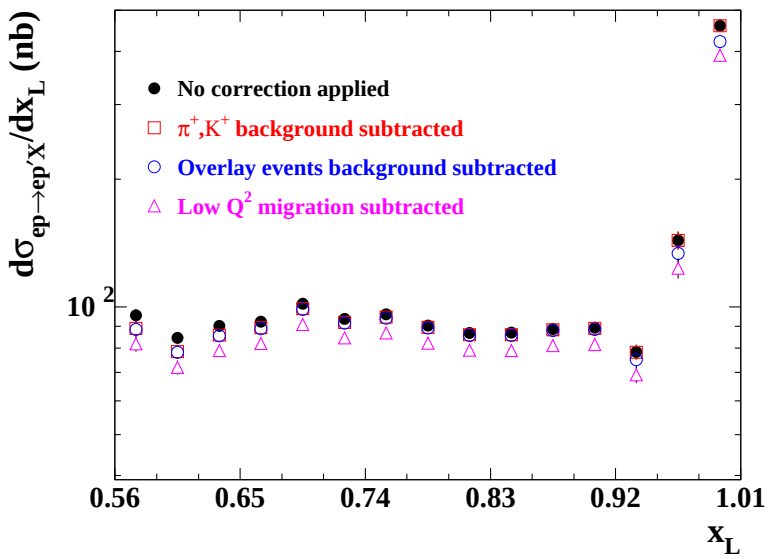

Figure 6.10: *Cross section $d\sigma/dx_L$ before the background correction (black dots) and after applying the background corrections.*

$Q^2 > 3$ GeV^2, $45 < W < 225$ GeV and $p_T^2 < 0.5$ GeV^2. The values of the cross section with the statistical and systematic uncertainties are listed in table A.7. The cross section was fitted to the function $(1 - x_L)^\alpha$ in the range $0.56 < x_L < 0.9$ and it was found the parameter $\alpha = 0.04 \pm 0.01$ with $\chi^2/NoF = 4.6/14$. The cross section is flat up to the diffractive peak where it becomes approximately five times larger. Below the diffractive peak the cross section contains also the proton-dissociative diffractive reaction, in which the proton dissociates and is detected with low longitudinal momentum.

In figure 6.13 the single differential cross section $d\sigma_{ep\to ep'X}/dx_L$ is normalised to the inclusive DIS cross section σ_{tot} and its values with the statistical and systematic uncertainties are listed in table A.8. The ZEUS results obtained with 1995 LPS data are superimposed. The old measurement is systematically 10% higher in the range $x_L < 0.8$ and the discrepancy rises in the diffractive peak at $x_L > 0.98$. However the observed discrepancies are within the experimental uncertainties. The experimental data are compared to the Regge-based model of Szczurek et al. [27]. The agreement with the new measurement is very good. In the range $0.56 < x_L < 0.9$ the leading-proton production is dominated by isoscalar Reggeon exchange. The diffractive processes, due to Pomeron exchange, become increasingly important as x_L approaches unity.

The single differential cross section $d\sigma_{ep\to ep'X}/dp_T^2$ calculation follows the same procedure used for $d\sigma/dx_L$. The cross section is computed from:

$$\frac{d\sigma_{ep\to ep'}}{dp_T^2} = \frac{N_{data}}{A(p_T^2)\mathcal{L}} \cdot \frac{1}{\Delta p_T^2} \tag{6.15}$$

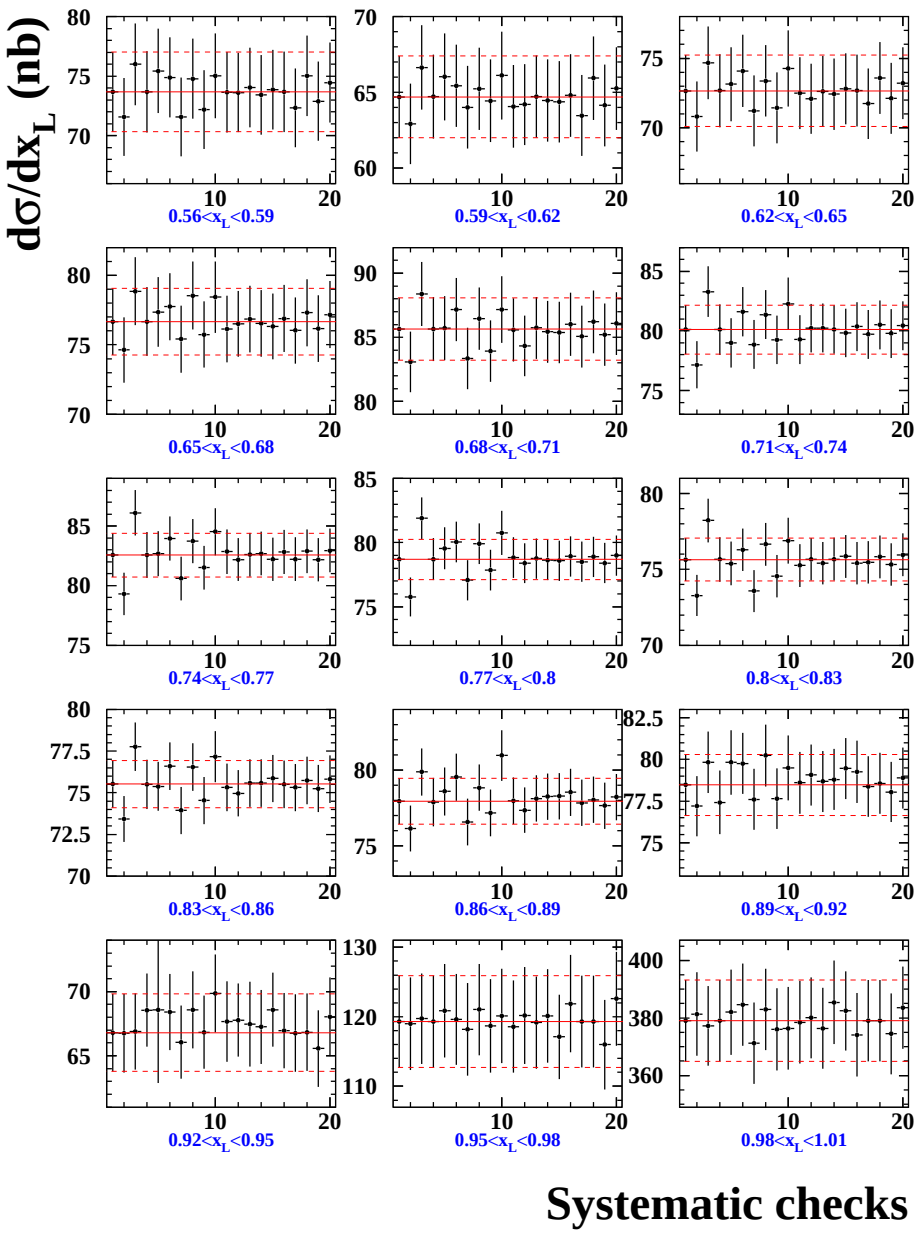

Figure 6.11: *Systematic checks for each x_L bin. The x-axis values correspond to the systematic indexes reported in table 6.1. The red line on each plot is drawn on the central value and the red-dashed lines are the associated statistical errors. The bars on each dot represent the statistical uncertainty of each measurement.*

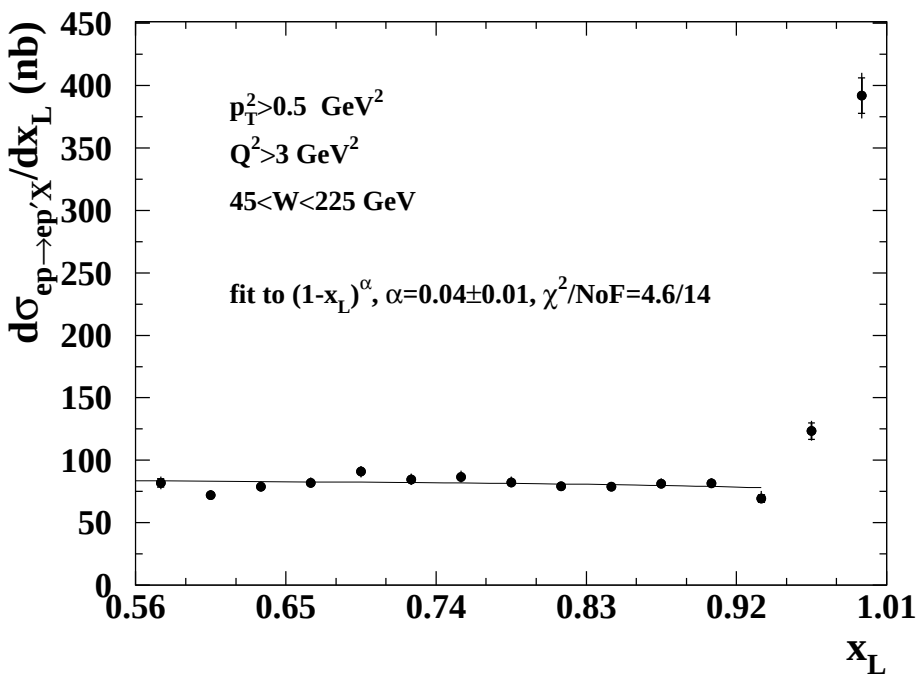

Figure 6.12: *Single differential cross section $d\sigma_{ep\to ep'X}/dx_L$ measured in the kinematic range $p_T^2 < 0.5\ GeV^2$, $Q^2 > 3\ GeV^2$ and $45 < W < 225\ GeV$. The inner bars show the statistical uncertainties and the outer bars the statistical and systematic uncertainties added in quadrature.*

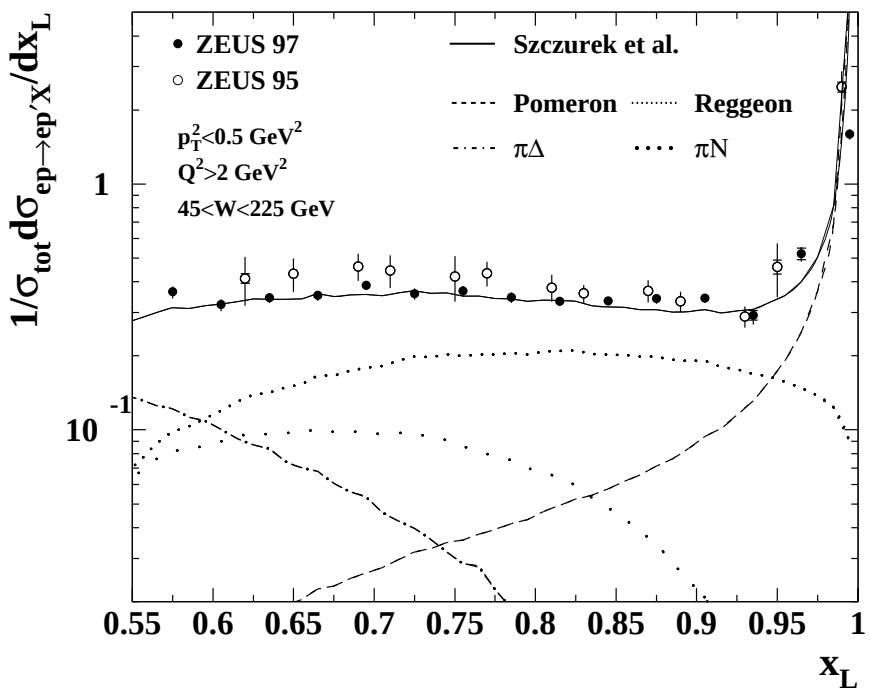

Figure 6.13: *Single differential cross section normalised to the total DIS cross section* $1/\sigma_{tot} \cdot d\sigma_{ep\to ep'X}/dx_L$ *measured in the kinematic range* $p_T^2 < 0.5$ GeV^2, $Q^2 > 3$ GeV^2 *and* $45 < W < 225$ GeV. *The black dots are the results of this analysis and the circles are the ZEUS results obtained with 1995 LPS data. The inner bars show the statistical errors and the outer bars the systematic and statistical uncertainties added in quadrature. The data are compared to the model of Szczurek et al. [27]. The solid curve is the sum of Pomeron, Reggeon and pion exchanges contributions, indicated in the figure.*

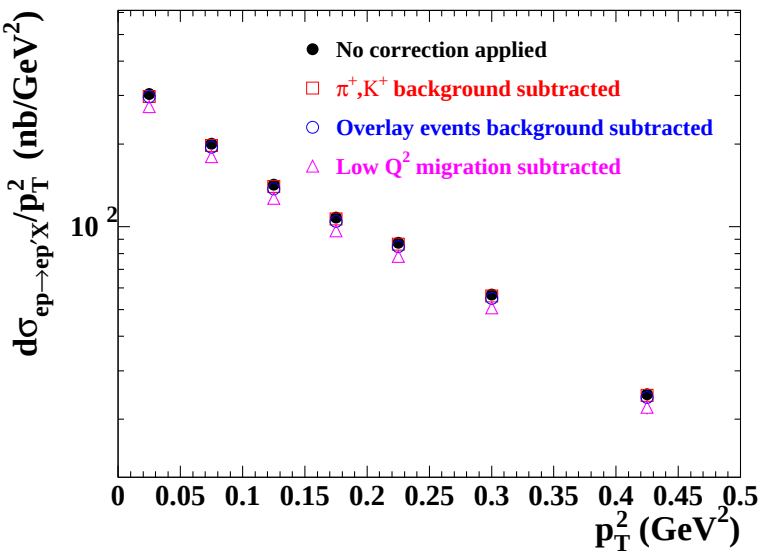

Figure 6.14: *Cross section $d\sigma/dp_T^2$ before the background correction (black dots) and after applying the background corrections.*

where N_{data} is the number of the events in each p_T^2 bin after the selection cuts, $A(p_T^2)$ is the acceptance as a function of p_T^2 and Δp_T^2 is the bin width.

In figure 6.14 are shown the effects of the background subtraction. The background corrections do not depend on p_T^2 and then the subtraction of each contribution result to be constant over the whole p_T^2 spectrum.

The systematic checks (fig. 6.15) evidence a strong dependence of the transverse momentum cross section on the variation of the reweighting parameter α, particularly for $p_T^2 < 0.15$ GeV^2. This effect comes from the fact that the Monte Carlo was reweighted to the function $f(x_L, p_T^2) \propto (1 - x_L)^\alpha \exp(-b \cdot p_T^2)$ that rises at lower x_L values when $\alpha \neq 0$. The low x_L acceptance range corresponds to the low p_T^2 region, and hence the cross section is observed to rise up in that range. In the other cases the cross section is stable within the statistical uncertainty.

The final plot of p_T^2 is shown in figure 6.16 and the cross section values with the statistical and systematic uncertainties are listed in table A.9. In the kinematic range $Q^2 > 3$ GeV^2, $45 < W < 225$ GeV and $x_L > 0.56$ the cross section exhibits an exponential behaviour. The line in the plot is drawn to guide the eye and the slope of the exponential function is the same used in the reweighting function.

The double differential cross section $d^2\sigma_{ep\to ep'X}/dx_L dp_T^2$ was measured as a function of p_T^2 in bins of x_L. The p_T^2 range in each of the x_L bins of the measurement is dictated by the acceptance of the LPS. In figure 6.17 the differential cross sections were plotted after applying the background corrections. In each x_L bin, the cross section was fitted to the exponential

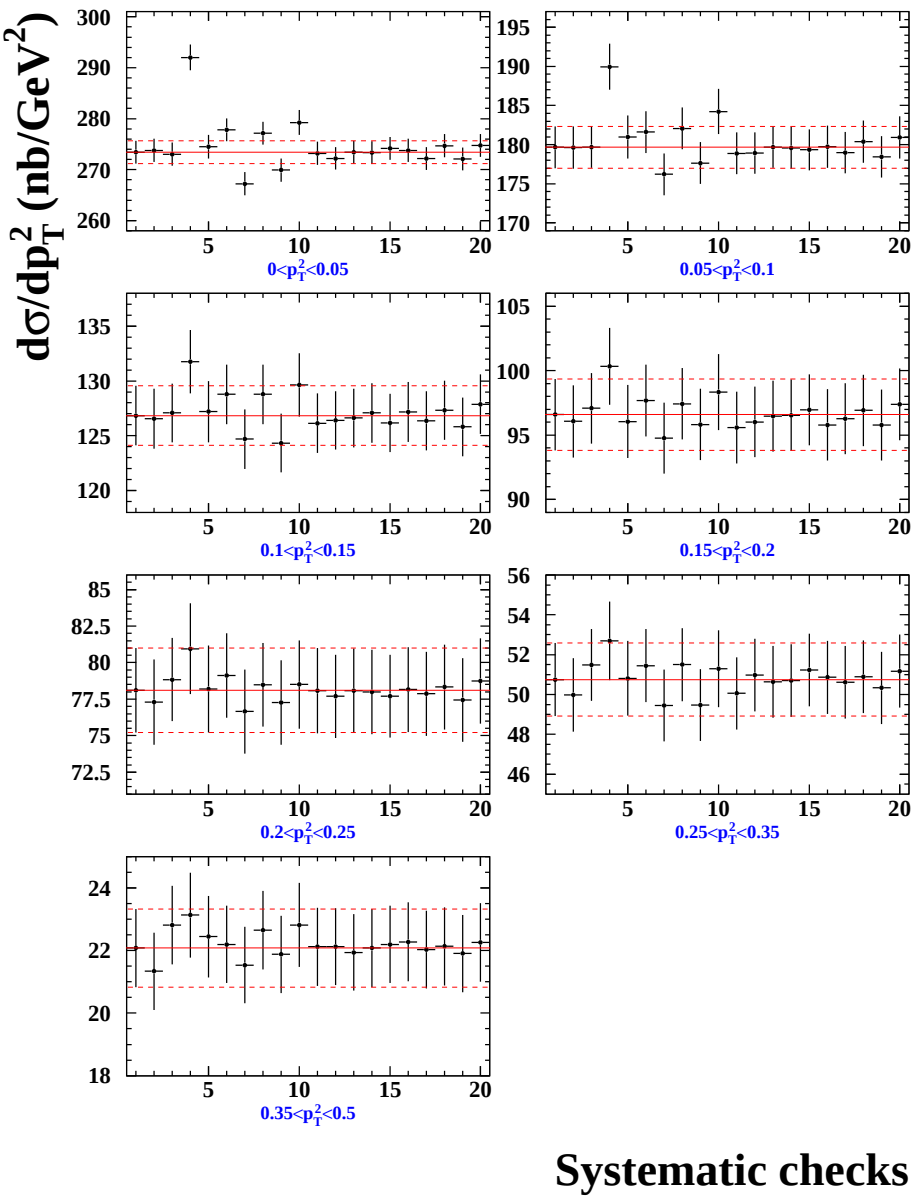

Figure 6.15: *Systematic checks for each p_T^2 bin. The x-axis values correspond to the systematic indexes reported in table 6.1. The red line on each plot is drawn on the central value and the red-dashed lines are the associated statistical errors. The bars on each dot represent the statistical uncertainty of each measurement.*

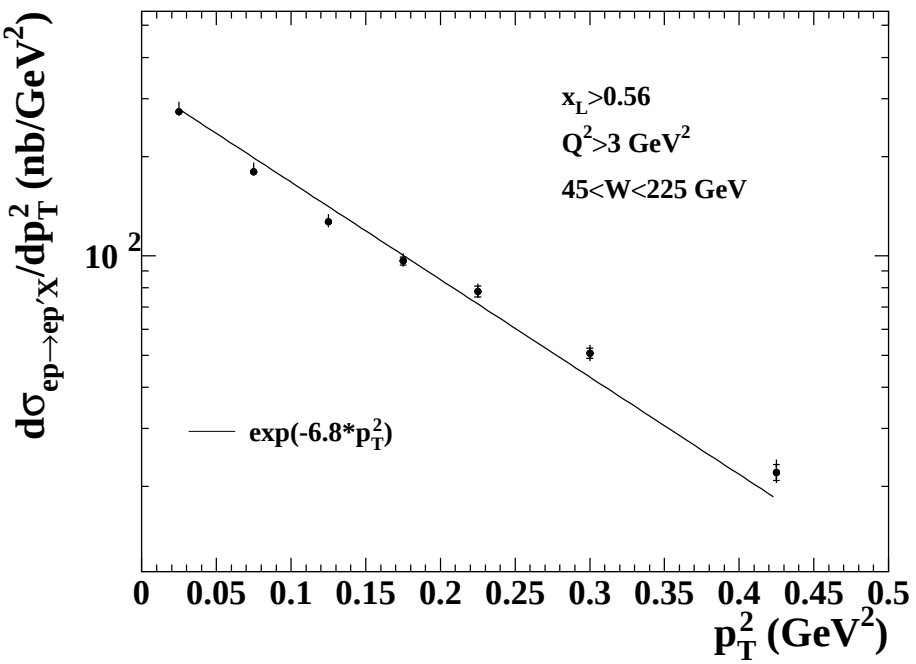

Figure 6.16: *Single differential cross section $d\sigma_{ep\to ep'X}/dp_T^2$ measured in the kinematic range $x_L > 0.56$ GeV^2, $Q^2 > 3$ GeV^2 and $45 < W < 225$ GeV. The inner bars show the statistical uncertainties and the outer bars the statistical and systematic uncertainties added in quadrature. The exponential function is drawn to guide the eye.*

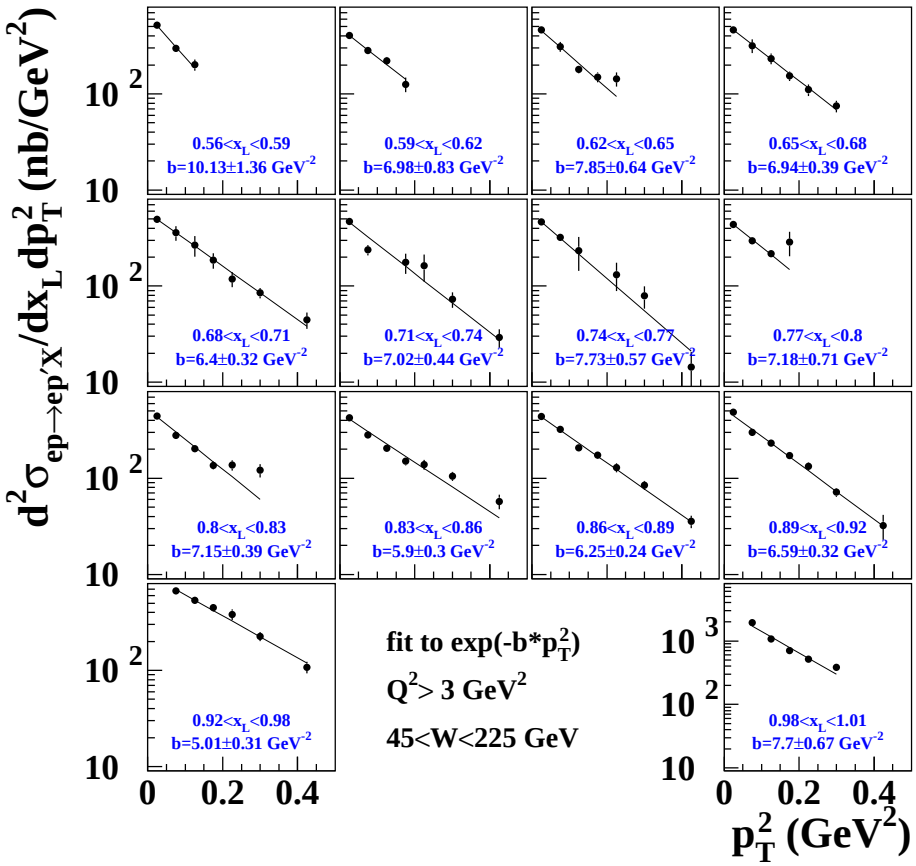

Figure 6.17: *Double differential cross section $d^2\sigma_{ep\to ep'X}/dx_L dp_T^2$ measured in the kinematic range $Q^2 > 3$ GeV^2 and $45 < W < 225$ GeV plotted as a function of p_T^2 in bins of x_L. The vertical bars are the statistical errors. The lines are the result of the fit to the function $A \cdot exp(-b \cdot p_T^2)$ and the fit results and the associated statistical errors are reported.*

function $A \cdot \exp(-b \cdot p_T^2)$ and the b-slopes were reported with their errors. The fit was performed on the mean values $\langle p_T^2 \rangle$ of each p_T^2 bin. Since in the bin $0.95 < x_L < 0.98$ the statistics is low, the bin was merged to the previous one.

The fit was repeated as systematic check and the effect of the systematic variations is shown in figure 6.18. The statistical error resulting from the fit is dominant on the systematic uncertainty.

The b-slopes were plotted as a function of x_L in the measurement range $x_L > 0.56$ and are shown in figure 6.19. The values of the b-slopes are listed in table A.10 together with the statistical and systematic errors. In the same plot the b-slopes measured by ZEUS using the 1995 LPS data (black squares) were superimposed and the two measurements are found to be consistent.

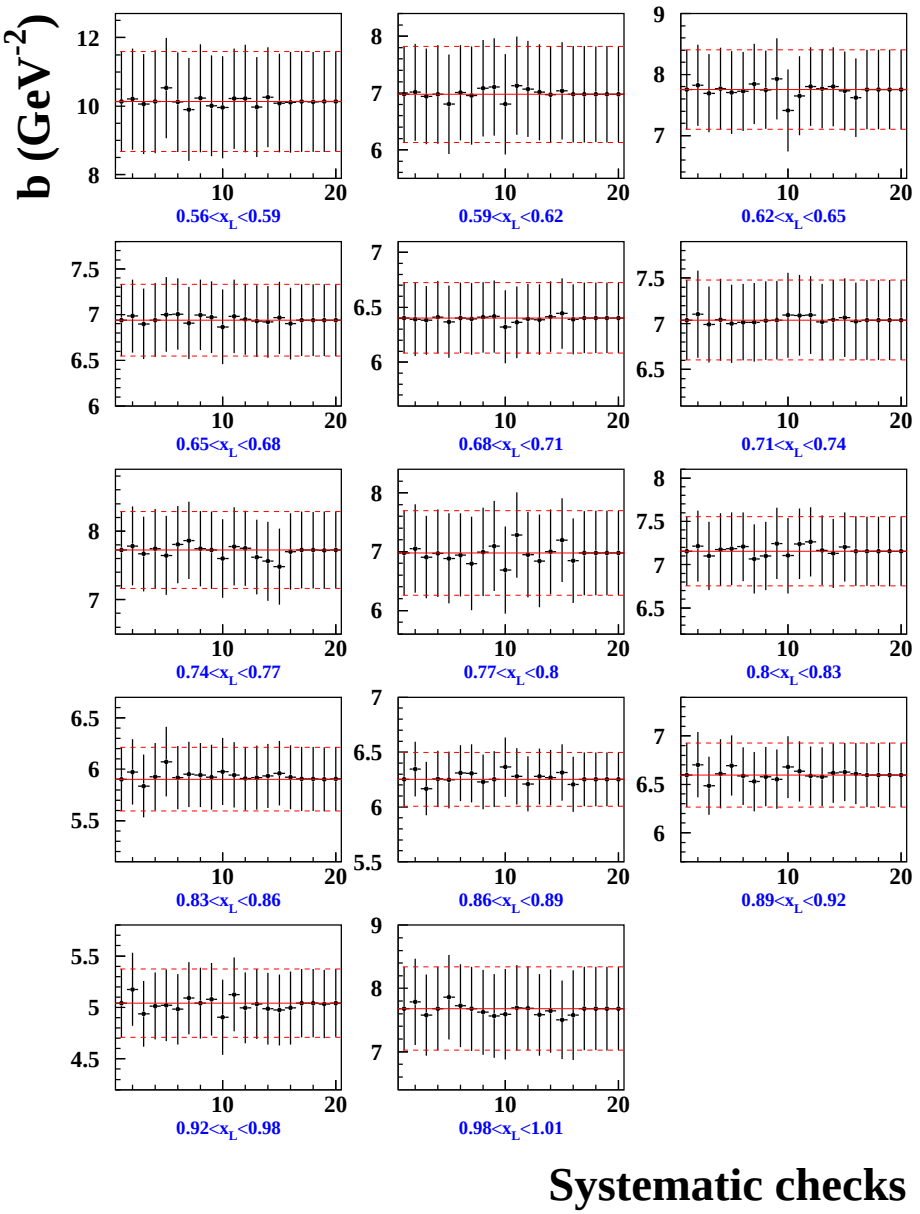

Figure 6.18: *Systematic checks of the b-slope measurement for each x_L bin. The x-axis values correspond to the systematic indexes reported in table 6.1. The red line on each plot is drawn on the central value and the red-dashed lines are the associated statistical errors. The bars on each dot represent the statistical uncertainty of each measurement.*

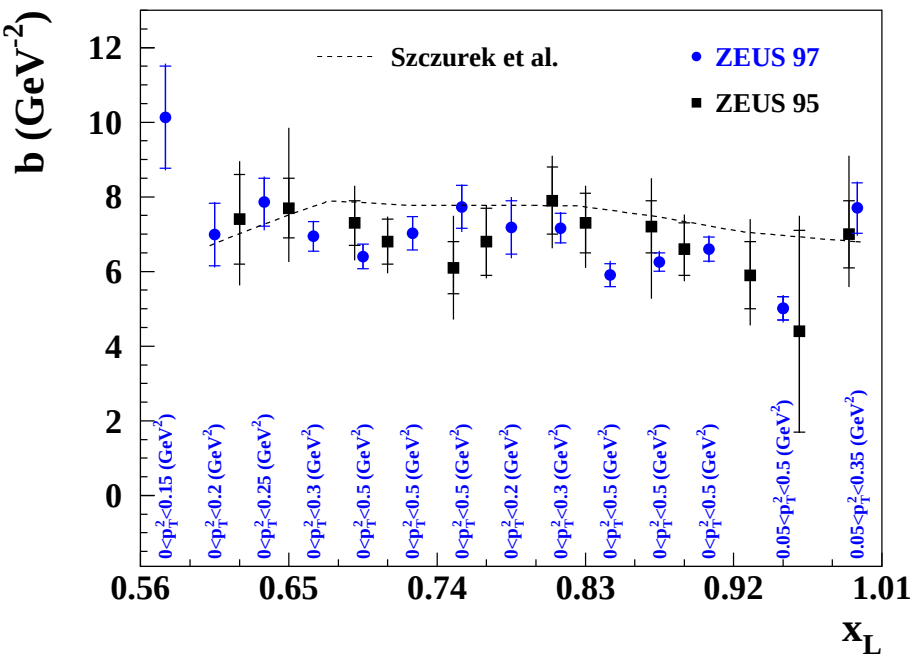

Figure 6.19: *b-slope of the cross section* $d\sigma_{ep\to ep'X}/dp_T^2$ *as obtained by the fit to the function* $A \cdot exp(-b \cdot p_T^2)$ *in bins of* x_L*. The blue full circles are the present measurements and the black squares are the published ZEUS data. The inner bars show the statistical uncertainties and the outer bars the statistical and systematic uncertainties added in quadrature. The range of* p_T^2 *used in each* x_L *bin is reported at the bottom of the measurement. The dashed curve is the prediction of the Reggeon exchange model of Szczurek et al. [27].*

The predictions of the model of Szczurek et al. [27] are also shown and they are in reasonable agreement with the transverse momentum data. The observed fluctuations of the b-slopes are related to the p_T^2 ranges in which the cross section was fitted (the p_T^2 ranges were reported in the figure). The mean slope is $\langle b \rangle \approx 6.9$ GeV^{-2} and no evidence of a strong dependence of the b-slope on x_L is observed.

6.5 Leading-proton production rate to the inclusive DIS

The relationship between the leading-proton production and the inclusive e^+p scattering was studied in terms of the ratio of the cross sections. The leading-proton cross section can be expressed in terms of leading-proton structure function:

$$\frac{d^4\sigma^{LP}}{dxdQ^2dx_Ldp_T^2} = \frac{4\pi\alpha^2}{xQ^4}\left(1-y+\frac{y^2}{2}\right)F_2^{LP(4)}(x,Q^2,x_L,p_T^2)(1+\Delta_{LP}). \tag{6.16}$$

were Δ_{LP} takes into account the effect of the longitudinal structure function F_L and the violating parity terms arising from the Z^0 exchange contribution (eq. 1.9). The integration over the measured x_L and p_T^2 ranges gives

$$\bar{F}_2^{LP(2)}(x,Q^2) = \int_0^{p_T^{2max}} dp_T^2 \int_{x_L^{min}}^{x_L^{max}} dx_L F_2^{LP(4)}(x,Q^2,x_L,p_T^2), \tag{6.17}$$

and the ratio $r^{LP(2)}$ is then defined as

$$r^{LP(2)}(x,Q^2) = \frac{\bar{F}_2^{LP(2)}(x,Q^2)}{F_2(x,Q^2)}, \tag{6.18}$$

where $F_2(x,Q^2)$ is the inclusive DIS structure function (eq. 1.9). The ratio $r^{LP(2)}(x,Q^2)$ is measured in a given bin of x and Q^2. In this fraction the acceptance corrections related to the DIS selection procedure cancel and the ratio $r^{LP(2)}$ yields:

$$r^{LP(2)}(x,Q^2) = \frac{N^{LPS}(x,Q^2)}{N^{DIS}(x,Q^2)}\frac{\mathcal{L}^{DIS}}{\mathcal{L}^{LPS}}\frac{1}{\epsilon_{LPS}}, \tag{6.19}$$

where $N^{LPS}(x,Q^2)$ is the number of events with a leading-proton in the x, Q^2 bin, $N^{DIS}(x,Q^2)$ is the number of DIS event in that bin after the DIS selection cuts. $\mathcal{L}^{DIS} = 938.85$ nb^{-1} and $\mathcal{L}^{LPS} = 12.8$ pb^{-1} are the DIS and LPS luminosities, respectively. The quantity ϵ_{LPS} is the LPS acceptance, obtained by applying only the LPS selection. In the range $0.56 < x_L < 0.98$ and $p_T^2 < 0.5$ GeV^2 , ϵ_{LPS} is approximately 19%.

The ratio $r^{LP(3)}(x,Q^2,x_L)$ is defined in analogy to $r^{LP(2)}(x,Q^2)$:

$$r^{LP(3)}(x,Q^2,x_L) = \frac{N^{LPS}(x,Q^2,x_L)}{N^{DIS}(x,Q^2)}\frac{\mathcal{L}^{DIS}}{\mathcal{L}^{LPS}}\frac{1}{\epsilon_{LPS}(x_L)\Delta x_L}, \tag{6.20}$$

where Δx_L indicate the size of the x_L bins. In analogy with the equation 6.18 the ratio $r^{LP(3)}$ can be expressed in terms of structure functions:

$$r^{LP(3)(x,Q^2,x_L)} = \frac{\bar{F}_2^{LP(3)}(x,Q^2,x_L)}{F_2(x,Q^2)}, \tag{6.21}$$

where $\bar{F}_2^{LP(3)}(x,Q^2,x_L)$ is obtained by the integration over p_T^2 only.

The ratio $r^{LP(3)}$ as a function of x_L in bins of x and Q^2 is shown in figures 6.20 and 6.21 in the kinematic range $p_T^2 < 0.5$ GeV^2 and $45 < W < 225$ GeV. The values of $r^{LP(3)}$ with the statistical and systematic uncertainties are reported in tables A.11− A.17. The measurements of $r^{LP(3)}$ with 1995 data are also reported in figure 6.22. The dashed lines at $r^{LP(3)} = 0.4$ are overlaid to guide the eye. In the new results presented in this analysis, the measurement range was extended to $x = 8.5 \cdot 10^{-5}$ and $Q^2 = 377$ GeV^2. Also the x_L range was extended down to $x_L = 0.56$. The $r^{LP(3)}$ values are approximately constant over the kinematic range.

In figure 6.23 it is shown the ratio $r^{LP(2)}$ as a function of x for fixed Q^2 values, for $45 < W < 225$ GeV and for leading protons in the range $0.56 < x_L < 0.98$ and $p_T^2 < 0.5$ GeV^2. The horizontal dashed lines at $r^{LP(2)} = 0.1$ and $r^{LP(2)} = 0.15$ are drawn to guide the eye. The values of $r^{LP(2)}$ with the statistical and systematic uncertainties are reported in tables A.18− A.19. The ratio $r^{LP(2)}$ is observed to be approximately constant along x. The ratio $\langle r^{LP(2)} \rangle$ averaged on x as a function of Q^2 is shown in figure 6.24 for $0.56 < x_L < 0.98$ and its values are listed in table A.20. The leading-proton yield increases from $\langle r^{LP(2)} \rangle \approx 0.14$ at $Q^2 = 3.4$ GeV^2 to $\langle r^{LP(2)} \rangle \approx 0.17$ at $Q^2 = 22$ GeV^2 and then goes down to $\langle r^{LP(2)} \rangle \approx 0.155$ at higher Q^2 values. The decrease of $\langle r^{LP(2)} \rangle$ at low Q^2 values can be interpreted in terms of rescattering of the leading-proton on the virtual photon. In fact at low Q^2 values the photon radiated at the lepton vertex has low virtuality and it can fluctuate in a $q - \bar{q}$ state and hence the leading-proton can interact with the quarks inside the photon. The rescattered proton is not detected and the measured cross section (and, as consequence, the ratio $\langle r^{LP(2)} \rangle$) is expected to decrease at low Q^2 values.

In figure 6.25 the average ratio $\langle r^{LP(2)} \rangle$ was measured in the range $0.62 < x_L < 0.98$ and compared to the measurement obtained with 1995 data. The same behaviour is observed in the overlapping region.

The data in figure 6.23 are also presented in figure 6.26 in terms of the proton-tagged structure function $\bar{F}_2^{LP(2)}$, obtained by multiplying $r^{LP(2)}$ by F_2. For the parametrisation of F_2, the ZEUS-S fit NLO [18] was used. $\bar{F}_2^{LP(2)}$ is plotted as a function of x at fixed Q^2 values. The bands in the plots show the one-standard-deviation limits of F_2, scaled by the average value of $r^{LP(2)}$ ($\langle r^{LP(2)} \rangle \simeq 0.164$). The value of $\bar{F}_2^{LP(2)}$ are listed in tables A.21 and A.22. Since $r^{LP(2)}$ is approximately independent of x and Q^2, $\bar{F}_2^{LP(2)}$ is found to be approximately proportional to F_2, and the proportionality factor between $\bar{F}_2^{LP(2)}$ and F_2 results to be $\langle r^{LP(2)} \rangle \simeq 0.164$.

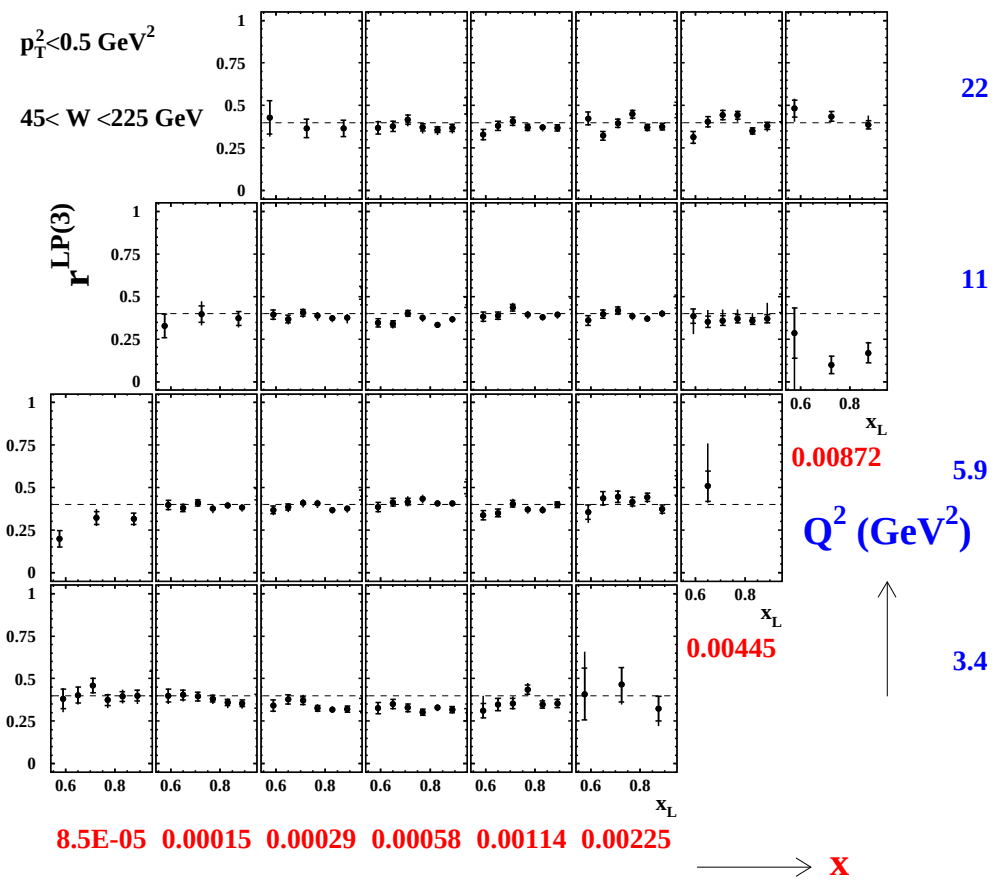

Figure 6.20: *The ratio $r^{LP(3)}$ as a function of x_L in bins of x and Q^2, for protons having $p_T^2 < 0.5$. The inner bars show the statistical uncertainties and the outer bars the statistical and systematic uncertainties added in quadrature. The dashed line at $r^{LP(3)} = 0.4$ is overlaid to guide the eye.*

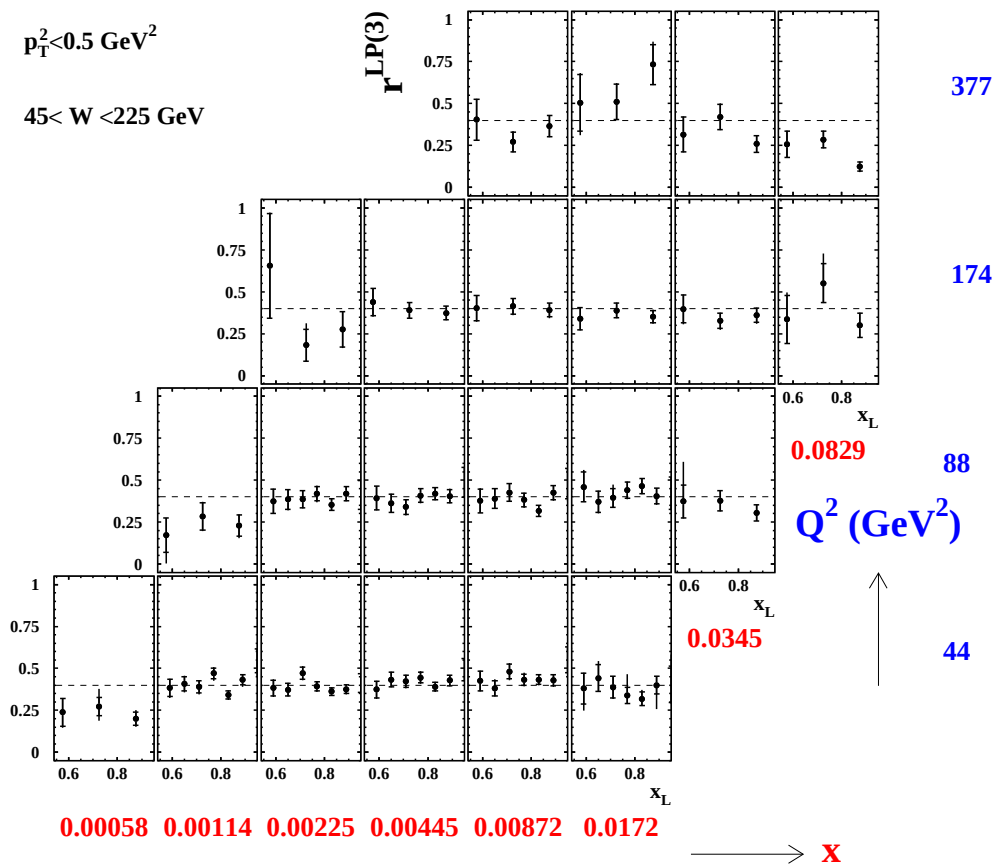

Figure 6.21: *The ratio $r^{LP(3)}$ as a function of x_L in bins of x and Q^2, for protons having $p_T^2 < 0.5$. The inner bars show the statistical uncertainties and the outer bars the statistical and systematic uncertainties added in quadrature. The dashed line at $r^{LP(3)} = 0.4$ is overlaid to guide the eye.*

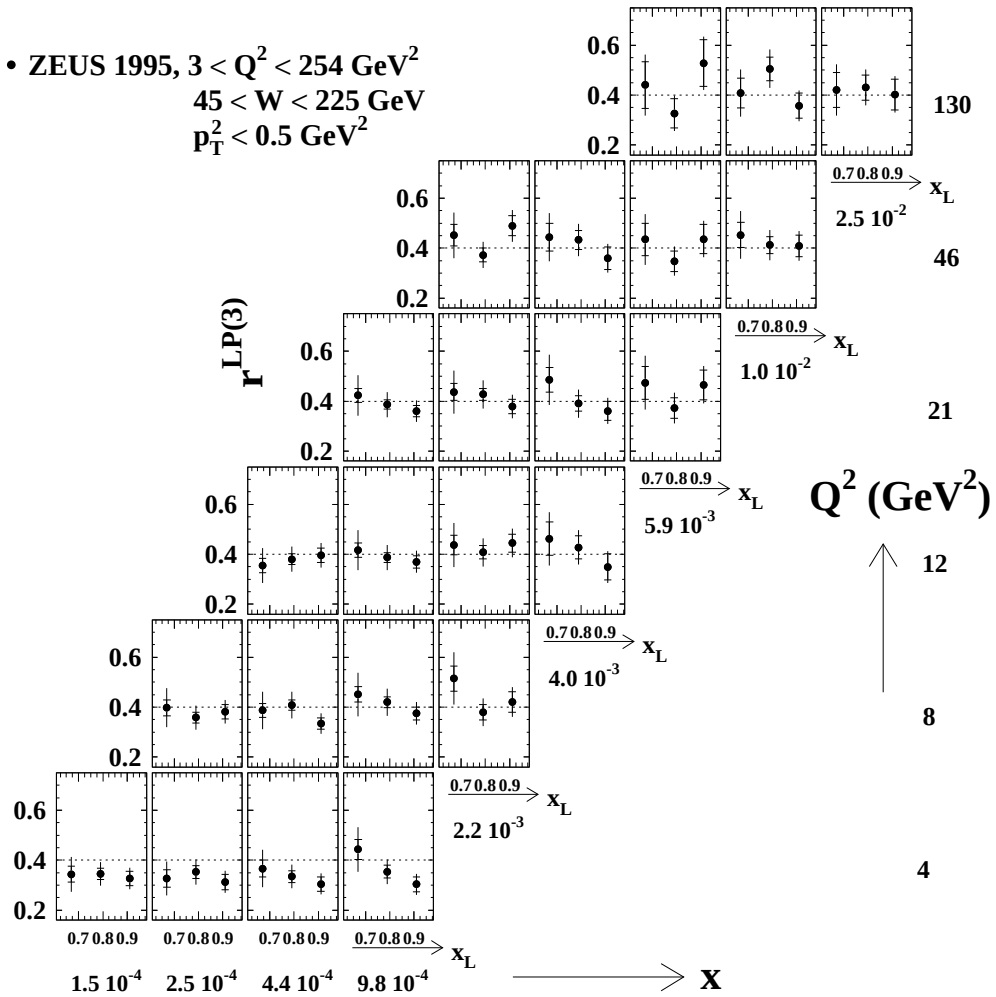

Figure 6.22: *The ratio $r^{LP(3)}$ as a function of x_L in bins of x and Q^2, for protons having $p_T^2 < 0.5$ measured with 1995 ZEUS data. The inner bars show the statistical uncertainties and the outer bars the statistical and systematic uncertainties added in quadrature. The dashed line at $r^{LP(3)} = 0.4$ is overlaid to guide the eye.*

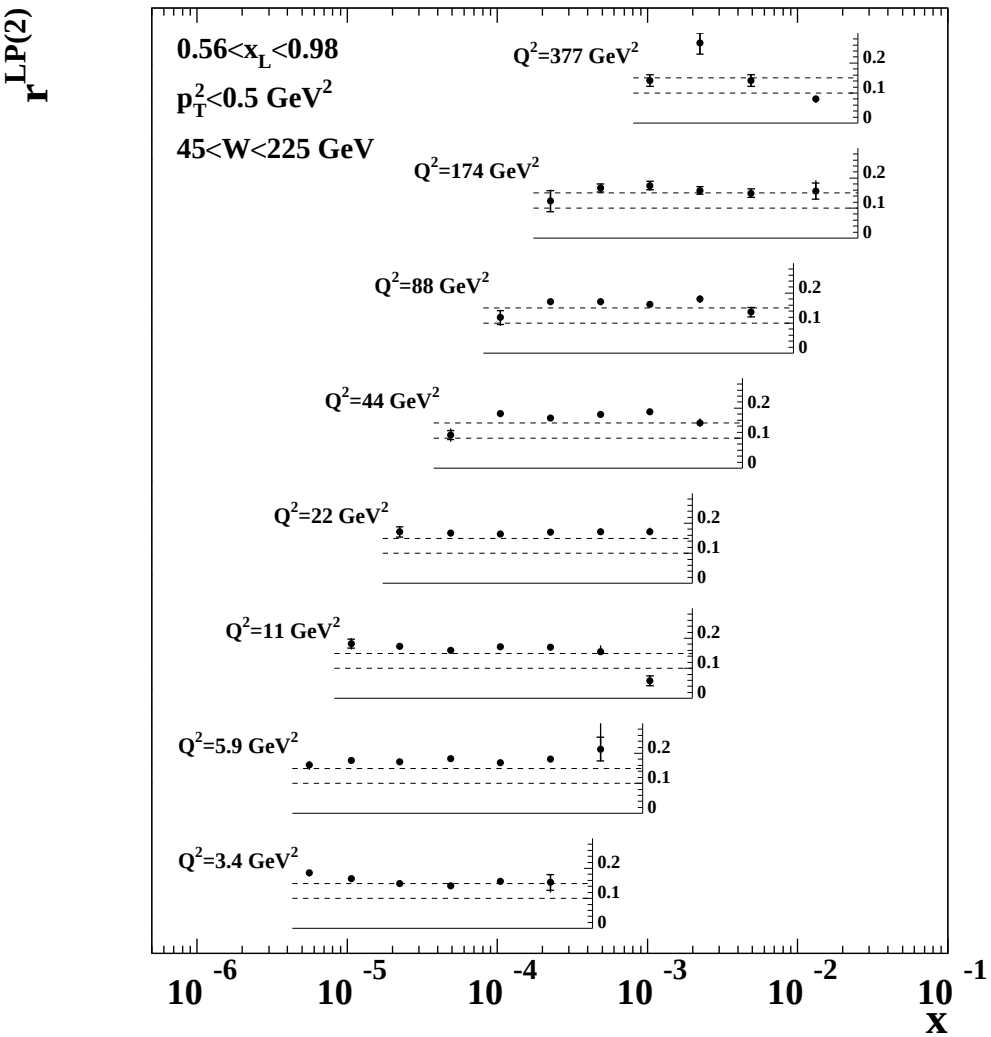

Figure 6.23: *The ratio $r^{LP(2)}$ as a function of x for fixed Q^2 values, for protons having $p_T^2 < 0.5$ and $0.56 < x_L < 0.98$. The inner bars show the statistical uncertainties and the outer bars the statistical and systematic uncertainties added in quadrature. The horizontal dashed lines at $r^{LP(2)} = 0.10$ and $r^{LP(2)} = 0.15$ are overlaid to guide the eye.*

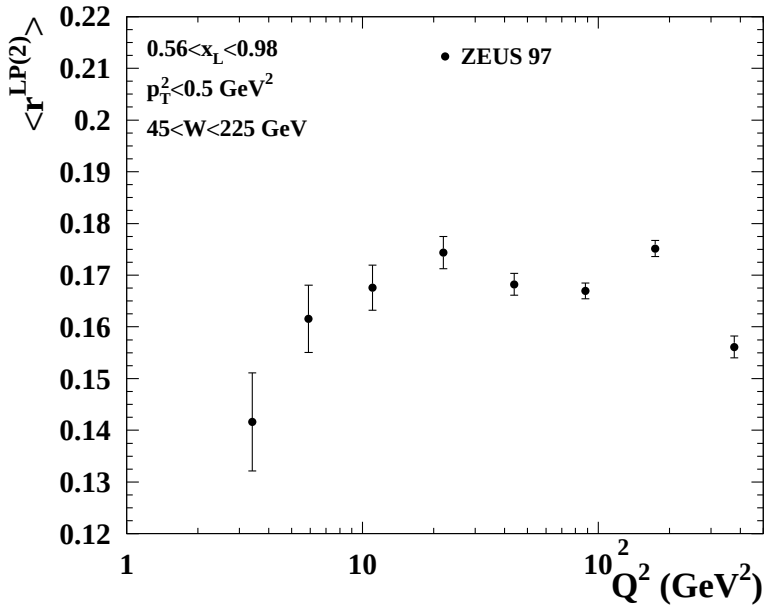

Figure 6.24: *The average ratio* $\langle r^{LP(2)} \rangle$ *as a function of* Q^2 *for protons having* $p_T^2 < 0.5$ *and* $0.56 < x_L < 0.98$. *The error bars show the statistical uncertainties.*

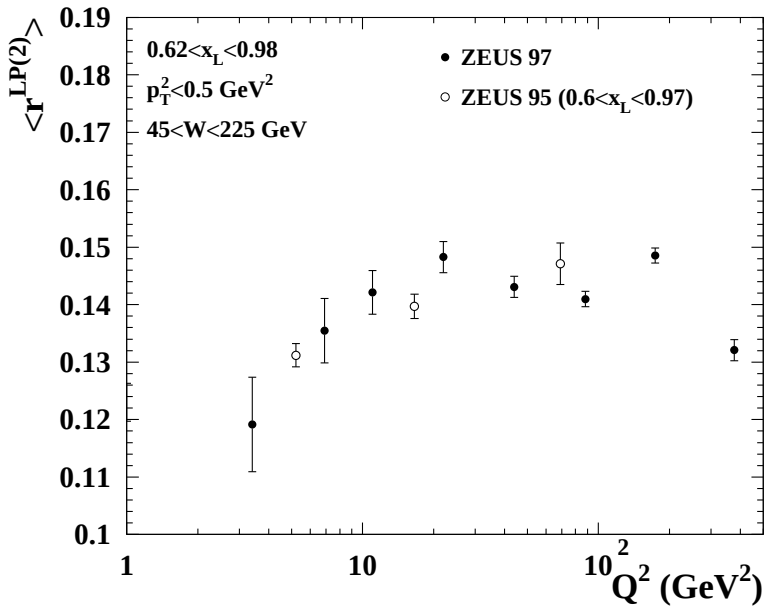

Figure 6.25: *The average ratio* $\langle r^{LP(2)} \rangle$ *as a function of* Q^2. *The black dots are the results of this analysis for protons having* $p_T^2 < 0.5$ *and* $0.62 < x_L < 0.98$ *and the circles are the published results for protons having* $p_T^2 < 0.5$ *and* $0.6 < x_L < 0.97$. *The error bars show the statistical uncertainties.*

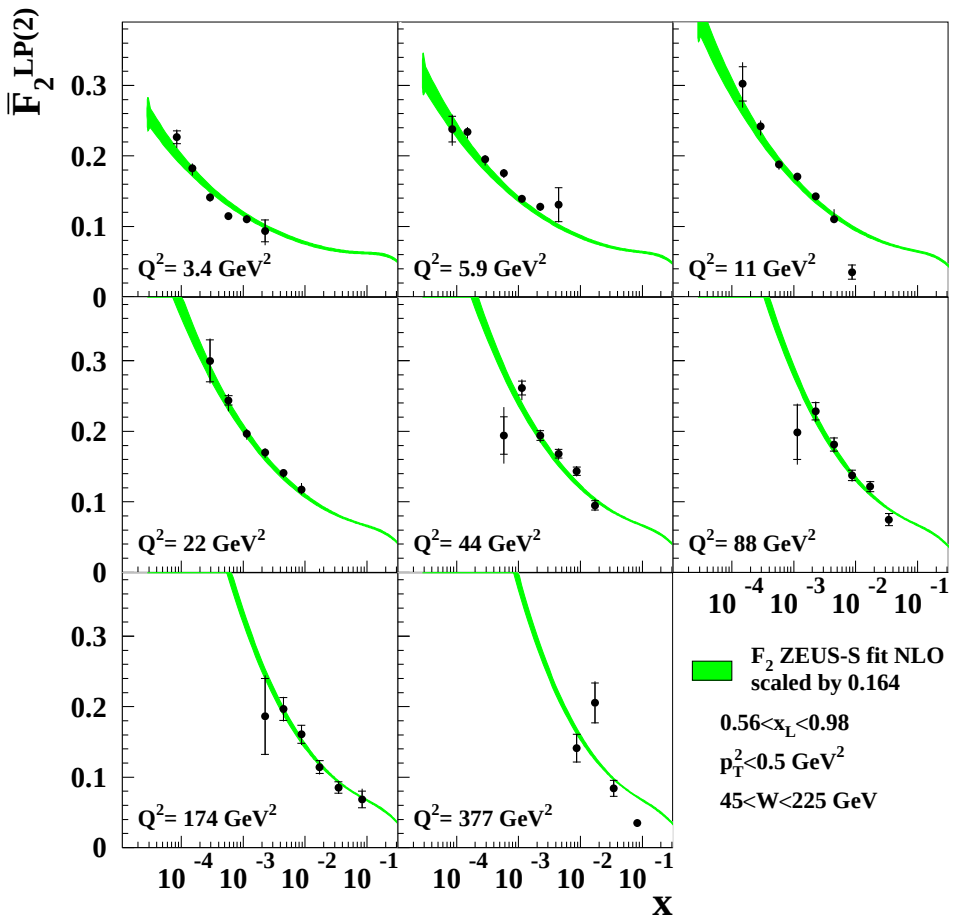

Figure 6.26: *The tagged-proton structure function* $\bar{F}_2^{LP(2)}$ *as a function of* x *for fixed* Q^2 *values, for protons having* $p_T^2 < 0.5$ *and* $0.62 < x_L < 0.98$. *The bands show the one-standard-deviation limits of the* F_2 *ZEUS-S fit NLO parametrisation, scaled by the average value* $\langle r^{LP(2)} \rangle = 0.164$. *The inner bars show the statistical uncertainties and the outer bars the statistical and systematic uncertainties added in quadrature.*

Chapter 7

Preliminary results with LPS s123

The Leading Proton Spectrometer is composed of six stations (s1 → s6), but it can be considered as a pair of two independent spectrometers (s123 and s456), due to the different acceptance regions (there is only a limited overlapping acceptance region).

Since the stations s123 are the nearest to the interaction point, they are more sensitive to the proton kinematic and a small mis-calibration or mis-alignement of the stations and of the magnets could affect considerably the acceptance of the spectrometer. For this reason these stations have not been commissioned for a long time and up to now they have never been used for physics analyses.

Studies with real and simulated data led to suspect that the desing shape of some of the stations, the one implemented in the Monte Carlo simulation, did not correspond to that of the actual detectors.

After the LPS stations were removed from the experiment, they were re-measured on a probe station and significative differences were indeed found with respect to the original design. A new geometry was therefore implemented in the MOLPS simulation package, based on these measurements, and corresponding modifications were implemented in the reconstruction program - both for the simulated and the real data.

Even if the shapes of the leading proton distributions now are quite well reproduced by the MC, the relative number of simulated events reconstructed in the stations s123 is found to be in excess with respect to the spectrometer s456. This is likely due to inaccurancies in the simulation of the position of the stations during part of the data-taking periods, a subject now under study. In the meantime we were able to identify a sub-set of the data sample much better reproduced by the Monte Carlo. We measured the leading proton cross sections using this data sub-sample, and they were compared to the results obtained with the spectrometer s456.

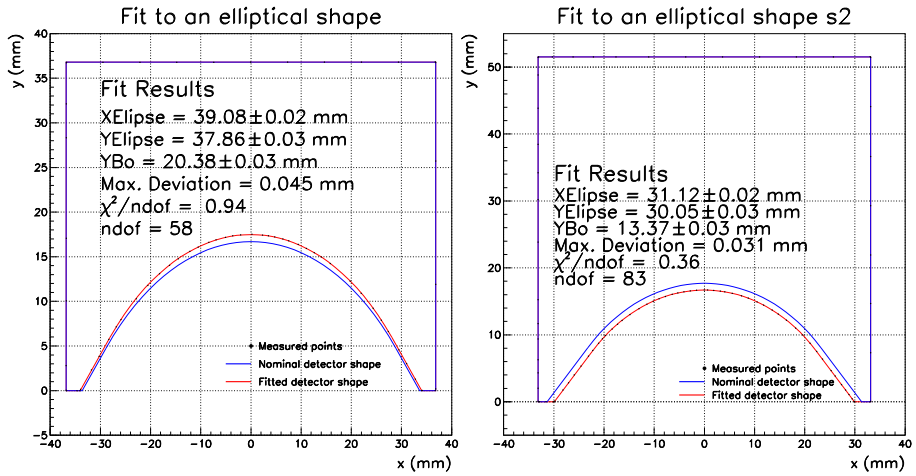

Figure 7.1: *Schematic plot of the measurement of the station s1 (left) and s2 (right) on probe station. The fit parameters and the measured (red line) and design (blue line) shapes are shown.*

7.1 New Geometry implementation

The results of the measurement of the LPS stations s1 and s2 on the probe station are reported in figure 7.1. The internal border of the stations s1 and s2 was measured and fitted to an elliptical shape and differences of the order of 1 mm were found with respect to the design shape. The actual shape were then implemented in the MOLPS reconstruction package. In figure 7.2 are shown the $x - y$ hit distributions on the LPS station s1 in the coincidence s1*s2*s3; the green circles are the simulated hits and the black ones are the data. In the left plot the original geometry was used and a large excess of acceptance is observed near the internal border of the station. After implementing the new geometry, with the measured shape, the hit distributions of the MC fits the data very well (right plot).

7.1.1 Data-MC comparisons

After implementing the new geometry, the MC distributions of the leading proton variables reconstructed in the LPS were compared to the data. The selection procedures and the reweighting of the Monte Carlo events are the same as adopted in the analysis of the s456 data sample (sections 5.2 and 5.3).

In figure 7.3 are shown the x_L distributions for each coincidence (two stations and triple coincidence). In each plot the MC distribution was normalised to the number of the data and a reasonable agreement is observed. In figure 7.4 the p_T^2 distributions for each coincidence are reported. The MC reproduces quite well the data in the range $p_T^2 < 0.3$ GeV^2 but an excess

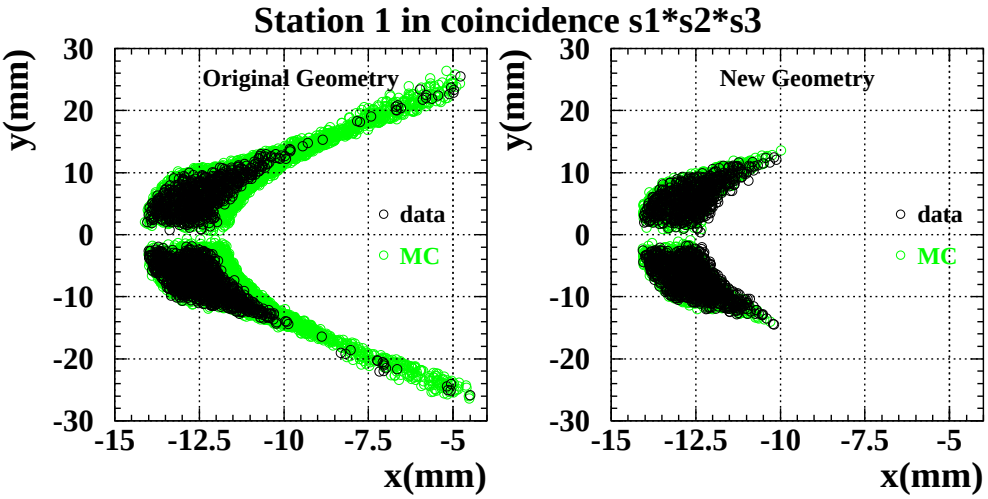

Figure 7.2: *$x-y$ map on station s1 in s1*s2*s3 coincidence using the original (left) and new (right) geometry. The black circles are the data and the green circles are the MC.*

of simulated events in the tail at higher p_T^2 is observed in the coincidence s2*s3. The x_L and p_T^2 distributions obtained for any coincidence are shown in figure 7.5.

The number of events in each LPS s123 coincidence is shown in figure 7.6 together with s456. In the left plot the total number of events is normalised to the data, taking into account the different luminosities of each spectrometer ($\mathcal{L}_{s123} = 9.0$ pb $^{-1}$ and $\mathcal{L}_{s456} = 12.8$ pb $^{-1}$).

In the right plot the ratio data/MC is plotted for each coincidence and it is observed to be $\simeq 30\%$ smaller in the s123 spectrometer. Assuming that the relative acceptance for s456 is correct (as confirmed by previous ZEUS analyses carried out with the LPS s456 spectrometer), we can conclude that the acceptance of s123 is overestimated.

7.2 Cross section measurement with a reduced event sample

In the s123 data sample the stations have two different spatial configurations depending on the data taking period. In the coincidence s2*s3 the position of the stations s2 and s3 are $\simeq 2$ mm shifted along the positive x direction starting from the data taking run number 27138. In figure 7.7 the data $x-y$ hit maps of the stations s2 (left) and s3(right) in the coincidence s2*s3 are shown (black circles) and the data taken before the run number 27138 are superimposed (green circles). Let define as $\overline{\text{s123}}$ and $\overline{\text{s456}}$ the sub-sets of the data collected from run number 27138. The luminosity of the $\overline{\text{s123}}$ sub-set

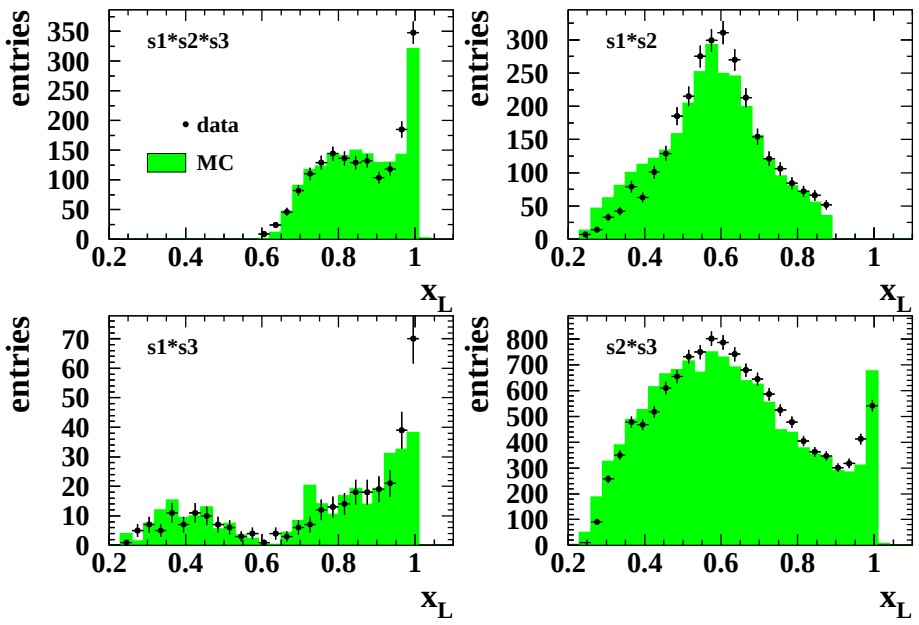

Figure 7.3: x_L *distribution for each station coincidence for data (dots) and MC (green histogram). The MC is normalised to the number of the data in each plot.*

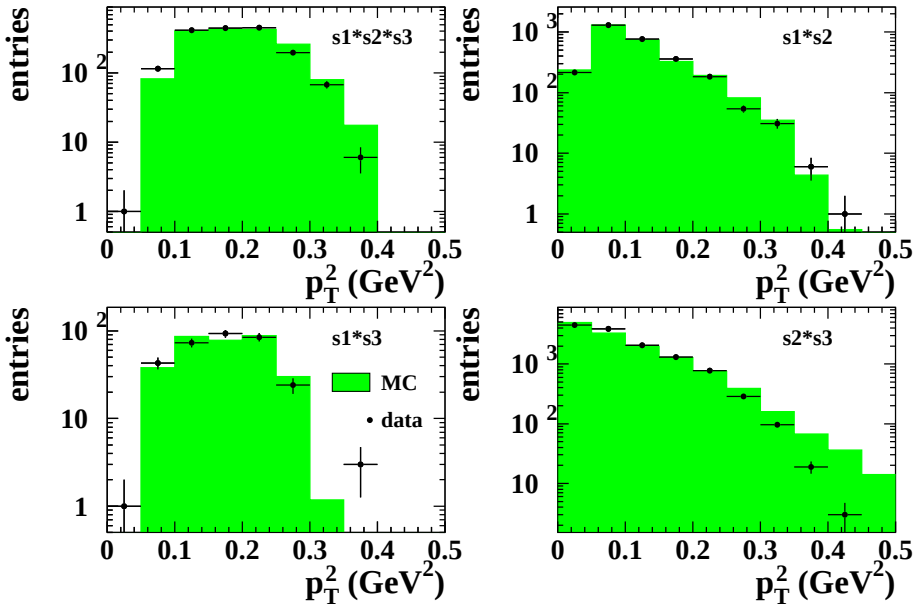

Figure 7.4: p_T^2 *distribution for each station coincidence for data (dots) and MC (green histogram). The MC is normalised to the number of the data in each plot.*

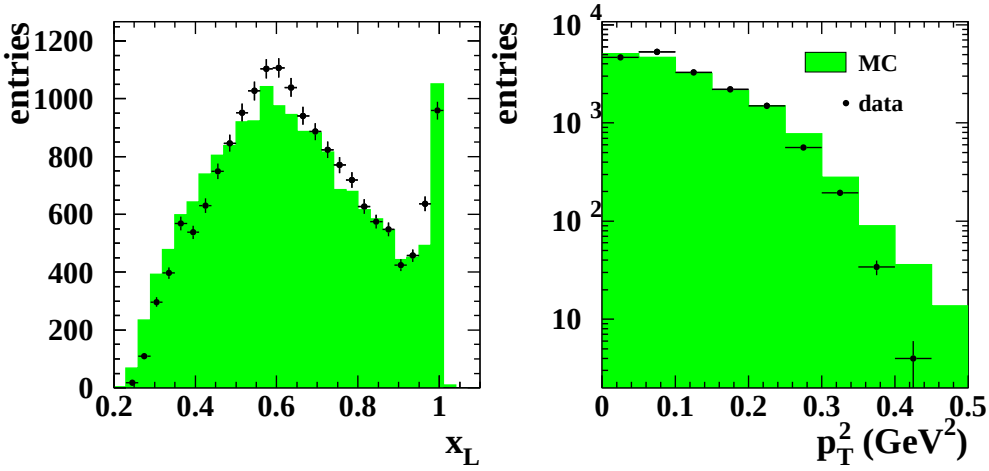

Figure 7.5: *x_L (left) and p_T^2 (right) distribution obtained for any coincidence for data (dots) and MC (green histogram).The MC is normalised to the number of the data in each plot.*

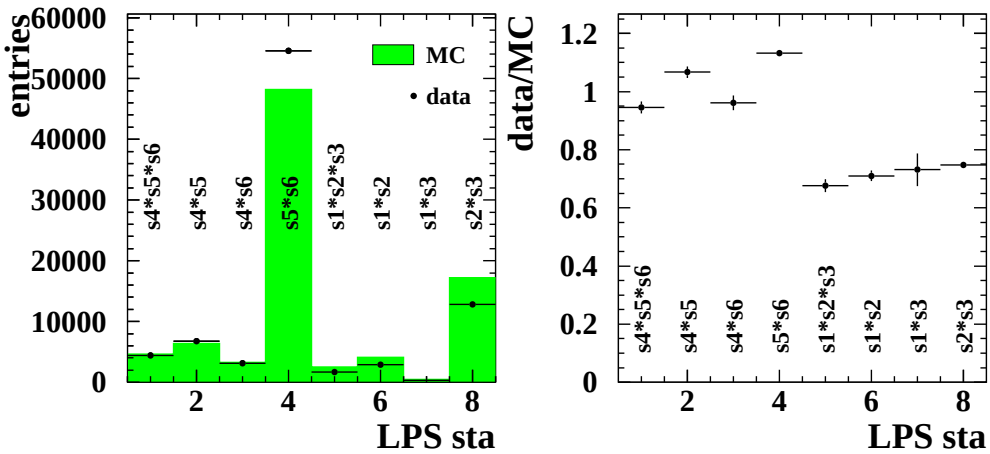

Figure 7.6: *Left: number of events for each LPS station coincidences for the data (dots) and MC (green histogrsm); the MC is normalised to the number of the data, taking into account the diffent luminosity of s123 and s456. Right: ratio data/MC for each LPS station coincidence.*

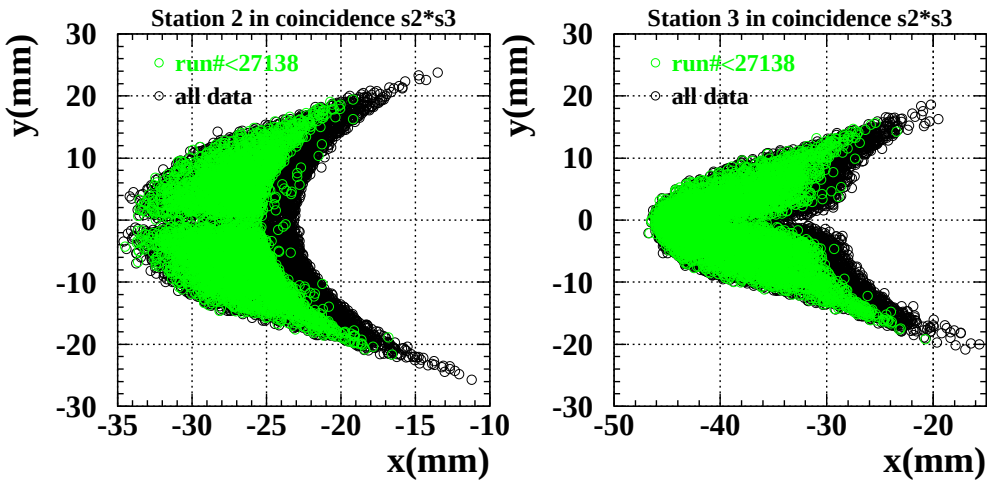

Figure 7.7: *$x-y$ hit map of station s2 (left) and s3 (right) in the coincidence s2*s3. The black circles represent the whole data set and the green circles are the data taken before run number 27138.*

is $\bar{\mathcal{L}}_{\rm s123} = 4.8$ pb $^{-1}$, more than a half of the total luminosity collected with LPS s123.

The x projections of the hit maps are reported in figure 7.8 (s2 on the left and s3 on the right) together with the MC. All distributions were normalised to the number of the data in $\overline{\rm s123}$. It can be noticed that the available Monte Carlo reproduces better the distribution of the data in $\overline{\rm s123}$.

The number of events in each coincidence was plotted for the $\overline{\rm s123}$ sample, togheter with $\overline{\rm s456}$ (fig. 7.9) and taking into account only that runs (or fractions of run) in which both s123 and s456 were in good data taking condition. In this way the effect due to the different luminosities of the two sub-samples cancel. The relative ratio data/MC in the coincidence $\overline{\rm s2*s3}$[1] is consistent with the ratio data/MC in $\overline{\rm s456}$, while an excess of acceptance is still present when s1 is included. Hence the events in the coincidences $\overline{\rm s1*s2*s3}$, $\overline{\rm s1*s2}$ and $\overline{\rm s1*s3}$, were discarded (the rejected events are $\simeq 20\%$).

In the $\overline{\rm s2*s3}$ coincidence the number of events after the selection cuts is 8586 (out of 12839 in the coincidence s2*s3 of the total s123 data set). The x_L and p_T^2 distribution for the coincidence $\overline{\rm s2*s3}$ are shown in figure 7.10. The x_L distribution is quit well reproduced (left plot), while in the region at $p_T^2 > 0.25$ GeV^2 the simulated event are still in excess (right plot).

The acceptance was calculated following the same criteria illustrated in section 6.2 and it was plotted as a function of x_L and p_T^2 (figure 7.11). The maximum s2*s3 acceptance value is 10% in the range $0.59 < x_L < 0.74$ and $0.05 < p_T^2 < 0.1$ GeV^2.

The single differential cross sections $d\sigma/dx_L$ and $d\sigma/dp_T^2$ were calculated

[1]The overline notation is referred to the coincidences in the $\overline{\rm s123}$ data set.

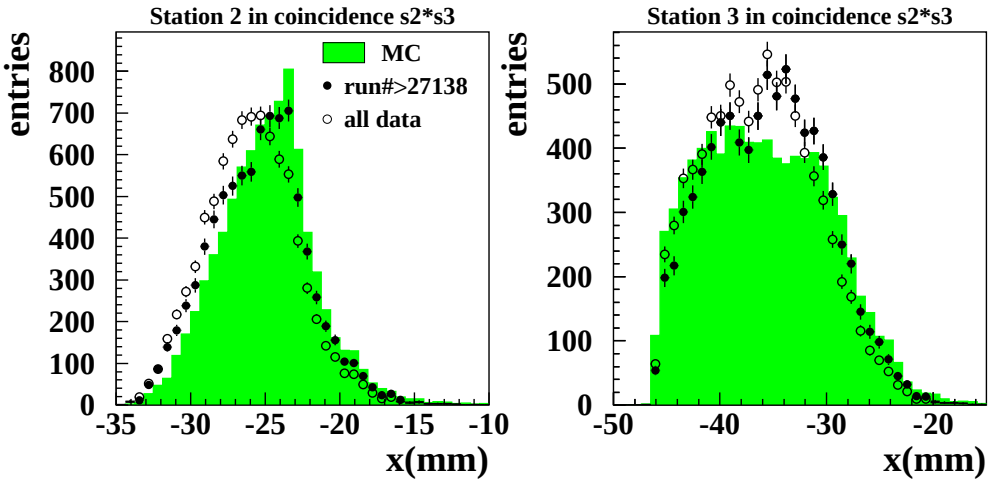

Figure 7.8: *x coordinate of the hit on the station s2 (left) and s3 (right) in coincidence s2*s3. The green histogram is the MC, the circles are the whole data set and the black dots are the data belonging to the sub-set* $\overline{s123}$. *The plotted distributions are normalised to the number of events of the* $\overline{s123}$ *sub-sample.*

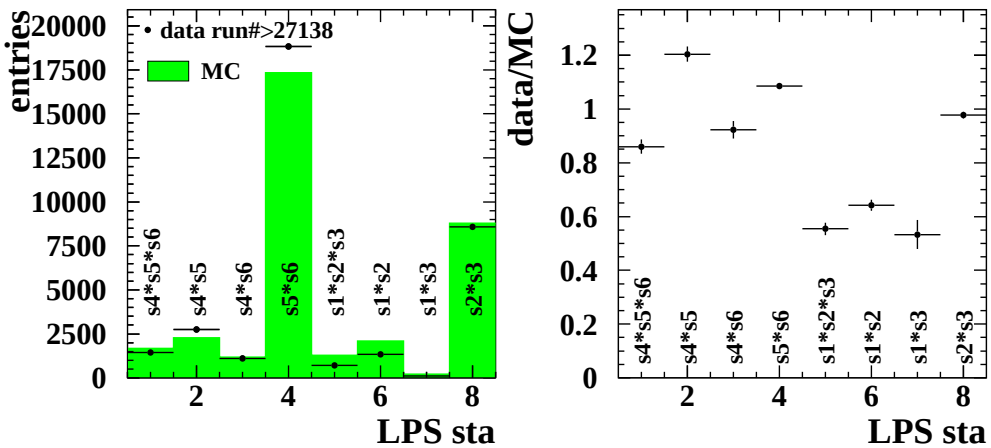

Figure 7.9: *Left: number of events for each LPS station coincidences for the data in* $\overline{s123}$ *and* $\overline{s456}$ *(dots) and MC (green histogram); the MC is normalised to the number of the data. Right: ratio data/MC for each LPS station coincidence.*

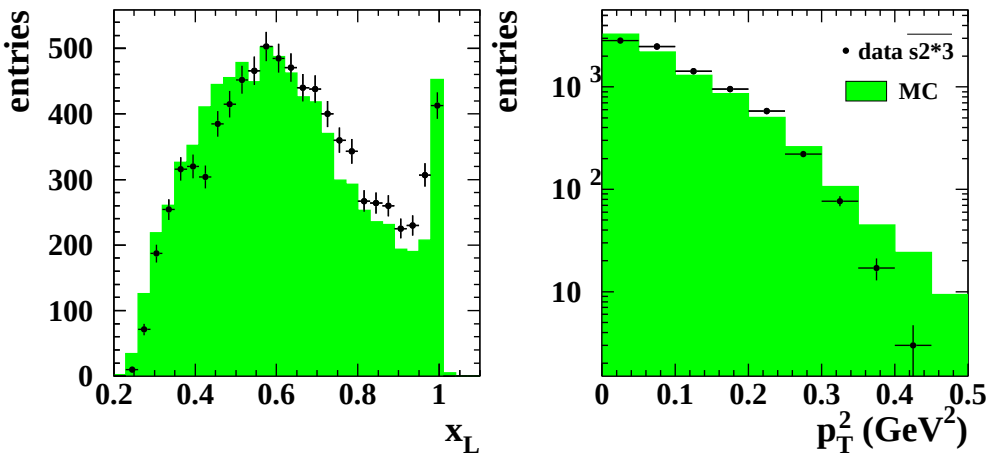

Figure 7.10: *x_L (left) and p_T^2 (right) distributions for the data (dots) and MC (green histogram) for events in $\overline{s2 * s3}$. The MC is normalised to the number of the data in each plot.*

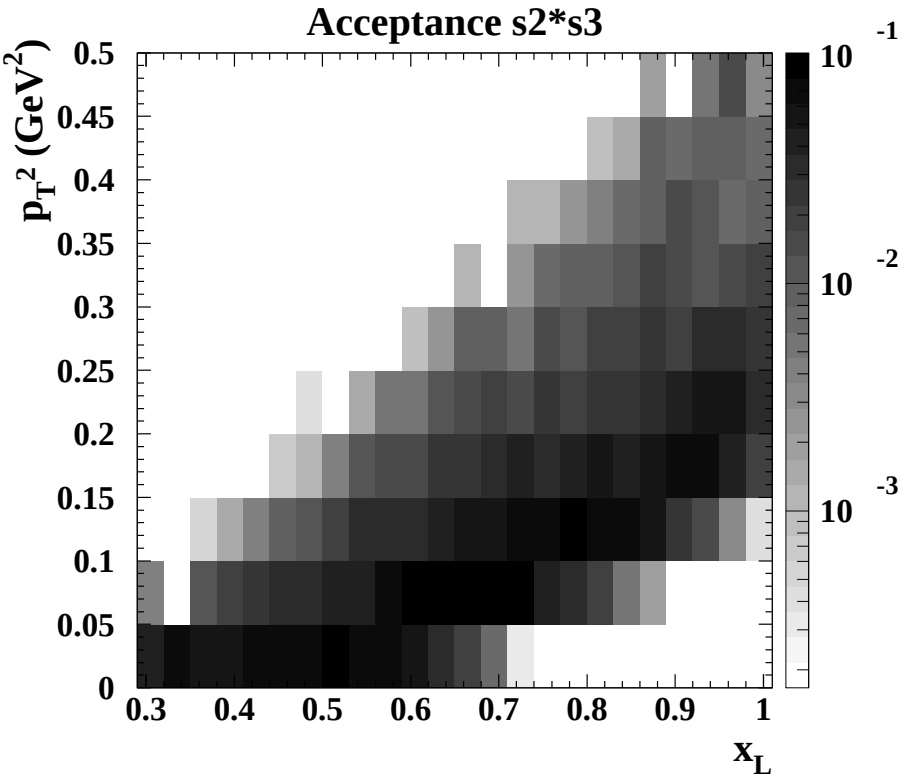

Figure 7.11: *s2*s3 acceptance as a function of x_L and p_T^2.*

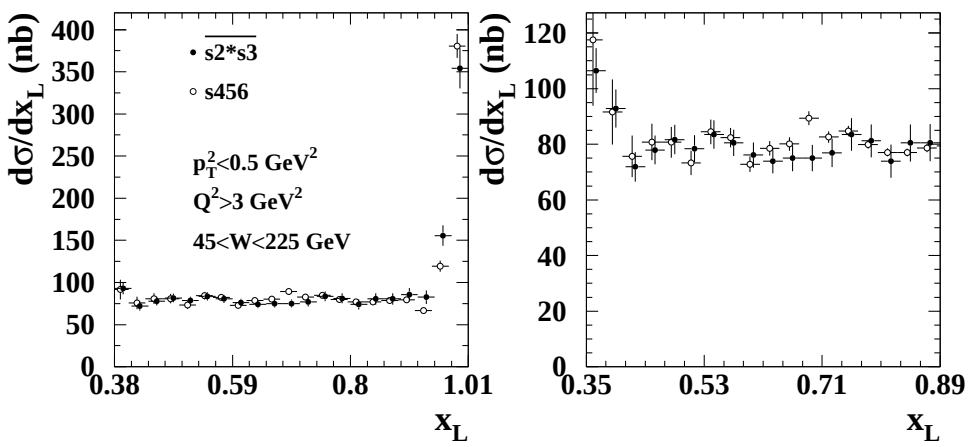

Figure 7.12: *Differential cross section $d\sigma/dx_L$ measured using $\overline{s2 * s3}$ (dots) and s456 (circles) in the kinematic range $p_T^2 < 0.5$ GeV^2, $Q^2 > 3$ GeV^2 and $45 < W < 225$ GeV. On the right the x_L range is reduced to put in evidence the statistical uncertainties.*

using the same method described in section 6.1. The background subtraction was also applied. The overlay events (section 5.6) were rejected only with the $E + p_z$ cut and the surviving fraction was neglected, since only a very small number of randomly triggered events was detected in s123. The background from π^+ and K^+ mis-reconstructed in the LPS (section 5.7) was subtracted by repeating the same study for the stations s123. The fraction of events migrating from low Q^2 regions (section 5.5) and the trigger effects (section 5.8) were assumed to be the same as in s456.

The differential cross section $d\sigma/dx_L$ was measured with the events in $\overline{\text{s2*s3}}$ in the kinematic range $p_T^2 < 0.5$ GeV^2, $Q^2 > 3$ GeV^2 and $45 < W < 225$ GeV. The result is reported in figure 7.12 where also the s456 result is shown. In the right figure a smaller x_L range was plotted to put in evidence the statistical errors. Even if the measurement of $d\sigma/dx_L$ is reliable only in the range $x_L > 0.56$, in figure 7.12 the x_L range was extended down to 0.38 to have an idea of the behaviour of the cross section at low x_L. In general the two measurement are consistent within the statistical uncertainties. The discrepancies at $x_L > 0.92$ could be due to resolution effects, it has to be understood yet.

The differential cross section $d\sigma/dp_T^2$ measured in $\overline{\text{s2*s3}}$ is shown in figure 7.13 together with the measurements carried out with s456. The two measurements were carried out in the kinematic range $x_L > 0.56$ GeV^2, $Q^2 > 3$ GeV^2 and $45 < W < 225$ GeV. The agreement is generally good in the range $0.05 < p_T^2 < 0.25$ GeV^2, but it tends to get worse elsewhere.

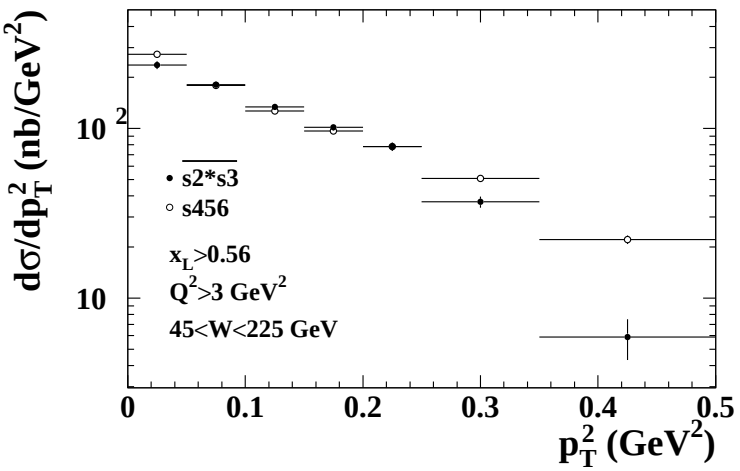

Figure 7.13: *Differential cross section* $d\sigma/dp_T^2$ *measured using* $\overline{s2*s3}$ *(dots) and s456 (circles) in the kinrmatic range* $x_L > 0.56$ GeV^2, $Q^2 > 3$ GeV^2 *and* $45 < W < 225$ GeV.

7.3 Conclusions

A new geometry for the stations s123 of the Leading Proton Spectrometer was implemented in the reconstruction program after that important differences were found between the actual and the design shapes of the stations s1 and s2. With the new geometry the overall simulation of the leading proton distribution improves, even if the number of simulated events in the LPS stations s123 is in excess in relation to s456. A sub-set of the data collected with s123 having a different spatial configuration of the station s2 and s3 in the coincidence s2*s3 was identified. The sub-set $\overline{s123}$ contains the events collected after the data taking run number 27138 and its luminosity is $\bar{\mathcal{L}}_{s123} = 4.8$ pb $^{-1}$. It was found that the MC describe quite well the events in the sub-set coincidence $\overline{s2*s3}$ and the cross section measurements carried out with this reduced sample are in reasonable agreement with the ones measured with the LPS stations s456.

The LPS stations s123 were never used in a physics analysis and these very preliminary results are encouraging. The simulation of the full LPS data sample will give the opportunity to measure the leading proton production in a kinematic range never explored before at HERA.

Conclusions

The leading-proton production in DIS semi-inclusive reaction $ep \to ep'X$ was studied using the data collected with the Leading Proton Spectrometer of the ZEUS experiment at HERA during the 1997 data taking period, corresponding to an integrated luminosity of 12.8 pb^{-1}.

The analysis was mainly performed using the leading-protons detected in the LPS stations s4-s5-s6. The measurement were carried out in the kinematic range $Q^2 > 3$ GeV^2, $45 < W < 225$ GeV, $p_T^2 < 0.5$ GeV^2 and $x_L > 0.56$.

The single differential cross section as a function of the longitudinal fractional momentum $d\sigma_{ep\to ep'X}/dx_L$ was found to be independent from x_L up to the diffractive peak where it becomes approximately five times larger. The single differential cross section as a function of the transverse squared momentum $d\sigma_{ep\to ep'X}/dp_T^2$ has an exponential behaviour. The double differential cross section $d^2\sigma_{ep\to ep'X}/dx_L dp_T^2$ was measured as a function of p_T^2 in bins of x_L and it was fitted to the exponential function $A\exp(-b\cdot p_T^2)$. The b-slopes have a mean value $\langle b\rangle \approx 6.9$, without showing any strong dependence on x_L and the measurement agrees with the theoretical predictions and with the previous measurements carried out with ZEUS 1995 data.

The single differential cross section normalised to the total DIS cross section $1/\sigma_{tot}\cdot d\sigma_{ep\to ep'X}/dx_L$ was found to be in a very good agreement with the theoretical expectations and the result is consistent with the old ZEUS measurement.

The leading-proton production was also compared to the inclusive DIS $ep \to eX$ scattering. The ratio $r^{LP(3)}(x, Q^2, x_L)$ of the structure function F_2^{LP} for events with a leading-proton to the inclusive F_2 was measured as a function of x_L in bins of the DIS variables x and Q^2. It is observed to be almost independent on x and Q^2. The same ratio integrated over x_L, $r^{LP(2)}(x, Q^2)$, was measured as a function of x for fixed Q^2 values. The mean $\langle r^{LP(2)}\rangle$ as a function of Q^2 decreases in the low Q^2 region. The observed behaviour can be explained in terms of rescattering of the leading-proton on the hadronic components of the quasi-real exchanged photon.

The leading-proton-tagged structure function $\bar{F}_2^{LP}$ was measured as a function of x for fixed Q^2 values and its dependence on the variables x and Q^2 is similar to the DIS structure function F_2.

Finally, the single differential cross sections $d\sigma/dx_L$ and $d\sigma/dp_T^2$ were evaluated using data collected in the LPS stations s1-s2-s3. These are highly preliminary results, as work is in progress to fully commission this spectrometer that up to now has never been used for physics analyses. The comparison of the results obtained with those from the main analysis with the stations s4-s5-s6 is however quite encouraging.

Acknowledgements

Questa tesi è l'ultimo tassello che va a completare il quadro dei miei tre anni di dottorato, durante i quali ho avuto il mio primo vero contatto con il mondo della ricerca scientifica a ho avuto l'opportunità di versare la mia infinitesima goccia nell'infinito mare della conoscenza umana. I miei sforzi sarebbero stati vani senza le persone che mi sono state accanto.

Vorrei ringraziare il mio supervisore, Prof. Maurizio Basile, che mi ha offerto il suo supporto e la sua esperienza per farmi raggiungere questo traguardo.

Un ringraziamento enorme va a Graziano Bruni e Peppe Iacobucci, guide sagge e pazienti, che mi hanno trasferito le loro preziose conoscenze e che hanno seguito ogni mio passo durante questi tre anni di dottorato.

Un importante riconoscimento va a tutti i componenti del gruppo ZEUS-Bologna, in particolare a Lorenzo Bellagamba, Davide Boscherini, Alessia Bruni, Massimo Corradi, Alessandro Montanari (now at DESY), Alessandro Pesci e Alessandro Polini, ai nuovi arrivati Marcello e Stefano nonchè a tutti i numerosi membri del ZEUS-IT Cluster. Grazie per tutte le utili discussioni e suggerimenti e per tutti i momenti passati in vostra compagnia.

I would like to thank the people of the ZEUS Collaboration that followed my work. In particular the Diffractive group "staff", Alessia Bruni, Kerstin Borras, Jo Cole, Uta Stoesslein, Marta Ruspa and Michele Arneodo for their support to my analysis and for their precious advices and discussions.

Si dice che noi fisici abbiamo un modo tutto nostro di vedere le cose. Non ho ancora capito quale sia il punto di transizione (e forse mai lo capirò), ma è sempre un piacere tornare in quel mondo fatto di amicizia e amore, ma anche di ansie e preoccupazioni, fatto delle persone che ci circondano a cui vogliamo bene e da cui riceviamo tanto affetto. Sono troppe le persone per elencarle tutte e nel farlo sicuramente dimenticherei qualcuno. Perciò voglio dire grazie a tutti coloro con i quali ho trascorso momenti felici e che mi sono stati vicini nei momenti difficili.

Un pensiero speciale va ai miei genitori, ai miei fratellini e alla mia cara e lontana famiglia.

Il ringraziamento più grande è certamente per la mia Lauretta, che è stata sempre accanto a me, offrendomi tutto il suo amore senza il quale tutto questo non sarebbe stato possibile.

Appendix A

Tables

x_L **bin**	**Overlay Events fraction**
$0.47 < x_L < 0.50$	0.021 ± 0.036
$0.50 < x_L < 0.53$	0.013 ± 0.022
$0.53 < x_L < 0.56$	0.006 ± 0.011
$0.56 < x_L < 0.59$	0.005 ± 0.009
$0.59 < x_L < 0.62$	0.004 ± 0.007
$0.62 < x_L < 0.65$	0.002 ± 0.003
$0.65 < x_L < 0.68$	0.005 ± 0.006
$0.68 < x_L < 0.71$	0.004 ± 0.005
$0.71 < x_L < 0.74$	0.004 ± 0.005
$0.74 < x_L < 0.77$	0.005 ± 0.005
$0.77 < x_L < 0.80$	0.004 ± 0.004
$0.80 < x_L < 0.83$	0.003 ± 0.003
$0.83 < x_L < 0.86$	0.004 ± 0.004
$0.86 < x_L < 0.89$	0.004 ± 0.004
$0.89 < x_L < 0.92$	0.005 ± 0.005
$0.92 < x_L < 0.95$	0.040 ± 0.018
$0.95 < x_L < 0.98$	0.069 ± 0.026
$0.98 < x_L < 1.01$	0.079 ± 0.010

Table A.1: *Overlay event fraction in bin of x_L used to correct the cross section measurements.*

x_L **bin**	π^+ **and** X^+ **fraction**
$0.38 < x_L < 0.41$	0.195 ± 0.031
$0.41 < x_L < 0.44$	0.165 ± 0.023
$0.44 < x_L < 0.47$	0.187 ± 0.028
$0.47 < x_L < 0.50$	0.111 ± 0.013
$0.50 < x_L < 0.53$	0.108 ± 0.013
$0.53 < x_L < 0.56$	0.091 ± 0.011
$0.56 < x_L < 0.59$	0.068 ± 0.008
$0.59 < x_L < 0.62$	0.071 ± 0.008
$0.62 < x_L < 0.65$	0.048 ± 0.006
$0.65 < x_L < 0.68$	0.032 ± 0.004
$0.68 < x_L < 0.71$	0.026 ± 0.004
$0.71 < x_L < 0.74$	0.020 ± 0.003
$0.74 < x_L < 0.77$	0.016 ± 0.003
$0.77 < x_L < 0.80$	0.010 ± 0.002
$0.80 < x_L < 0.83$	0.010 ± 0.002
$0.83 < x_L < 0.86$	0.011 ± 0.002
$0.86 < x_L < 0.89$	0.005 ± 0.001
$0.89 < x_L < 0.92$	0.005 ± 0.002
$0.92 < x_L < 0.95$	0.002 ± 0.001
$x_L > 0.95$	0.0
p_T^2 **bin**	π^+ **and** X^+ **fraction**
$0.00 < p_T^2 < 0.05$ GeV^2	0.017 ± 0.001
$0.05 < p_T^2 < 0.10$ GeV^2	0.017 ± 0.001
$0.10 < p_T^2 < 0.15$ GeV^2	0.015 ± 0.002
$0.15 < p_T^2 < 0.20$ GeV^2	0.022 ± 0.004
$0.20 < p_T^2 < 0.25$ GeV^2	0.018 ± 0.004
$0.25 < p_T^2 < 0.35$ GeV^2	0.018 ± 0.003
$0.35 < p_T^2 < 0.50$ GeV^2	0.021 ± 0.008

Table A.2: *Charged meson π^+ and K^+ fraction in each x_L and p_T^2 bin, used to correct the cross section measurements.*

x_L **bin**	**trigger inefficiency**
$0.38 < x_L < 0.41$	0.995 ± 0.097
$0.41 < x_L < 0.44$	0.996 ± 0.080
$0.44 < x_L < 0.47$	1.000 ± 0.064
$0.47 < x_L < 0.50$	1.000 ± 0.054
$0.50 < x_L < 0.53$	0.994 ± 0.048
$0.53 < x_L < 0.56$	0.994 ± 0.041
$0.56 < x_L < 0.59$	0.994 ± 0.033
$0.59 < x_L < 0.62$	0.997 ± 0.032
$0.62 < x_L < 0.65$	0.996 ± 0.027
$0.65 < x_L < 0.68$	0.997 ± 0.024
$0.68 < x_L < 0.71$	0.998 ± 0.022
$0.71 < x_L < 0.74$	0.997 ± 0.020
$0.74 < x_L < 0.77$	0.997 ± 0.018
$0.77 < x_L < 0.80$	0.997 ± 0.016
$0.80 < x_L < 0.83$	0.997 ± 0.015
$0.83 < x_L < 0.86$	0.997 ± 0.016
$0.86 < x_L < 0.89$	0.998 ± 0.016
$0.89 < x_L < 0.92$	0.997 ± 0.019
$0.92 < x_L < 0.95$	0.997 ± 0.029
$0.95 < x_L > 0.98$	0.996 ± 0.041
$0.98 < x_L > 1.01$	0.990 ± 0.028
p_T^2 **bin**	**trigger inefficiency**
$0.00 < p_T^2 < 0.05$ GeV^2	0.997 ± 0.006
$0.05 < p_T^2 < 0.10$ GeV^2	0.996 ± 0.012
$0.10 < p_T^2 < 0.15$ GeV^2	0.996 ± 0.018
$0.15 < p_T^2 < 0.20$ GeV^2	0.995 ± 0.024
$0.20 < p_T^2 < 0.25$ GeV^2	0.996 ± 0.030
$0.25 < p_T^2 < 0.35$ GeV^2	0.994 ± 0.030
$0.35 < p_T^2 < 0.50$ GeV^2	0.998 ± 0.049

Table A.3: *Trigger effect correction factors for each x_L and p_T^2 bin.*

x_L **bin**	**Resolution %**	p_T^2 **bin (GeV^2)**	**Resolution %**
$0.47 < x_L < 0.50$	0.0011	$0.00 < p_T^2 < 0.05$	0.36
$0.50 < x_L < 0.53$	0.0011	$0.05 < p_T^2 < 0.10$	0.26
$0.53 < x_L < 0.56$	0.0010	$0.10 < p_T^2 < 0.15$	0.23
$0.56 < x_L < 0.59$	0.0010	$0.15 < p_T^2 < 0.20$	0.20
$0.59 < x_L < 0.62$	0.0010	$0.20 < p_T^2 < 0.25$	0.19
$0.62 < x_L < 0.65$	0.0011	$0.25 < p_T^2 < 0.35$	0.18
$0.65 < x_L < 0.68$	0.0011	$0.35 < p_T^2 < 0.50$	0.16
$0.68 < x_L < 0.71$	0.0012		
$0.71 < x_L < 0.74$	0.0012		
$0.74 < x_L < 0.77$	0.0013		
$0.77 < x_L < 0.80$	0.0016		
$0.80 < x_L < 0.83$	0.0020		
$0.83 < x_L < 0.86$	0.0025		
$0.86 < x_L < 0.89$	0.0035		
$0.89 < x_L < 0.92$	0.0038		
$0.92 < x_L < 0.95$	0.0033		
$0.95 < x_L < 0.98$	0.0028		
$0.98 < x_L < 1.01$	0.0028		

Table A.4: *Binning of the variables x_L and p_T^2 with the resolutions.*

x_{DA} **bin**	$\langle x_{DA} \rangle$
$1 \cdot 10^{-6} < x_{DA} < 1 \cdot 10^{-4}$	$8.5 \cdot 10^{-5}$
$1 \cdot 10^{-4} < x_{DA} < 2 \cdot 10^{-4}$	$1.5 \cdot 10^{-4}$
$2 \cdot 10^{-4} < x_{DA} < 4 \cdot 10^{-4}$	$2.9 \cdot 10^{-4}$
$4 \cdot 10^{-4} < x_{DA} < 8 \cdot 10^{-4}$	$5.8 \cdot 10^{-4}$
$8 \cdot 10^{-4} < x_{DA} < 1.6 \cdot 10^{-3}$	$1.1 \cdot 10^{-3}$
$1.6 \cdot 10^{-3} < x_{DA} < 3.2 \cdot 10^{-3}$	$2.3 \cdot 10^{-3}$
$3.2 \cdot 10^{-3} < x_{DA} < 6.4 \cdot 10^{-3}$	$4.4 \cdot 10^{-3}$
$6.4 \cdot 10^{-3} < x_{DA} < 1.28 \cdot 10^{-2}$	$8.7 \cdot 10^{-3}$
$1.28 \cdot 10^{-2} < x_{DA} < 2.56 \cdot 10^{-2}$	$1.7 \cdot 10^{-2}$
$2,56 \cdot 10^{-2} < x_{DA} < 5.12 \cdot 10^{-2}$	$3.5 \cdot 10^{-2}$
$5.12 \cdot 10^{-2} < x_{DA} < 0.5$	$8.3 \cdot 10^{-2}$

Q^2_{DA} **bin** ($\mathbf{GeV}^2$)	$\langle Q^2_{DA} \rangle$ ($\mathbf{GeV}^2$)
$3 < Q^2_{DA} < 4$	3.4
$4 < Q^2_{DA} < 8$	5.9
$8 < Q^2_{DA} < 16$	11
$16 < Q^2_{DA} < 32$	22
$32 < Q^2_{DA} < 64$	44
$64 < Q^2_{DA} < 128$	88
$128 < Q^2_{DA} < 256$	174
$256 < Q^2_{DA} < 1000$	377

Table A.5: *Binning of the DIS variables x and Q^2 with bin average values.*

x_L **bin**	**Acceptance**	p_T^2 **bin (GeV^2)**	**acceptance**
$0.47 < x_L < 0.50$	0.0177 ± 0.0007	$0.00 < p_T^2 < 0.05$	0.197 ± 0.001
$0.50 < x_L < 0.53$	0.0246 ± 0.0008	$0.05 < p_T^2 < 0.10$	0.098 ± 0.001
$0.53 < x_L < 0.56$	0.0302 ± 0.0011	$0.10 < p_T^2 < 0.15$	0.065 ± 0.001
$0.56 < x_L < 0.59$	0.0468 ± 0.0013	$0.15 < p_T^2 < 0.20$	0.047 ± 0.001
$0.59 < x_L < 0.62$	0.0593 ± 0.0015	$0.20 < p_T^2 < 0.25$	0.034 ± 0.001
$0.62 < x_L < 0.65$	0.0761 ± 0.0017	$0.25 < p_T^2 < 0.35$	0.029 ± 0.001
$0.65 < x_L < 0.68$	0.0922 ± 0.0019	$0.35 < p_T^2 < 0.50$	0.017 ± 0.001
$0.68 < x_L < 0.71$	0.1051 ± 0.0020		
$0.71 < x_L < 0.74$	0.1302 ± 0.0022		
$0.74 < x_L < 0.77$	0.1623 ± 0.0024		
$0.77 < x_L < 0.80$	0.2025 ± 0.0026		
$0.80 < x_L < 0.83$	0.2341 ± 0.0028		
$0.83 < x_L < 0.86$	0.2275 ± 0.0027		
$0.86 < x_L < 0.89$	0.2086 ± 0.0026		
$0.89 < x_L < 0.92$	0.1540 ± 0.0024		
$0.92 < x_L < 0.95$	0.0786 ± 0.0027		
$0.95 < x_L < 0.98$	0.0205 ± 0.0008		
$0.98 < x_L < 1.01$	0.0140 ± 0.0003		

Table A.6: *Acceptance in bins of x_L and p_T^2.*

x_L **bin**	$d\sigma_{ep\to ep'X}/dx_L$ **(nb)**
$0.56 < x_L < 0.59$	$81.73 \pm 3.34^{+3.93}_{-3.67}$
$0.59 < x_L < 0.62$	$71.98 \pm 2.7^{+3.18}_{-2.52}$
$0.62 < x_L < 0.65$	$78.89 \pm 2.56^{+3.24}_{-2.93}$
$0.65 < x_L < 0.68$	$81.89 \pm 2.39^{+3.7}_{-2.77}$
$0.68 < x_L < 0.71$	$90.89 \pm 2.42^{+3.66}_{-4.15}$
$0.71 < x_L < 0.74$	$84.46 \pm 2.04^{+4.37}_{-3.64}$
$0.74 < x_L < 0.77$	$86.71 \pm 1.83^{+4.49}_{-4}$
$0.77 < x_L < 0.80$	$82.14 \pm 1.57^{+4.33}_{-3.48}$
$0.80 < x_L < 0.83$	$78.95 \pm 1.4^{+3.12}_{-3.4}$
$0.83 < x_L < 0.86$	$78.92 \pm 1.41^{+3.2}_{-2.87}$
$0.86 < x_L < 0.89$	$80.99 \pm 1.52^{+4.14}_{-2.48}$
$0.89 < x_L < 0.92$	$81.52 \pm 1.82^{+3.44}_{-2.07}$
$0.92 < x_L < 0.95$	$69.17 \pm 3.02^{+5.32}_{-1.44}$
$0.95 < x_L < 0.98$	$123.3 \pm 6.59^{+5.06}_{-4.22}$
$0.98 < x_L < 1.01$	$391.83 \pm 14.18^{+11.54}_{-11.54}$

Table A.7: *Single differential cross section $d\sigma_{ep\to ep'X}/dx_L$ in bins of x_L with the statistical and systematic uncertainties.*

x_L **bin**	$1/\sigma_{tot} \cdot d\sigma_{ep\to ep'X}/dx_L$
$0.56 < x_L < 0.59$	$0.364 \pm 0.014^{+0.015}_{-0.011}$
$0.59 < x_L < 0.62$	$0.323 \pm 0.012^{+0.014}_{-0.011}$
$0.62 < x_L < 0.65$	$0.344 \pm 0.011^{+0.011}_{-0.009}$
$0.65 < x_L < 0.68$	$0.351 \pm 0.01^{+0.013}_{-0.011}$
$0.68 < x_L < 0.71$	$0.387 \pm 0.01^{+0.013}_{-0.012}$
$0.71 < x_L < 0.74$	$0.357 \pm 0.008^{+0.017}_{-0.016}$
$0.74 < x_L < 0.77$	$0.367 \pm 0.007^{+0.017}_{-0.014}$
$0.77 < x_L < 0.80$	$0.346 \pm 0.006^{+0.016}_{-0.013}$
$0.80 < x_L < 0.83$	$0.332 \pm 0.005^{+0.012}_{-0.011}$
$0.83 < x_L < 0.86$	$0.334 \pm 0.006^{+0.011}_{-0.009}$
$0.86 < x_L < 0.89$	$0.342 \pm 0.006^{+0.014}_{-0.008}$
$0.89 < x_L < 0.92$	$0.343 \pm 0.007^{+0.013}_{-0.007}$
$0.92 < x_L < 0.95$	$0.292 \pm 0.012^{+0.021}_{-0.005}$
$0.95 < x_L < 0.98$	$0.52 \pm 0.028^{+0.025}_{-0.02}$
$0.98 < x_L < 1.01$	$1.593 \pm 0.058^{+0.051}_{-0.042}$

Table A.8: *Single differential cross section normalised to the total DIS cross section* $1/\sigma_{tot} \cdot d\sigma_{ep\to ep'X}/dx_L$ *in bins of* x_L *with the statistical and systematic uncertainties.*

p_T^2 **bin**	$d\sigma_{ep\to ep'X}/dp_T^2$ **(nb/GeV^2)**
$0 < p_T^2 < 0.05$ GeV^2	$273.41 \pm 2.25^{+20.44}_{-7.45}$
$0.05 < p_T^2 < 0.1$ GeV^2	$179.68 \pm 2.67^{+11.81}_{-4.41}$
$0.1 < p_T^2 < 0.15$ GeV^2	$126.84 \pm 2.7^{+6.41}_{-3.68}$
$0.15 < p_T^2 < 0.2$ GeV^2	$96.59 \pm 2.77^{+4.46}_{-2.7}$
$0.2 < p_T^2 < 0.25$ GeV^2	$78.09 \pm 2.89^{+3.24}_{-2.04}$
$0.25 < p_T^2 < 0.35$ GeV^2	$50.75 \pm 1.82^{+2.47}_{-2.14}$
$0.35 < p_T^2 < 0.5$ GeV^2	$22.08 \pm 1.24^{+1.65}_{-0.97}$

Table A.9: *Single differential cross section $d\sigma_{ep\to ep'X}/dp_T^2$ in bins of p_T^2 with the statistical and systematic uncertainties.*

x_L **bin**	b**-slope (GeV^{-2})**
$0.56 < x_L < 0.59$	$10.13 \pm 1.36^{+0.44}_{-0.36}$
$0.59 < x_L < 0.62$	$6.98 \pm 0.83^{+0.25}_{-0.25}$
$0.62 < x_L < 0.65$	$7.85 \pm 0.64^{+0.22}_{-0.39}$
$0.65 < x_L < 0.68$	$6.94 \pm 0.39^{+0.13}_{-0.09}$
$0.68 < x_L < 0.71$	$6.4 \pm 0.32^{+0.04}_{-0.1}$
$0.71 < x_L < 0.74$	$7.02 \pm 0.44^{+0.11}_{-0.07}$
$0.74 < x_L < 0.77$	$7.73 \pm 0.57^{+0.18}_{-0.35}$
$0.77 < x_L < 0.80$	$7.18 \pm 0.71^{+0.4}_{-0.4}$
$0.80 < x_L < 0.83$	$7.15 \pm 0.39^{+0.19}_{-0.13}$
$0.83 < x_L < 0.86$	$5.9 \pm 0.3^{+0.22}_{-0.06}$
$0.86 < x_L < 0.89$	$6.25 \pm 0.24^{+0.18}_{-0.1}$
$0.89 < x_L < 0.92$	$6.59 \pm 0.32^{+0.17}_{-0.13}$
$0.92 < x_L < 0.98$	$5.01 \pm 0.31^{+0.17}_{-0.2}$
$0.98 < x_L < 1.01$	$7.7 \pm 0.67^{+0.21}_{-0.3}$

Table A.10: *b-slope in bins of x_L with the statistical and systematic uncertainties.*

x	Q^2 **(GeV^2)**	x_L	$r^{LP(3)}$
8.5E-05	3.4	0.59	0.380±0.057+0.053−0.026
8.5E-05	3.4	0.65	0.402±0.046+0.027−0.021
8.5E-05	3.4	0.71	0.459±0.042+0.020−0.020
8.5E-05	3.4	0.77	0.373±0.031+0.033−0.022
8.5E-05	3.4	0.83	0.394±0.028+0.027−0.028
8.5E-05	3.4	0.89	0.400±0.032+0.038−0.013
0.00015	3.4	0.59	0.400±0.037+0.031−0.018
0.00015	3.4	0.65	0.403±0.029+0.021−0.014
0.00015	3.4	0.71	0.395±0.025+0.020−0.014
0.00015	3.4	0.77	0.382±0.020+0.022−0.016
0.00015	3.4	0.83	0.360±0.017+0.027−0.017
0.00015	3.4	0.89	0.354±0.019+0.024−0.010
0.00029	3.4	0.59	0.341±0.032+0.020−0.012
0.00029	3.4	0.65	0.377±0.027+0.017−0.015
0.00029	3.4	0.71	0.371±0.023+0.018−0.022
0.00029	3.4	0.77	0.325±0.017+0.016−0.016
0.00029	3.4	0.83	0.319±0.015+0.013−0.012
0.00029	3.4	0.89	0.320±0.017+0.012−0.011
0.00058	3.4	0.59	0.327±0.033+0.014−0.011
0.00058	3.4	0.65	0.351±0.027+0.017−0.010
0.00058	3.4	0.71	0.328±0.022+0.016−0.011
0.00058	3.4	0.77	0.303±0.017+0.015−0.011
0.00058	3.4	0.83	0.330±0.016+0.012−0.012
0.00058	3.4	0.89	0.317±0.018+0.014−0.006
0.00114	3.4	0.59	0.311±0.042+0.012−0.075
0.00114	3.4	0.65	0.348±0.035+0.018−0.012
0.00114	3.4	0.71	0.354±0.030+0.021−0.028
0.00114	3.4	0.77	0.435±0.027+0.018−0.027
0.00114	3.4	0.83	0.347±0.022+0.011−0.025
0.00114	3.4	0.89	0.353±0.024+0.010−0.02
0.00225	3.4	0.575	0.408±0.151+0.014−0.199
0.00225	3.4	0.725	0.463±0.100+0.060−0.031
0.00225	3.4	0.875	0.324±0.072+0.072−0.023

Table A.11: *Ratio $r^{LP(3)}$ in bins of x, Q^2 and x_L with the statistical, upper-systematic and lower-systematic uncertainties.*

x	Q^2 $(\mathbf{GeV}^2)$	x_L	$r^{LP(3)}$
8.5E-05	5.9	0.575	0.198±0.048+0.015−0.019
8.5E-05	5.9	0.725	0.321±0.037+0.026−0.036
8.5E-05	5.9	0.875	0.317±0.033+0.026−0.009
0.00015	5.9	0.59	0.397±0.026+0.020−0.014
0.00015	5.9	0.65	0.380±0.020+0.013−0.016
0.00015	5.9	0.71	0.410±0.018+0.017−0.015
0.00015	5.9	0.77	0.375±0.014+0.020−0.014
0.00015	5.9	0.83	0.396±0.013+0.015−0.014
0.00015	5.9	0.89	0.382±0.014+0.017−0.009
0.00029	5.9	0.59	0.367±0.022+0.019−0.013
0.00029	5.9	0.65	0.386±0.018+0.022−0.011
0.00029	5.9	0.71	0.408±0.016+0.019−0.014
0.00029	5.9	0.77	0.406±0.013+0.024−0.015
0.00029	5.9	0.83	0.366±0.011+0.016−0.011
0.00029	5.9	0.89	0.375±0.012+0.018−0.009
0.00058	5.9	0.59	0.385±0.026+0.020−0.013
0.00058	5.9	0.65	0.413±0.022+0.017−0.015
0.00058	5.9	0.71	0.416±0.019+0.020−0.025
0.00058	5.9	0.77	0.435±0.015+0.022−0.016
0.00058	5.9	0.83	0.405±0.013+0.015−0.013
0.00058	5.9	0.89	0.406±0.015+0.016−0.011
0.00114	5.9	0.59	0.337±0.027+0.012−0.010
0.00114	5.9	0.65	0.350±0.022+0.011−0.012
0.00114	5.9	0.71	0.405±0.020+0.015−0.019
0.00114	5.9	0.77	0.369±0.016+0.017−0.015
0.00114	5.9	0.83	0.367±0.014+0.013−0.019
0.00114	5.9	0.89	0.400±0.016+0.013−0.010
0.00225	5.9	0.59	0.355±0.042+0.047−0.017
0.00225	5.9	0.65	0.436±0.037+0.026−0.015
0.00225	5.9	0.71	0.445±0.032+0.023−0.020
0.00225	5.9	0.77	0.416±0.025+0.019−0.020
0.00225	5.9	0.83	0.443±0.023+0.024−0.014
0.00225	5.9	0.89	0.372±0.024+0.022−0.010
0.00445	5.9	0.65	0.509±0.088+0.041−0.235

Table A.12: *Ratio $r^{LP(3)}$ in bins of x, Q^2 and x_L with the statistical, upper-systematic and lower-systematic uncertainties.*

x	Q^2 **(GeV^2)**	x_L	$r^{LP(3)}$
0.00015	11	0.575	0.327±0.069+0.023−0.030
0.00015	11	0.725	0.397±0.047+0.044−0.056
0.00015	11	0.875	0.372±0.040+0.033−0.010
0.00029	11	0.59	0.393±0.028+0.016−0.018
0.00029	11	0.65	0.367±0.021+0.023−0.011
0.00029	11	0.71	0.404±0.019+0.023−0.016
0.00029	11	0.77	0.386±0.015+0.025−0.015
0.00029	11	0.83	0.371±0.013+0.017−0.015
0.00029	11	0.89	0.374±0.015+0.026−0.014
0.00058	11	0.59	0.345±0.022+0.015−0.014
0.00058	11	0.65	0.338±0.017+0.016−0.009
0.00058	11	0.71	0.401±0.016+0.016−0.014
0.00058	11	0.77	0.375±0.013+0.018−0.014
0.00058	11	0.83	0.334±0.010+0.013−0.010
0.00058	11	0.89	0.365±0.012+0.015−0.008
0.00114	11	0.59	0.382±0.026+0.019−0.011
0.00114	11	0.65	0.387±0.021+0.016−0.013
0.00114	11	0.71	0.435±0.019+0.017−0.017
0.00114	11	0.77	0.392±0.014+0.018−0.015
0.00114	11	0.83	0.378±0.013+0.014−0.011
0.00114	11	0.89	0.392±0.015+0.016−0.008
0.00225	11	0.59	0.359±0.028+0.015−0.011
0.00225	11	0.65	0.396±0.023+0.012−0.019
0.00225	11	0.71	0.418±0.021+0.016−0.017
0.00225	11	0.77	0.384±0.016+0.016−0.015
0.00225	11	0.83	0.370±0.014+0.012−0.012
0.00225	11	0.89	0.398±0.016+0.011−0.008
0.00445	11	0.59	0.384±0.043+0.095−0.014
0.00445	11	0.65	0.350±0.033+0.011−0.062
0.00445	11	0.71	0.358±0.028+0.013−0.058
0.00445	11	0.77	0.370±0.023+0.015−0.048
0.00445	11	0.83	0.356±0.020+0.011−0.040
0.00445	11	0.89	0.368±0.023+0.008−0.092
0.00872	11	0.575	0.284±0.148+0.378−0.028
0.00872	11	0.725	0.099±0.051+0.023−0.010
0.00872	11	0.875	0.169±0.059+0.006−0.024

Table A.13: *Ratio $r^{LP(3)}$ in bins of x, Q^2 and x_L with the statistical, upper-systematic and lower-systematic uncertainties.*

x	Q^2 $(\mathbf{GeV}^2)$	x_L	$r^{LP(3)}$
0.00029	22	0.575	0.430±0.096+0.060−0.033
0.00029	22	0.725	0.365±0.054+0.017−0.022
0.00029	22	0.875	0.365±0.048+0.016−0.011
0.00058	22	0.59	0.369±0.036+0.017−0.022
0.00058	22	0.65	0.378±0.029+0.018−0.012
0.00058	22	0.71	0.417±0.026+0.027−0.020
0.00058	22	0.77	0.371±0.020+0.032−0.015
0.00058	22	0.83	0.357±0.017+0.026−0.015
0.00058	22	0.89	0.368±0.020+0.025−0.009
0.00114	22	0.59	0.329±0.030+0.017−0.016
0.00114	22	0.65	0.380±0.026+0.014−0.011
0.00114	22	0.71	0.407±0.023+0.018−0.015
0.00114	22	0.77	0.371±0.018+0.018−0.014
0.00114	22	0.83	0.370±0.016+0.014−0.013
0.00114	22	0.89	0.368±0.018+0.016−0.008
0.00225	22	0.59	0.423±0.037+0.016−0.018
0.00225	22	0.65	0.322±0.026+0.013−0.009
0.00225	22	0.71	0.395±0.024+0.017−0.017
0.00225	22	0.77	0.448±0.021+0.025−0.017
0.00225	22	0.83	0.371±0.017+0.015−0.011
0.00225	22	0.89	0.375±0.019+0.017−0.008
0.00445	22	0.59	0.313±0.033+0.025−0.010
0.00445	22	0.65	0.404±0.031+0.018−0.014
0.00445	22	0.71	0.444±0.027+0.018−0.017
0.00445	22	0.77	0.443±0.022+0.030−0.018
0.00445	22	0.83	0.349±0.017+0.014−0.011
0.00445	22	0.89	0.380±0.020+0.024−0.008
0.00872	22	0.575	0.482±0.049+0.060−0.027
0.00872	22	0.725	0.435±0.028+0.018−0.015
0.00872	22	0.875	0.386±0.023+0.015−0.048

Table A.14: *Ratio $r^{LP(3)}$ in bins of x, Q^2 and x_L with the statistical, upper-systematic and lower-systematic uncertainties.*

x	Q^2 **(GeV^2)**	x_L	$r^{LP(3)}$
0.00058	44	0.575	0.238±0.083+0.041−0.022
0.00058	44	0.725	0.273±0.054+0.067−0.087
0.00058	44	0.875	0.199±0.039+0.026−0.032
0.00114	44	0.59	0.382±0.051+0.026−0.016
0.00114	44	0.65	0.409±0.042+0.031−0.019
0.00114	44	0.71	0.390±0.035+0.026−0.018
0.00114	44	0.77	0.470±0.031+0.031−0.022
0.00114	44	0.83	0.342±0.024+0.020−0.012
0.00114	44	0.89	0.431±0.030+0.027−0.011
0.00225	44	0.59	0.382±0.047+0.022−0.019
0.00225	44	0.65	0.373±0.037+0.017−0.013
0.00225	44	0.71	0.471±0.036+0.020−0.019
0.00225	44	0.77	0.392±0.026+0.018−0.015
0.00225	44	0.83	0.361±0.022+0.015−0.012
0.00225	44	0.89	0.376±0.026+0.017−0.01
0.00445	44	0.59	0.373±0.050+0.021−0.015
0.00445	44	0.65	0.433±0.044+0.017−0.018
0.00445	44	0.71	0.423±0.037+0.018−0.015
0.00445	44	0.77	0.445±0.031+0.020−0.018
0.00445	44	0.83	0.390±0.025+0.017−0.015
0.00445	44	0.89	0.427±0.030+0.016−0.009
0.00872	44	0.59	0.424±0.059+0.020−0.014
0.00872	44	0.65	0.380±0.044+0.019−0.030
0.00872	44	0.71	0.481±0.043+0.026−0.026
0.00872	44	0.77	0.432±0.033+0.021−0.028
0.00872	44	0.83	0.433±0.029+0.014−0.014
0.00872	44	0.89	0.428±0.033+0.017−0.014
0.0172	44	0.59	0.379±0.092+0.095−0.012
0.0172	44	0.65	0.441±0.080+0.020−0.060
0.0172	44	0.71	0.388±0.063+0.029−0.015
0.0172	44	0.77	0.339±0.048+0.021−0.116
0.0172	44	0.83	0.318±0.041+0.011−0.034
0.0172	44	0.89	0.399±0.052+0.131−0.008

Table A.15: *Ratio $r^{LP(3)}$ in bins of x, Q^2 and x_L with the statistical, upper-systematic and lower-systematic uncertainties.*

x	Q^2 $(\mathbf{GeV}^2)$	x_L	$r^{LP(3)}$
0.00114	88	0.575	0.172±0.103+0.132−0.005
0.00114	88	0.725	0.283±0.080+0.032−0.030
0.00114	88	0.875	0.229±0.063+0.042−0.019
0.00225	88	0.59	0.374±0.071+0.023−0.015
0.00225	88	0.65	0.385±0.058+0.027−0.020
0.00225	88	0.71	0.385±0.049+0.023−0.016
0.00225	88	0.77	0.419±0.042+0.027−0.019
0.00225	88	0.83	0.353±0.034+0.014−0.013
0.00225	88	0.89	0.418±0.042+0.016−0.011
0.00445	88	0.59	0.392±0.070+0.015−0.017
0.00445	88	0.65	0.362±0.054+0.019−0.016
0.00445	88	0.71	0.339±0.044+0.023−0.012
0.00445	88	0.77	0.408±0.040+0.021−0.018
0.00445	88	0.83	0.418±0.036+0.017−0.014
0.00445	88	0.89	0.403±0.040+0.016−0.017
0.00872	88	0.59	0.375±0.071+0.015−0.028
0.00872	88	0.65	0.389±0.057+0.011−0.026
0.00872	88	0.71	0.426±0.051+0.016−0.016
0.00872	88	0.77	0.381±0.039+0.022−0.014
0.00872	88	0.83	0.316±0.032+0.012−0.010
0.00872	88	0.89	0.425±0.042+0.022−0.017
0.0172	88	0.59	0.459±0.088+0.017−0.049
0.0172	88	0.65	0.372±0.063+0.028−0.017
0.0172	88	0.71	0.393±0.055+0.016−0.055
0.0172	88	0.77	0.439±0.048+0.021−0.019
0.0172	88	0.83	0.464±0.044+0.015−0.019
0.0172	88	0.89	0.404±0.046+0.025−0.013
0.0345	88	0.575	0.373±0.097+0.023−0.213
0.0345	88	0.725	0.377±0.060+0.019−0.020
0.0345	88	0.875	0.304±0.047+0.011−0.013

Table A.16: *Ratio $r^{LP(3)}$ in bins of x, Q^2 and x_L with the statistical, upper-systematic and lower-systematic uncertainties.*

x	Q^2 **(GeV^2)**	x_L	$r^{LP(3)}$
0.00225	174	0.575	0.654±0.312+0.024−0.054
0.00225	174	0.725	0.182±0.095+0.008−0.090
0.00225	174	0.875	0.276±0.105+0.031−0.021
0.00445	174	0.575	0.439±0.080+0.032−0.015
0.00445	174	0.725	0.389±0.046+0.019−0.018
0.00445	174	0.875	0.373±0.040+0.016−0.010
0.00872	174	0.575	0.402±0.076+0.027−0.017
0.00872	174	0.725	0.413±0.047+0.023−0.018
0.00872	174	0.875	0.391±0.040+0.024−0.009
0.0172	174	0.575	0.338±0.066+0.015−0.020
0.0172	174	0.725	0.388±0.044+0.017−0.015
0.0172	174	0.875	0.351±0.036+0.019−0.016
0.0345	174	0.575	0.397±0.083+0.034−0.019
0.0345	174	0.725	0.327±0.045+0.032−0.012
0.0345	174	0.875	0.361±0.043+0.026−0.008
0.0829	174	0.575	0.335±0.143+0.012−0.069
0.0829	174	0.725	0.551±0.116+0.021−0.133
0.0829	174	0.875	0.299±0.072+0.010−0.025
0.00872	377	0.575	0.403±0.122+0.032−0.011
0.00872	377	0.725	0.270±0.060+0.016−0.024
0.00872	377	0.875	0.366±0.063+0.018−0.011
0.0172	377	0.575	0.504±0.168+0.096−0.053
0.0172	377	0.725	0.510±0.105+0.022−0.037
0.0172	377	0.875	0.732±0.118+0.031−0.067
0.0345	377	0.575	0.315±0.104+0.015−0.021
0.0345	377	0.725	0.419±0.074+0.024−0.035
0.0345	377	0.875	0.259±0.050+0.020−0.017
0.0829	377	0.575	0.257±0.077+0.024−0.021
0.0829	377	0.725	0.285±0.049+0.021−0.016
0.0829	377	0.875	0.125±0.027+0.017−0.003

Table A.17: *Ratio $r^{LP(3)}$ in bins of x, Q^2 and x_L with the statistical, upper-systematic and lower-systematic uncertainties.*

x	Q^2 **(GeV^2)**	$r^{LP(2)}$
8.5E-05	3.4	$0.185 \pm 0.007^{+0.009}_{-0.004}$
0.00015	3.4	$0.166 \pm 0.004^{+0.008}_{-0.004}$
0.00029	3.4	$0.149 \pm 0.003^{+0.005}_{-0.004}$
0.00058	3.4	$0.141 \pm 0.003^{+0.004}_{-0.003}$
0.00114	3.4	$0.156 \pm 0.005^{+0.004}_{-0.006}$
0.00225	3.4	$0.153 \pm 0.025^{+0.02}_{-0.009}$
8.5E-05	5.9	$0.16 \pm 0.012^{+0.01}_{-0.006}$
0.00015	5.9	$0.175 \pm 0.003^{+0.006}_{-0.004}$
0.00029	5.9	$0.172 \pm 0.002^{+0.007}_{-0.004}$
0.00058	5.9	$0.181 \pm 0.003^{+0.006}_{-0.004}$
0.00114	5.9	$0.168 \pm 0.003^{+0.005}_{-0.005}$
0.00225	5.9	$0.18 \pm 0.005^{+0.006}_{-0.004}$
0.00445	5.9	$0.214 \pm 0.039^{+0.01}_{-0.079}$
0.00015	11	$0.182 \pm 0.014^{+0.013}_{-0.01}$
0.00029	11	$0.173 \pm 0.003^{+0.008}_{-0.004}$
0.00058	11	$0.159 \pm 0.002^{+0.005}_{-0.003}$
0.00114	11	$0.171 \pm 0.003^{+0.005}_{-0.004}$
0.00225	11	$0.17 \pm 0.003^{+0.004}_{-0.004}$
0.00445	11	$0.155 \pm 0.005^{+0.004}_{-0.02}$
0.00872	11	$0.058 \pm 0.016^{+0.003}_{-0.006}$
0.00029	22	$0.171 \pm 0.016^{+0.006}_{-0.006}$
0.00058	22	$0.167 \pm 0.004^{+0.009}_{-0.004}$
0.00114	22	$0.163 \pm 0.004^{+0.005}_{-0.003}$
0.00225	22	$0.17 \pm 0.004^{+0.006}_{-0.004}$
0.00445	22	$0.171 \pm 0.004^{+0.006}_{-0.004}$
0.00872	22	$0.171 \pm 0.008^{+0.005}_{-0.01}$

Table A.18: *Ratio $r^{LP(2)}$ in bins of x and Q^2 with the statistical and systematic uncertainties.*

x	Q^2 **(GeV^2)**	$r^{LP(2)}$
0.00058	44	$0.11 \pm 0.015^{+0.017}_{-0.017}$
0.00114	44	$0.182 \pm 0.006^{+0.009}_{-0.005}$
0.00225	44	$0.166 \pm 0.005^{+0.005}_{-0.003}$
0.00445	44	$0.178 \pm 0.006^{+0.006}_{-0.004}$
0.00872	44	$0.187 \pm 0.007^{+0.006}_{-0.005}$
0.0172	44	$0.151 \pm 0.01^{+0.006}_{-0.01}$
0.00114	88	$0.118 \pm 0.023^{+0.015}_{-0.007}$
0.00225	88	$0.171 \pm 0.009^{+0.007}_{-0.004}$
0.00445	88	$0.17 \pm 0.008^{+0.006}_{-0.004}$
0.00872	88	$0.163 \pm 0.008^{+0.005}_{-0.003}$
0.0172	88	$0.179 \pm 0.01^{+0.006}_{-0.005}$
0.0345	88	$0.136 \pm 0.016^{+0.004}_{-0.005}$
0.00225	174	$0.123 \pm 0.035^{+0.008}_{-0.014}$
0.00445	174	$0.166 \pm 0.013^{+0.006}_{-0.004}$
0.00872	174	$0.174 \pm 0.013^{+0.008}_{-0.004}$
0.0172	174	$0.158 \pm 0.012^{+0.006}_{-0.005}$
0.0345	174	$0.149 \pm 0.013^{+0.007}_{-0.003}$
0.0829	174	$0.156 \pm 0.027^{+0.005}_{-0.023}$
0.00872	377	$0.141 \pm 0.019^{+0.005}_{-0.004}$
0.0172	377	$0.266 \pm 0.036^{+0.01}_{-0.016}$
0.0345	377	$0.141 \pm 0.019^{+0.007}_{-0.008}$
0.0829	377	$0.079 \pm 0.011^{+0.004}_{-0.001}$

Table A.19: *Ratio $r^{LP(2)}$ in bins of x and Q^2 with the statistical and systematic uncertainties.*

Q^2 **(GeV^2)**	$\langle r^{LP(2)} \rangle$
3.4	0.142±0.009
5.9	0.162±0.006
11	0.168±0.004
22	0.174±0.003
44	0.168±0.002
88	0.167±0.002
174	0.175±0.002
377	0.156±0.002

Table A.20: *Averaged ratio $\langle r^{LP(2)} \rangle$ in bins of Q^2 with the statistical uncertainties.*

x	Q^2 **(GeV^2)**	$\bar{F}_2^{LP(2)}$
8.5E-05	3.4	$0.2265 \pm 0.0092^{+0.0115}_{-0.0056}$
0.00015	3.4	$0.1826 \pm 0.0048^{+0.009}_{-0.0048}$
0.00029	3.4	$0.1412 \pm 0.0037^{+0.0049}_{-0.0046}$
0.00058	3.4	$0.1148 \pm 0.0032^{+0.0038}_{-0.0025}$
0.00114	3.4	$0.11 \pm 0.0038^{+0.0033}_{-0.0046}$
0.00225	3.4	$0.0936 \pm 0.0155^{+0.0128}_{-0.0059}$
8.5E-05	5.9	$0.2381 \pm 0.0181^{+0.0154}_{-0.0095}$
0.00015	5.9	$0.2339 \pm 0.0042^{+0.0081}_{-0.0057}$
0.00029	5.9	$0.1954 \pm 0.0031^{+0.0082}_{-0.0047}$
0.00058	5.9	$0.1757 \pm 0.0032^{+0.0064}_{-0.0044}$
0.00114	5.9	$0.1392 \pm 0.0029^{+0.0043}_{-0.0042}$
0.00225	5.9	$0.128 \pm 0.004^{+0.0042}_{-0.0035}$
0.00445	5.9	$0.1308 \pm 0.024^{+0.0062}_{-0}$
0.00015	11	$0.3021 \pm 0.0244^{+0.023}_{-0.0182}$
0.00029	11	$0.242 \pm 0.0048^{+0.012}_{-0.0066}$
0.00058	11	$0.1878 \pm 0.0032^{+0.0066}_{-0.0044}$
0.00114	11	$0.1704 \pm 0.0032^{+0.0058}_{-0.0041}$
0.00225	11	$0.1425 \pm 0.003^{+0.0041}_{-0.0035}$
0.00445	11	$0.11 \pm 0.0036^{+0.0031}_{-0.0141}$
0.00872	11	$0.0352 \pm 0.0101^{+0.0021}_{-0.004}$
0.00029	22	$0.2998 \pm 0.0297^{+0.0115}_{-0.011}$
0.00058	22	$0.2437 \pm 0.0066^{+0.0137}_{-0.0067}$
0.00114	22	$0.1967 \pm 0.0048^{+0.0069}_{-0.0047}$
0.00225	22	$0.1699 \pm 0.0044^{+0.0065}_{-0.0039}$
0.00445	22	$0.1407 \pm 0.0038^{+0.0057}_{-0.0035}$
0.00872	22	$0.1172 \pm 0.0055^{+0.0038}_{-0.0074}$

Table A.21: *Leading-proton-tagged structure function $\bar{F}_2^{LP(2)}$ in bins of x and Q^2 with the statistical and systematic uncertainties.*

x	Q^2 $(\mathbf{GeV}^2)$	$\bar{F}_2^{LP(2)}$
0.00058	44	$0.1941 \pm 0.0264^{+0.0298}_{-0.0302}$
0.00114	44	$0.2613 \pm 0.0096^{+0.0141}_{-0.0078}$
0.00225	44	$0.194 \pm 0.0068^{+0.0068}_{-0.0046}$
0.00445	44	$0.1681 \pm 0.0062^{+0.006}_{-0.0043}$
0.00872	44	$0.1433 \pm 0.0057^{+0.0047}_{-0.0043}$
0.0172	44	$0.0949 \pm 0.0068^{+0.0039}_{-0.0064}$
0.00114	88	$0.1986 \pm 0.0385^{+0.0252}_{-0.0127}$
0.00225	88	$0.2285 \pm 0.0122^{+0.0094}_{-0.006}$
0.00445	88	$0.1814 \pm 0.0093^{+0.0064}_{-0.0051}$
0.00872	88	$0.1374 \pm 0.0074^{+0.005}_{-0.0033}$
0.0172	88	$0.1216 \pm 0.0071^{+0.0041}_{-0.0037}$
0.0345	88	$0.0747 \pm 0.0087^{+0.0027}_{-0.0028}$
0.00225	174	$0.1861 \pm 0.0535^{+0.0125}_{-0.0221}$
0.00445	174	$0.1967 \pm 0.0162^{+0.0073}_{-0.0054}$
0.00872	174	$0.1606 \pm 0.0128^{+0.0081}_{-0.0045}$
0.0172	174	$0.1142 \pm 0.0091^{+0.0045}_{-0.0036}$
0.0345	174	$0.0853 \pm 0.0079^{+0.0044}_{-0.002}$
0.0829	174	$0.0681 \pm 0.0118^{+0.0023}_{-0.0102}$
0.00872	377	$0.1409 \pm 0.0195^{+0.0053}_{-0.0045}$
0.0172	377	$0.2053 \pm 0.0282^{+0.0077}_{-0.0124}$
0.0345	377	$0.084 \pm 0.0112^{+0.0041}_{-0.0047}$
0.0829	377	$0.0351 \pm 0.0048^{+0.002}_{-0.0008}$

Table A.22: *Leading-proton-tagged structure function* $\bar{F}_2^{LP(2)}$ *in bins of* x *and* Q^2 *with the statistical and systematic uncertainties.*

Bibliography

[1] ZEUS Collab., M. Derrick et al., Z. Phys. **C 3**, 253 (1997).

[2] M. Basile et al., Lett. Nuovo Cim. **41**, 298 (1984).

[3] V.N. Gribov et al. (ed.), World Scientific Series in 20th Century Physics **25** (2001).

[4] M. Aguilar-Benitez et al., Z. Phys. **C 50**, 405 (1991).

[5] A.E. Brenner et al., Phys. Rew. **D 26**, 1497 (1982).

[6] H1 Collab., C. Adloff et al, Nucl. Phys. **B 619**, 3 (2001).

[7] H1 Collab., C. Adloff et al, Eur. Phys. J. **C 6**, 587 (1999).

[8] ZEUS Collab., S. Chekanov et al., Nucl. Phys. **B 685**, 3 (2002).

[9] M. Basile et al., Nuovo Cimento **A 79**, 1 (1984).

[10] A. Zichichi, *Deep Inelastic Scattering DIS01.* (2001).

[11] E. D. Bloom et al, Phys. Rew. Lett. **8**, 214 (1964).

[12] J.D. Bjorken, Phys. Rew. **179**, 1547 (1969).

[13] M. Gell-Mann, Phys. Lett. **8**, 1365 (1964).

[14] G. Zweig, CERN-8192/TH **401** (1964);
G. Zweig, CERN-8419/TH **402** (1964).

[15] R.P. Feynmann, Phys. Rew. Lett **23**, 1415 (1969).

[16] G. Altarelli and G. Parisi, Nucl. Phys. **B 126**, 298 (1977);
V.N. Gribov and L.N Lipatov, Sov. J. Nucl. Phys. **15**, 438 (1972);
Yu. L. Dokshitzer, Sov. Phys. JETP **45**, 641 (1977).

[17] ZEUS Collab., M. Derrick et al., Phys. Lett. **B 303**, 182 (1993);
ZEUS Collab., M. Derrick et al., Z. Phys. **C 72**, 399 (1996).

[18] ZEUS Collab., Eur. Phys. J. **C 42**, 13 (2005).

[19] H1 Collab., T. Ahmed et al, Nucl. Phys. **B 470**, 3 (1996).

[20] L.D. Landau and I. Ya. Pomeranchuk, Zh. Eksp. Teor. Fiz. **24**, 505 (1953).

[21] ZEUS Collab. M. Derrick et al., Phys Lett. **B 315**, 481 (1993).

[22] H1 Collab., T. Ahmed et al., Nucl Phys. **B 429**, 477 (1994).

[23] ZEUS Collab., M. Derrick et al., Eur. Phys. J. **C 6**, 43 (1999).

[24] G. Ingelman and P.E. Schlein, Phys. Lett. **B 152**, 256 (1985).

[25] ZEUS Collab., S. Chekanov et al., Nucl. Phys. **B 637**, 3 (2002).

[26] T. Regge, Nuovo Cimento Ser. **14**, 10 (1959).

[27] A. Szczurek, N.N. Nikolaev and J. Speth, Phys. Lett. **B 428**, 383 (1998).

[28] G.F. Chew and S.C. Frautschi, Phys. Rev. Lett. **8**, 41 (1962).

[29] A. Donnachie, P.V. Landshoff, Nucl. Phys. **B 244**, 322 (1984);
A. Donnachie, P.V. Landshoff, Nucl. Phys. Lett **B 191**, 309 (1987);
A. Donnachie, P.V. Landshoff, Nucl. Phys. **B 303**, 634 (1988);
A. Donnachie, P.V. Landshoff, Nucl. Phys. Lett **B 296**, 227 (1992).

[30] ZEUS Collab., S. Chekanov et al., Eur. Phys. J. **C 26**, 389 (2003).

[31] H. Yukawa, Proc. Phys. Math. Soc. Jap. **17**, 48 (1935);
M. Bishari, Phys. Lett. **B 38**, 510 (1972);
B.G. Zakharov and V.N. Sergeev, Sov. J. Nucl. Phys. **38**, 947 (1983).

[32] L. Trentadue and G. Veneziano, Phys. Lett. **B 323**, 201 (1994);
D. de Florian and R. Sassot, Phys. Rew. **D 56**, 426 (1997).

[33] B. Andersson et al., Phys. Rep. **97**, 31 (1983).

[34] ZEUS coll, U. Holm (ed.), *The ZEUS Detector*. Status Report (unpublished), DESY (1993), available on `http://www-zeus.desy.de/bluebook/bluebook.html`.

[35] S.M. Fisher P. Palazzi, *Adamo 3.2* (1992).

[36] E. Barberis et al., Nucl. Instr. and Meth. **A 364**, 507 (1995).

[37] D.E. Dorfan, Nucl. Instr. and Meth. **A 342**, 143 (1994);
E. Barberis et al., Nucl. Phys. **B 32**, 513 (1993).

[38] J. DeWitt, Nucl. Instr. and Meth. **A 288**, 209 (1990);
J. DeWitt, *The Time Slice Chip*. Senior Thesis, UC Santa Cruz, 1989.

[39] A. Staiano, Nucl. Phys. **B 54**, 125 (1997).

[40] R. Battiston et al., Nucl. Instr. and Meth. **A 238**, 35 (1985).

[41] S. Bhadra et al., Nucl. Instr. and Meth. **A 394**, 121 (1997).

[42] R. Sacchi, *Studio di eventi diffrattivi con uno spettrometro per protoni a ZEUS*. Tesi di Dottorato, University of Torino, 1996.

[43] J. Rahn, *Studying Characteristics of Diffractive Deep Inelastic Scattering with the ZEUS Leading Proton Spectrometer*. PhD Thesis, UC Santa Cruz, 1997.

[44] ZEUS Collaboration, M. Derrick et al., Z. Phys. **C 73**, 253 (1997).

[45] H. Plothow-Besch, Comput. Phys. Commun. **75**, 396 (1993).

[46] A. Kwiatkowski, H.-J. Möhring and H. Spiesberger, Comput. Phys. Commun. **69**, 155 (1992).

[47] G. Ingelman, A. Edin and J. Rathsman, Comput. Phys. Commun. **101**, 108 (1997).

[48] K. Charchuła, G.A. Schuler, H. Spiesberger, Comput. Phys. Commun. **81**, 381 (1994).

[49] T. Sjöstrand, Comput. Phys. Commun. **82**, 74 (1994).

[50] L. Löhnblad, Comput. Phys. Commun. **71**, 15 (1992).

[51] R. Brun et al., CERN DD/EE/11-1 (1989).

[52] Els de Wolf et al. (ed.), *ZGANA, Zeus trigger simulation library.*

[53] S. Maselli, A. Solano, *The LPS simulation in Mozart, ZEUS 91-112* (1991).

[54] S. Maselli, R. Sacchi, *LPS acceptance calculation and update of the LPS simulation, ZEUS 92-43* (1992).

[55] CTEQ Collab., H.L. Lai et al, Eur. Phys. J. **C 12**, 375 (2000).

[56] T. Sjöstrand, Comput. Phys. Commun. **135**, 238 (2001).

[57] H. Abramowicz, A. Caldwell and R. Sinkus, NUcl. Inst. Meth. **A 365**, 508 (1995).

[58] G. Bruni, G. Iacobucci, L. Rinaldi and M. Ruspa, *Proceedings of the HERA-LHC workshop (CERN-2005-014)*, p. 605. (2005).

[59] ZEUS Collab., *Proceedings of the International Europhysics Conference on High Energy Physics*, p. Abstract:544. (2003).